UNIVERSITÀ DEGLI STUDI DI PADOVA
DIPARTIMENTO DI INGEGNERIA CIVILE, EDILE E AMBIENTALE
Department Of Civil, Environmental and Architectural Engineering

Corso di Laurea Magistrale in Mathematical Engineering

TESI DI LAUREA

A process based model for investigating the re-endothelialization of stented vessels

Relatore:
Chiar.mo PROF. STEFANO LANZONI
Correlatore:
PROF. PAOLO PERUZZO

Laureando: **Jacopo Del Ferraro**
Matricola 2027597

ANNO ACCADEMICO 2022-2023

Abstract

Understanding the consequences and complications that arise after the implantation of a stent in a blood vessel is a complex and multidisciplinary topic.

The objective of this thesis is to simulate processes such as re-endothelialization and in-stent restenosis using models based on fluid dynamics parameters. In the first chapter we introduce the fundamental clinical and medical aspects regarding stent implantation and its consequences.

Numerous studies have explored these phenomena through in-vivo simulations or clinical results to grasp the primary causes, while only a few have proposed virtual simulations to reproduce the occlusion process. In the second chapter, we discuss the results of these various approaches, along with their respective advantages, drawbacks, and limitations.

In the third chapter we focus on the methods used and the modeling choices taken during the simulations. Our study focuses on singular stent type, under ideal flow conditions. The basic idea is to simulate endothelial growth varying locally the dynamical viscosity profile. Firstly, we assess the progression in steady-state flow for a single stented artery. Then we proceed with unsteady flows, considering two different vessel geometries and rheological models.

In the fourth and fifth chapter we will present the results of the stationary and time dependent simulations, respectively. We focus on the changes of the main blood flow parameters and the corresponding computed neointimal growth.

At last, we will compare the results of our different simulations, considering the various regimes and geometries, and assess them with both $in - vivo$ data and multiscale numerical simulations results found in the literature.

Contents

Chapter 1

Introduction

1.1 Preface

To achieve a comprehensive understanding of biological systems a multidisciplinary approach is needed, their inherent complexity has always fascinated and challenged physician and scientists alike.
We were always interested in human physiology and we started to analyze it since ancient time, even though the first detailed studies of the cardiovascular system are dated at the beginning of the XVIII century. Interdisciplinary collaborations between healthcare and engineering are not new, nevertheless, since the introduction of the X-ray in 1895, a technical revolution swept over the medical world with the development of instrumentation, devices, products, procedures, as well as diagnostic and operational systems.

$In - vivo$, clinical studies, and in vitro simulations are still crucial tools used nowadays to study blood flow and hemodynamics, but the introduction of computation fluid dynamic (CFD) has sped up the process considerably; the experimental results are the benchmark for complicated and detailed simulations.
The collaboration between medicine and engineering, in particular for modelling the cardiovascular system, has already brought remarkable results. Models have been used to support medical decisions, to evaluate patient-specific cases and eventual post-operational risks; nonetheless the huge inter- and intra-patient data variability and uncertainty are sources of concern for the models calibration and validation (Quarteroni 2017). Computational Fluid Dynamics is a key instrument used to analyze the local flow fields due to changes in coronary artery geometry. CFD plays a significant role in identifying risk factors and understanding the pathophysiology of coronary artery disease. In particular, CFD simulations allow researchers to study blood flow under various conditions, helping to gain insights into disease mechanisms, such as biomechanics of atherosclerotic plaques, plaques location and

progression. This complex scientific framework explains the increased interest from both the mathematical and bioengineering communities over the past 25 years.

1.2 Clinical Aspects

1.2.1 Atherosclerosis

The arterial tree is a complex structure, in charge of transporting blood and nutrients across the whole body. The cardiovascular system is a intricate branching network susceptible to a multitude of variables and irregularities.

Atherosclerosis remains a leading cause of death in the developed world, it consists of a process whereby deposits of fatty and inflammatory material build up inside arterial walls (Fig 1.1), create plaques, and obstruct normal blood flow (Mahmoudi 2021). Atherosclerotic plaques are commonly developed in the coronary arteries, causing a narrowing that reduces the blood flow to the heart muscle and in many cases leads to ischemia and myocardial infarction.

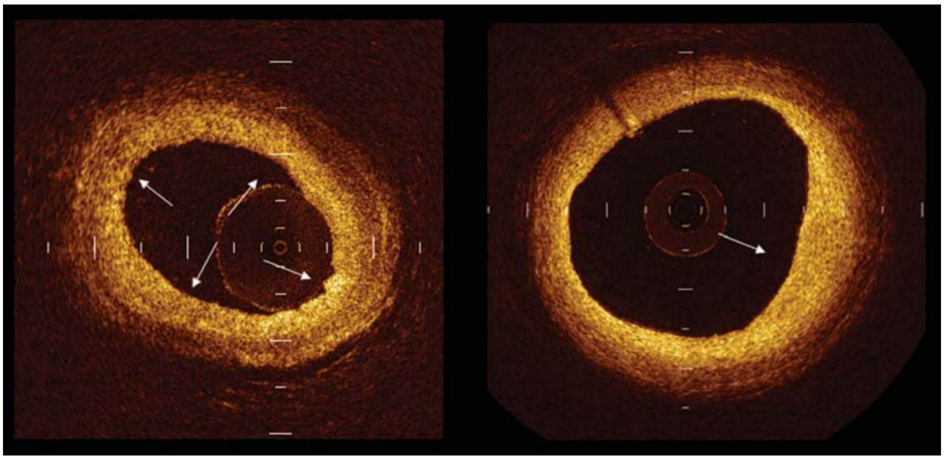

Figure 1.1: Example of intimal thickening revealed by optical coherence tomography as a bright homogeneous layer. The left panel shows a diffuse intimal thickening, the right panel a localized one (arrow) (Prati 2010)

Atherosclerosis is associated with genetic predisposition and multiple risk factors such as hypertension, smoking, hyperlipidemia, diabetes mellitus, social stress, sedentary lifestyle, and viral infections.
It is a disease that primarily manifests at the outer edges of blood vessels bifurcations, branch points, and curved arterial segments (Malek 1999, Van der Heiden 2013). In these vulnerable regions the blood flow is noticeably slowed and it is highly influenced by the cardiac cycle, resulting in a weak hemodynamic shear stress; conversely steady blood flow and higher magnitude shear stresses characterize healthy vessel regions.

1.2.2 Stent Implantation

The field of percutaneous coronary intervention has evolved rapidly in the last fourty years. In 1977 Andreas Grüntzig performed the first balloon angioplasty in the Universitätsspital in Zürich, Switzerland, and it is considered as one of the landmarks of cardiovascular medicine (Byrne 2015).
However balloon angioplasty was limited by the risk of abrupt closure (1%) and the lack of durability because of the early vessel recoil (5–10%) and restenosis (30-50%) (Schmidt and Abbott 2018). This procedure consists in the expansion of a stenosed artery from the lumen by applying pressure to a balloon located at a catheter tip; it is still the most frequent used treatment in vascular emergencies of the heart and the peripheral circulation (Barton 2014).

To reduce the risks and complication of the procedure, the implantation of a metallic stent in the treated vessel region was introduced; the first human coronary stent implantations were performed in Toulouse and Lausanne in 1986 (Byrne 2015). The additional mechanical strength brought by the stent structure attenuates the effects of vessel recoil and guarantees greater short-term luminal calibre, resulting in a lower rate of subsequent restenosis.
Stent implantation slowly became the standard treatment strategy and, therefore, the importance attributed to the stent design grew.
Stents are classified according to the mechanism of expansion, the construction technique and the coatings (Schmidt and Abbott 2018):

Mechanism of expansion. Stents can be balloon-expandable or self expanding.
The first are mounted on a balloon while contracted and delivered through a catheter; the latter ones are constructed to a certain size, collapsed in a stent delivery system to finally re-assume their original size once placed.

Construction. We refer to stent materials, construction methods and scaffolding.
The stent must be corrosion resistant and biocompatible to prevent an immune response with consequential inflammation and restenosis. Moreover the stent composition impacts greatly on characteristics like elastic modulus, yields strength and tensile strength with consequences on stiffness of the material, resistance to plastic deformation and to longitudinal forces. Originally the metallic backbone of the stent was made of a stainless steel alloys of iron, nickel, chromium, and molybdenum; nowadays a cobalt-chromium composition is used. The evolution of the materials has allowed thinner struts with subsequent increase of the inner diameter and flexibility while decreasing the chances of vascular injury.
Additionally we can classify stent as coil, slotted or modular by construction method and scaffolding structure.The commercially available stent today are all made of

modular open cell stents (Fig 1.2), constructed by fusing together repeated modules with cells not connected on all of the sides

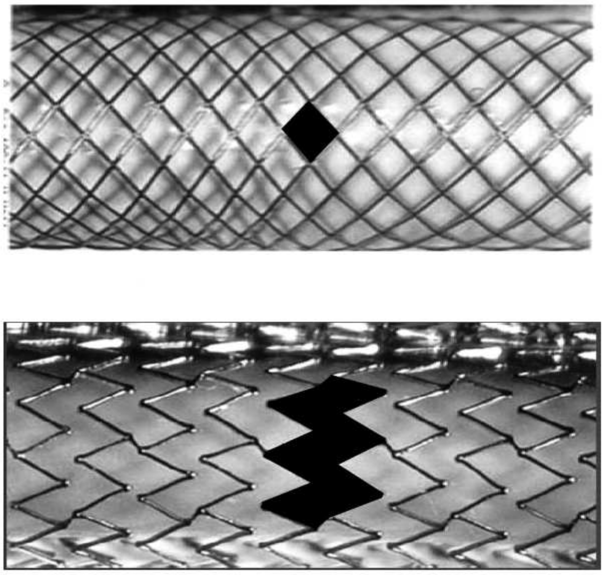

Figure 1.2: . Examples of a closed-cell design stent and an open-cell modular design stent, the free cell area is marked in black for both stent types. (Schillinger 2008)

Coatings. Usually, stents are divided by bare metal and drug eluting stents.
In response to the vascular injury due to stent implantation a proliferation and migration of smooth muscle cells to the stented region wall occurs, with consequent lumen loss. This phenomenon is called neointimal hyperplasia and reducing its effect is the main objective of the coating procedure. Drug eluting stents are covered with a bio-compatible polymer, which act as a carrier for anti-proliferative drugs; the objective is to obtain a slow controlled elution to ensure the release of this cell growth inhibitor over a long period of time.

1.2.3 Consequences of stenting

Following a stent implantation, the stented segment of the artery can be re-narrowed by four key processes: thrombus formation, arterial inflammation, neointimal hyperplasia and remodelling (Murphy 2010). Damages during balloon angioplasty and stent implantation to the vessel wall are inevitable. These lesions induce an healing response mainly guided by the inflammation of tissues with consequent endothelial and smooth muscle cells migration (Zun 2019). After the intervention mainly two widespread adverse effects could affect the stented region: stent thrombosis and stent restenosis.

Stent Thrombosis

Stent thrombosis takes place when too many thrombocytes aggregate on the exposed stent struts and block the artery (Zun 2019). The injured parts of the vessel walls attract blood-borne platelets to the source of the injury where they adhere to the damaged cells and release chemical attractants for other platelets; finally, a stringy protein called fibrin forms around the platelets to bind them together into a thrombus (Murphy 2010).

This major acute complication is commonly classified into two categories: early stent thrombosis is defined as thrombosis within thirty days from the operation and it can manifest even hours after stenting; and late thrombosis if it occurs later than thirty days (Byrne 2015). The first type of thrombosis is caused mainly by stent undersizing, impaired blood flow and residual disease proximal to the stent lesion, in addition to patient specific risks; the latter one is linked to significant mechanical issues like stent undersizing, underexpansion (Fig 1.3) or stent malapposition. The evolution of drug eluting stents paired with contemporary anti-thrombotic therapies have halved the stent thrombosis overall rates in the last years, from 3% to 1.5% (Byrne 2015).

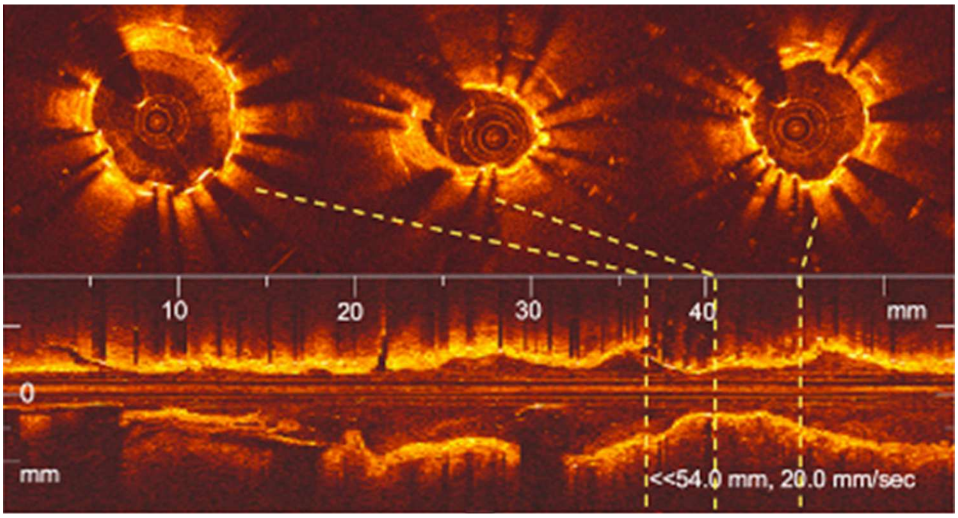

Figure 1.3: Optical coherence tomography (OCT) cross-sections of stent underexpansion, it can lead to both stent thrombosis and stent restenosis. (Erdogan 2022)

Stent Restenosis

Restenosis is a maladaptive healing response of the vessel wall. Angiographically, restenosis is classified as the presence of $> 50\%$ narrowing in the stented segment (Mitra and Agrawal 2006).

Balloon angioplasty and stent deployment partially or completely denude the endothelial layer and may stretch or even rupture its support elastic membrane called internal elastic lamina (Tahir 2015). This arterial injury triggers a cascade of mechanism involving platelet aggregation, migration, and proliferation of smooth muscle cells and stimulates the production of extracellular matrix materials (Mitra and Agrawal 2006). The accumulation of new tissue within the vessel is called neointimal hyperplasia.

Endothelialization consists in the smooth muscle cells proliferation, which cover the stent struts. Once the stent is embodied within the vessel wall, the endothelium recovers its function, and suppresses smooth muscle cell growth (Zun 2019). However, the healing is not always perfect, especially as drug eluting stents interfere with the propagating process in the stented region. If the growth stops too early the risk of late stent thrombosis is greatly increased due to the exposed stent struts; in contrast, if the growth is too intensive (Fig 1.4), it causes re-narrowing of the lumen vessel, or restenosis (Zun 2019).

Re-Endothelialization

The arteries walls have three distinct layers. The innermost layer is called intima and it is composed of a single layer of endothelial cells and the internal elastic lamina. The middle layer is called media, and mainly contains smooth muscle cells surrounded by a thin external elastic lamina. The third layer is the adventitial layer, which is the outer layer of the artery wall and consists of collagen and elastic tissue (Tahir 2015). The native endothelial layer has several functions and properties: provides hemostatic balance, acts as a barrier between blood and tissue, is selectively permeable, suppresses inflammation, controls vascular tone, creates and maintains an anti-thrombotic and anti-proliferative environment throughout the blood vessel for laminar flow of plasma and cellular constituents of blood (Jana 2019).

The restoration of healthy vascular endothelium is an important factor to avoid the lethal consequences of in-stent thrombosis and to prevent restenosis (Van der Heiden 2013). However, the exact process of re-endothelialization and its speed, the effect of a stent in the migration, proliferation and adhesion of endothelial cells are still poorly understood despite their importance.

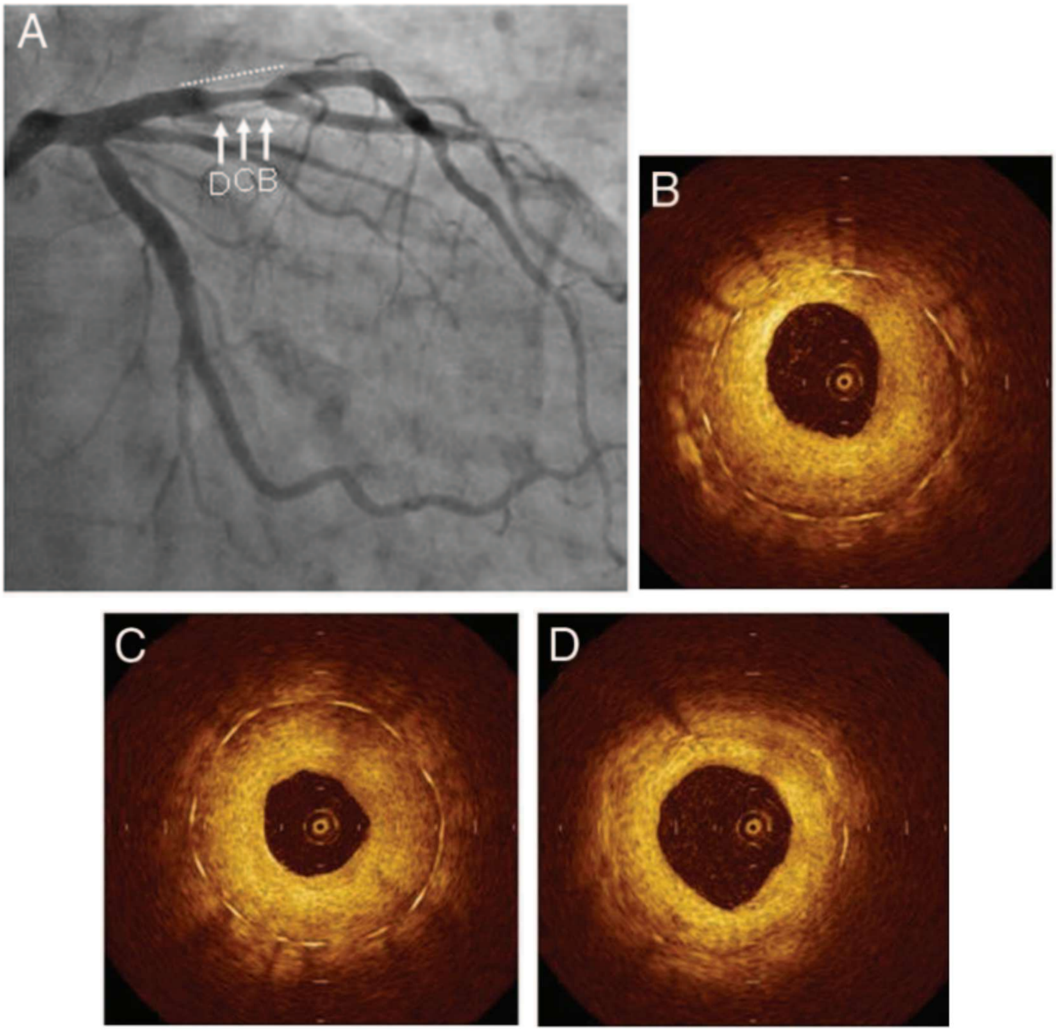

Figure 1.4: A case of early in-stent restenosis. (A)Follow-up coronary angiography 9 months post operation. The line indicates the implanted stent. (B through D) Typical OCT images of bare metal stent homogeneous restenotic tissue, in which the stent struts are visible (Habara 2011)

1.3 Biomechanical Forces

The characteristic pulsatile blood flow of the cardiovascular system exerts biomechanical forces through the whole arterial tree. These forces can act in circumferential, radial, and axial directions, deforming individual cells, atherosclerotic tissue, and the artery wall (Brown 2016). The non uniformity of atherosclerosis distribution, the uncertainty in the restenosis and re-endothelialization, and the intricate mechanical environment of stented arteries are strongly linked to the tangential forces acting on the vessel walls.

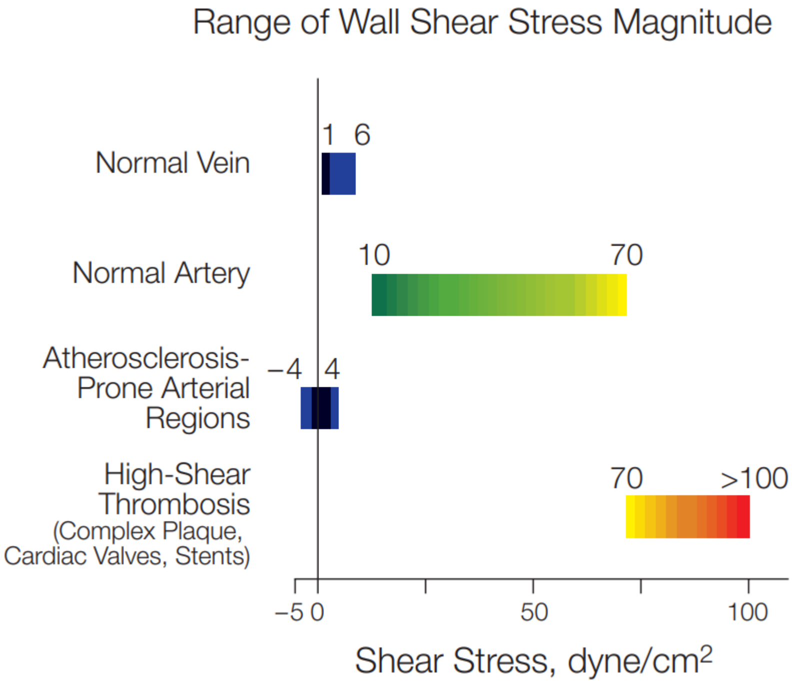

Figure 1.5: Tabular diagram illustrating the various range of wall shear stress magnitude (Malek 1999)

The wall shear stress (WSS) is the parallel frictional force exerted by blood flow on the endoluminal surface of the arterial wall (Brown 2016), with values highly influenced by arterial and luminal geometry, blood flow velocity and, in the case of a stented region, by the stent geometry.

Although the normal arterial shear stress typically falls in the range 1.0 –1.5 Pa, allometric arguments demonstrate that this range is not universal (Peiffer 2013).

The critical low threshold for neointimal formation is generally fixed around 0.4-0.5 Pa (4-5 dyne/cm^2) (Fig 1.5).

A disturbed blood flow can lead to change in both the magnitude and direction of wall shear stresses; regions exposed to low, time-averaged WSS, defined by the relation (1.1), or oscillatory stresses are prone to atherosclerosis and stent restenosis (Brown 2016).

$$TaWSS = \frac{1}{T}\int_0^T |WSS| dt \tag{1.1}$$

Although low wall shear stress is not sufficient to cause atherosclerosis and restenosis, it induces focal endothelial cell dysfunction and inflammation. To quantify the degree of flow reversal and the extent of possible recirculation zones two additional hemodynamic quantities are usually evaluated: the oscillatory shear index (OSI) and the relative residence time (RRT), defined respectively as

$$OSI = 0.5 \cdot \left[1 - \frac{|\int_0^T WSS\ dt|,}{\int_0^T |WSS| dt}\right] \tag{1.2}$$

and

$$RRT = \frac{1}{TaWSS \cdot (1 - 2 \cdot OSI)} = \frac{1}{\frac{1}{T} \cdot |\int_0^T WSS\ dt|.} \tag{1.3}$$

Moreover, it is worthwhile to note that WSS affects directly endothelial cells functionalities like mechanotransduction and biological transport processes (Mahmoudi 2021).

Percutaneous coronary interventions and stent placement greatly alter the mechanical environment of the vessel. Locally the stent struts produce perturbation in the flow patterns, whose size is correlated to that of the inter-strut recirculation zones and can affect thrombogenicity (Van der Heiden 2013).

Chapter 2

Modeling of a Stented Vessel: State of the Art

In this chapter, we will briefly discuss the effects of stent design on local blood flow dynamics. Next, we will provide a concise overview of clinically-based articles and numerical studies examining the relationship between neointimal growth and hemodynamic properties. Our emphasis will be on clinical data from human studies and $in-vivo$ animal testing, we briefly review the key computational fluid dynamics (CFD) simulations related to in-stent restenosis.

2.1 Flow Field in a Stented Vessel: Generalities

The arterial geometry is greatly altered by the rigid stent implantation, which modifies shear stresses, velocity profiles, and vessel wall properties (Koskinas 2012). Numerous factors influence the pro-restenotic processes associated with low wall shear stress regions, including specific stent design and configuration, strut dimensions and spacing, to name a few.

Wentzel et al. (2000) were among the first to study the changes in regional vessel geometry induced by a stent. Through 3D reconstruction of five pigs' stented left carotid arteries, they highlighted the formation of a great increase in curvature near the entrance and the exit of the stent and proposed an empirical correlation between the curvature gradient and the shear stress magnitude.

LaDisa et al. (2003) carried out a similar research, using the $in - vivo$ data of canine stented epicardial coronary arteries to build up CFD models. In particular, they studied the localized alterations of the wall shear rate within the region treated with a slotted-tube stent implantation (closed cell type shown in Fig. 1.2). The reported steady state results, obtained assuming a Newtonian fluid, highlight the

significance of stent design. The presence of the stent a) increases the cross-sectional area of the vessel correlated with low wall shear stress zones and b) determines low wall shear stress around stent struts, with the lowest values attained in the corners of each strut, probably due to a combination of stagnation flow and boundary layer separation.
In addition, angled struts act as converging and diverging nozzles to adjacent blood layers, while the wall shear stress decreases with each subsequent axial strut, suggesting a preference towards fewer axial struts in the stent design.
Finally, the low wall shear stress outlet region is a function of the inlet velocity, and it is characterized by lower shear stresses than that estimated at the inlet.

Duraiswamy et al. (2009) assessed the key hemodynamic parameters for four different commercially available stents, by modelling the blood flow as a Newtonian viscous incompressible fluid under pulsatile conditions. In particular, they focused on modeling a near-wall section of the vessel to enhance solution accuracy. The study involved two self-expandable stents and two slotted-tube balloon-expandable stents. The evaluated parameters included axial and transverse wall shear stresses, wall shear stress gradient, and a separation parameter. The results were consistent with in vivo animal data, and indicated that the alterations in blood flow cannot be solely attributed to strut thickness or spacing; rather, the overall strut and stent design also matters (Fig. 2.1).

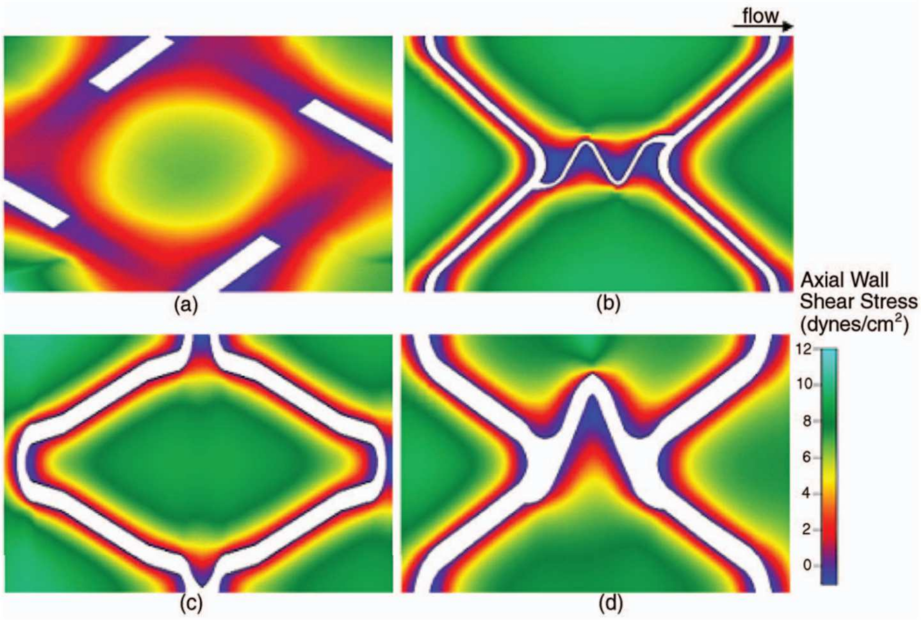

Figure 2.1: Axial WSS taken at the mean flow rate for (a) the Wallstent, (b) the Bx Velocity stent, (c) the Aurora stent, and (d)the NIR stent during the accelerating phase of the flow cycle (Duraiswamy 2009).

Jiménez and Davies (2009) focused into the specific design of stent struts, their shape, and dimensions, as the strut geometry promotes blood separation and consequent recirculation zones. During the research both steady and unsteady (pulsatile) flow simulations were conducted using a parabolic velocity profile and a Newtonian fluid model. Rectangular and circular cross-sectional geometries were considered with three different aspect ratio to establish a relationship between the strut geometry and the resulting flow characteristics (Fig. 2.2).

Local hemodynamic conditions were evaluated through several normalized parameter, including pressure field, separation zone cross-sectional area, separation distance, wall shear stress, and shear rate.

The implementation of a circular cross-section, as opposed to the rectangular one, resulted in a reduction of downstream separation distance up to 44% , of separation areas by at least 70%, and of maximum wall shear stress up to 50%, with even greater decreases when varying the aspect ratio. The study concluded, supported also by clinical data, that depending on the geometric characteristics of the stent strut cross-section, the local flow environment can promote, retard, or inhibit endothelialization.

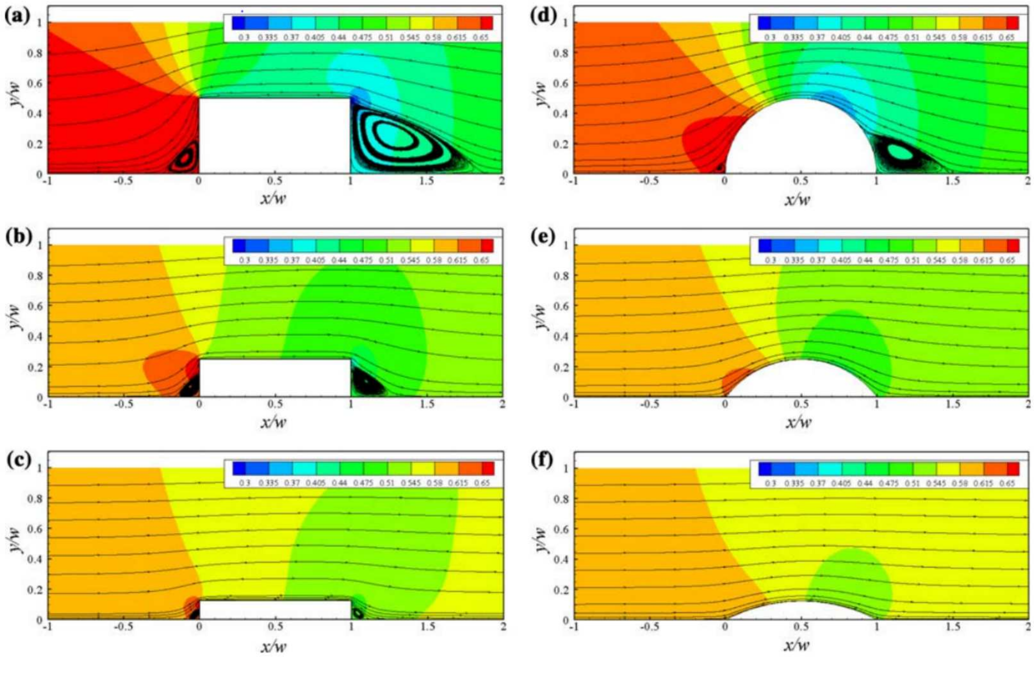

Figure 2.2: Streamlines in the foreground of a nondimensional pressure p* flow field, expressing a ratio between static and dynamic pressure, in the vicinity of (a)–(c) rectangular and (d)– (f) circular arc stent struts for aspect ratios, 2:1, 4:1, and 8:1 (Jiménez and Davies 2009).

In addition to the stent and strut design, other important variables include stent placement, length and configuration, eventual stent overlapping and flexibility with respect to arterial curvature (Koskinas 2012).

2.2 In-Vivo Studies

Over the past two decades, numerous $in-vivo$ studies have been conducted to assess the correlation between low and oscillatory wall shear stress and conditions, such as atherosclerosis, in-stent restenosis, and, more broadly, neointimal growth.

Peiffer et al. (2003) carried out a systematic review on CFD derived metrics and plaque distribution relation; the findings were based mainly on human and porcine arteries reconstruction, both treated in an anatomically realistic and relevant manner. Excluding some outliers, a combination of WSS, OSI and RRT was used to characterize the disease progression. By considering exclusively the two most popular data processing methods, thresholding and visual comparison maps, the analysis supports the existence of a correlation between the above three hemodynamic parameters and restenosis.

2.2.1 Human Studies

Stone et al. (2003) were the first to relate the baseline endothelial shear stress value to the human arterial behavior six months later stent implantation. The 3D anatomy of the artery was reconstructed through coronary intravascular ultrasound (IVUS) and biplane coronary angiography. These data were subsequently used to perform a steady state Newtonian flow simulation. The arterial segment were mapped and their lumen surface divided into independent rectangular patches; each patch had an endothelial shear stress (ESS), lumen radius, outer vessel wall radius, and plaque thickness values (Fig. 2.3). In the native segments of the artery, the following patterns emerged.
-Pathologically low ESS regions displayed progressive atherosclerosis along with outward or positive remodeling.
-Physiological ESS regions showed minimal alterations in vascular morphology.
-Increased ESS regions underwent outward remodeling without progressive atherosclerosis.
In the stented sections of the artery, neointimal hyperplasia was evident, resulting in a reduced lumen radius and increased shear stress across all baseline levels. While the impact of endothelial shear stress on in-stent restenosis remains somewhat uncertain, a clear inverse relationship between ESS and neointimal growth was observed. Areas with higher baseline ESS exhibited more significant increases in intimal-medial thickness and outer vessel radius.

Rikhtegar et al. (2012) conducted a study on thirty left and right coronary arteries with patient specific geometries, virtually removing the possible plaques and finally

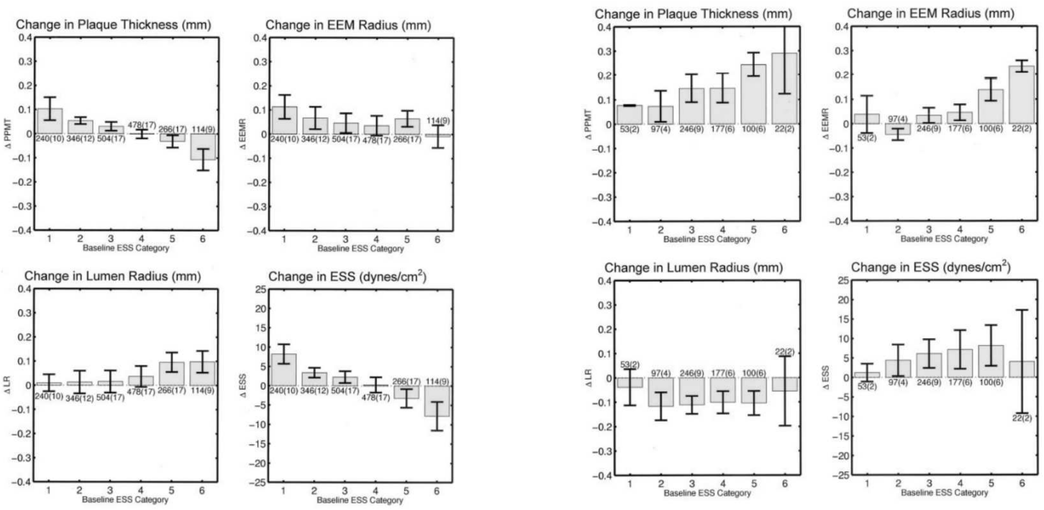

(a) Native Arteries

(b) Stented Arteries

Figure 2.3: Outcomes as function of shear stress baseline categories, Within each ESS category, the total area of the respective regions and the number of regions, in parentheses, are displayed on each bar.The y-axis displays the change in the vascular variable after 6 months. (Stone 2003)

using numerical simulation of the blood flow to evaluate the properties of the main hemodynamic parameters. Transient flow reproducing the systolic and diastolic flow characteristics was applied as inlet condition, the blood was modeled as Newtonian fluid and two cardiac cycle were evaluated. The statistical analysis performed on the computed data concerned time-average wall shear stress (TaWSS), its magnitude, the oscillatory shear index (OSI) and the relative residence time (RRT). The TaWSS predicted more accurately the critical regions as compared to the other two parameters, suggesting that a low wall shear stress is a crucial factor for plaque development. On the other hand, the RRT showed a significantly higher positive predictive value as compared to TaWSS since it accurately predicted plaque location near the proximal end of arteries. Although it is essential to consider the time-dependent directional changes in wall shear stress, RRT (and OSI) represent just two of the many potential time-dependent shear stress parameters which can be used.

Colombo et al. (2021) investigated the impact of local hemodynamics on the vessel lumen remodeling, focusing on human superficial left femoral artery (SFA) treated with self-expandable stents. The study involved patient-specific CFD simulations, employing geometrical domains reconstructed from computed tomography images obtained during the initial follow-up one week after stent implantation. The local hemodynamics thus calculated was subsequently linked to the lumen remodeling observed at the one-year follow-up. This analysis encompassed both global and local level analyses, including demographic and clinical data, as well as hemodynamic parameters. The shear stress based on data from all lesions were combined to establish objective thresholds for disturbed shear stress, namely 1.05 Pa for TAWSS, 0.20 for OSI, and 1.68 Pa^{-1} for RRT. Additionally, the percentage of surface area exposed to TAWSS (OSI and RRT) below or above these thresholds was computed. The findings of this study suggest that in human SFA lesions exists a connection between the TaWSS at baseline and the lumen remodeling at 1-year follow-up. Specifically, lower baseline TaWSS values and larger surface areas exposed to lower baseline TaWSS were both associated with a greater reduction in lumen area. In contrast, no statistically significant correlations were observed between the other examined hemodynamic descriptors (i.e., OSI and RRT) and changes in lumen area (Fig. 2.4). At the local level of analysis, a promising positive predictive value (PPV) of 44.8%, higher than the values for OSI or RRT, was determined for low TAWSS. The PPV for low TAWSS, compared to previous studies, may be attributed to preliminary spatial correlation analysis aimed at eliminating auto-correlated or mutually influenced data points, as well as a more advanced reconstruction of geometries and patient-specific boundary conditions.

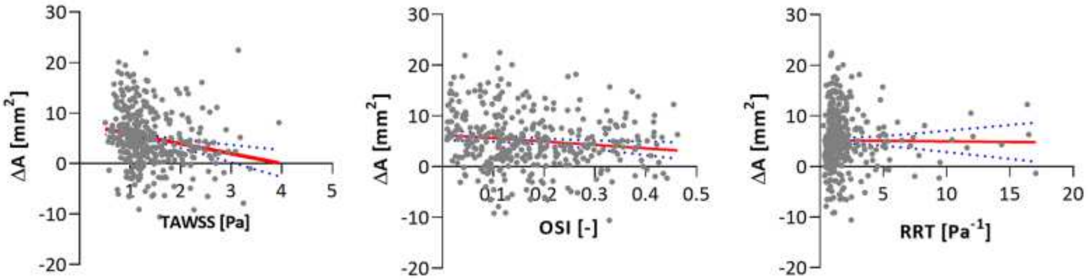

Figure 2.4: Linear regressions between each hemodynamic descriptor and change in lumen area (Colombo 2021a).

2.2.2 Animal Studies

$In - Vivo$ animal studies enable a more comprehensive examination and data extraction, despite the inevitable differences in anatomical and geometrical properties.

LaDisa et al. (2005) conducted a study on stented rabbit iliac arteries. Sixteen 16 mm slotted tube stents were implanted, and two different periods after stent implantation were examined: 14 days and 21 days. Following the prescribed time periods, a histological analysis was conducted, and an accurate geometric reconstruction was achieved using a microfocal X-ray CT imaging system. These reconstructed arteries were then employed for conducting computational fluid dynamics (CFD) simulations, with blood modeled as a Newtonian fluid. The inlet velocity profile for the simulations was derived from the $in - vivo$ iliac artery waveform.

The study examined the changes in spatial distributions of wall shear stress and its gradient within the stented region, calculating localized averages based on five adjacent control volumes at seven axial locations. To accommodate the elliptical shape of consecutive transaxial slices, a normalization factor was introduced. A strong correlation emerged between areas of low wall shear stress predicted by the artery immediately after stent implantation and the sites of neointimal hyperplasia in the histological sections. The examined histological sections (Fig. 2.5) revealed more pronounced tissue growth within regions characterized by low wall shear stress when compared to areas with higher values. Remarkably the critical threshold value consistently ranged around 0.5-0.6 Pa.

The distributions of WSS exhibited an inverse relationship with changes in vessel radius for all rabbits, with a decrease in the slope severity of this relationship between 14 and 21 days. The overall findings highlight a temporal dependence on the relationship between shear stress indexes and neointimal growth.

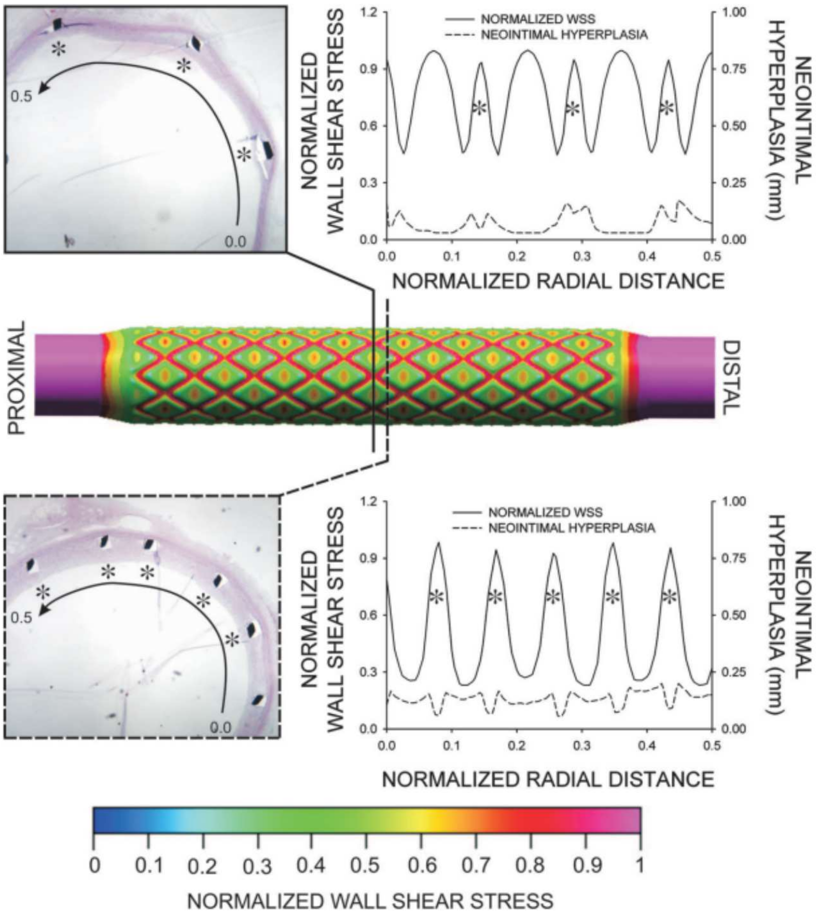

Figure 2.5: Predicted areas of WSS in the computational domain (middle) immediately after stent deployment and the localization of neointimal hyperplasia in histological sections (top and bottom) 14 days after implantation verify the correlation (J. F. e. a. LaDisa 2005).

Morlacchi et al. (2011) conducted a study similar to that of LaDisa et al. (2005). In this study, six healthy pigs underwent stent implantation in both the right coronary artery (RCA) and the left anterior descending artery (LAD). The stented segments were then excised, treated, and scanned at 6 hours, 4, 7, 14, 21, and 28 days post-implantation. Out of the 12 stents reconstructed using micro-CT, one stent was selected for further numerical analysis, specifically the one retrieved after 14 days, to achieve a good balance between neointimal hyperplasia and CT image quality. Both steady (for WSS) and transient (for OSI) simulations were performed. Blood was treated as an incompressible fluid, with viscosity characterized using the Carreau model. The velocity waveform for a porcine RCA was sourced from the literature, and a parabolic velocity profile was imposed at the inlet. In the case of steady-state simulations, the peak value was determined as the mean velocity of the transient velocity profile.

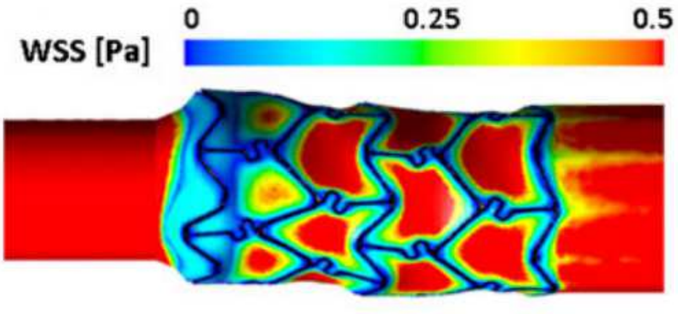

Figure 2.6: Spatial distribution of WSS magnitude over the arterial wall (Morlacchi 2011).

The results show a degree of neointimal growth at 14 days heavily influenced and proportional to the stent protrusion. The position along the stent also seems to affect the tissue thickness, with the proximal region of the stent being the most critical in terms of restenosis. The six devices explanted at 14, 21, and 28 days revealed the effects of time after deployment on the restenosis rate. The most substantial increase in neointimal thickness was observed in the third week of implantation, which showed a much higher value of neointima than the second week. The discrepancy of this result with respect to previous studies on animals could be attributed in part to differences in velocity profiles, but primarily to variations in geometry and diameter of the vessels. Specifically, the coronary arteries of pigs have a diameter of 3mm, whereas the iliac arteries of rabbits are less than 1mm in diameter.

Hemodynamic parameters were plotted at seven cross-sections along the arterial wall within the computational domain. Figure 2.7 shows that uneven tissue growth strongly correlates with regions characterized by low wall shear stress (WSS) and low axial wall shear stress, particularly where WSS falls below 0.5 Pa and the oscillatory shear index (OSI) values are notably high, typically exceeding 0.2.

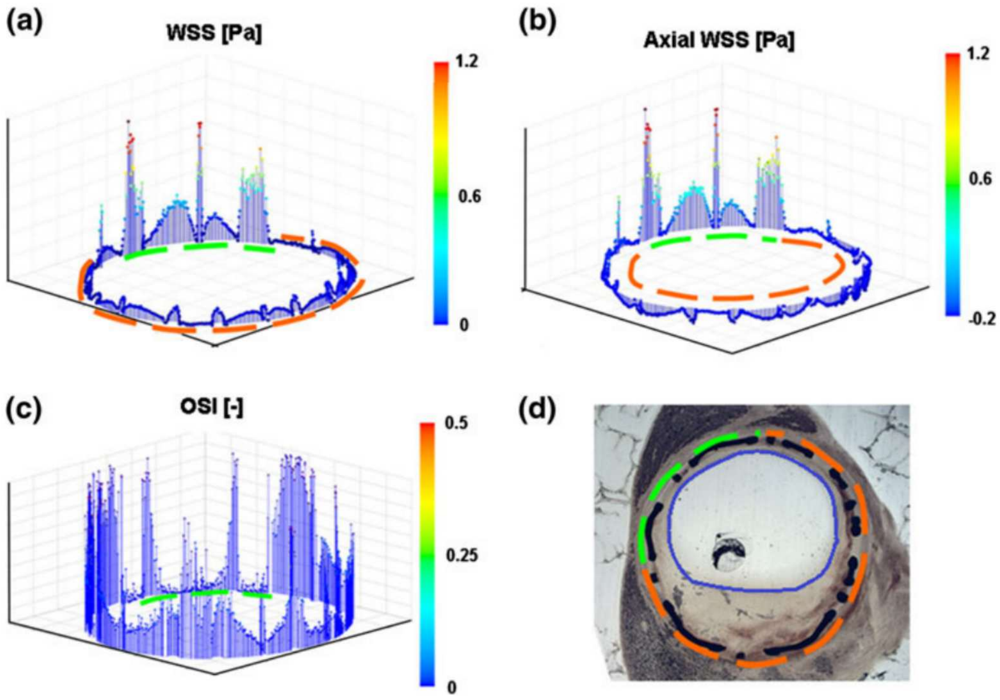

Figure 2.7: (a) WSS , (b) axial WSS, (c) OSI, calculated for the initial slice of the proximal part of the stent. The dashed orange lines indicate zones characterized by WSS lower than 0.5 Pa and high OSI. (d) Histological image with markedly non-uniform neointimal growth, blue line delineates the new lumen after occurrence of restenosis. (Morlacchi 2011).

2.3 Numerical Studies

De Santis et al. (2008) proposed a basic iterative remodeling algorithm that utilized a binary threshold of 0.5 Pa to determine whether intimal thickening occurred at a specific location. In cases where the steady-state flow simulation identified a wall shear stress (WSS) less than 0.5 Pa at a location, intimal thickening was simulated by reducing the lumen radius. This operation was repeated iteratively until no areas subjected to restenotic stimuli were found (as shown in Fig. 2.8). The considered axisymmetric geometry included a segment of an artery with a length of 3.5 mm and a radius of 1.5 mm. Two stent struts, each with a width of 0.15 mm and an inter-strut distance of 0.5 mm, were included on this segment. The quadrilateral mesh used was refined near the vessel wall. The iterative procedure has been observed to converge, confirming the existence of an inverse correlation between wall shear stress (WSS) and vessel remodeling. In cases where low wall shear stress zones were present within a large vessel, lumen narrowing occurred, resulting in subsequent velocity increase. This velocity increase was determined by the fixed flow rate imposed through the section, and led to an overall shear stress within the artery.

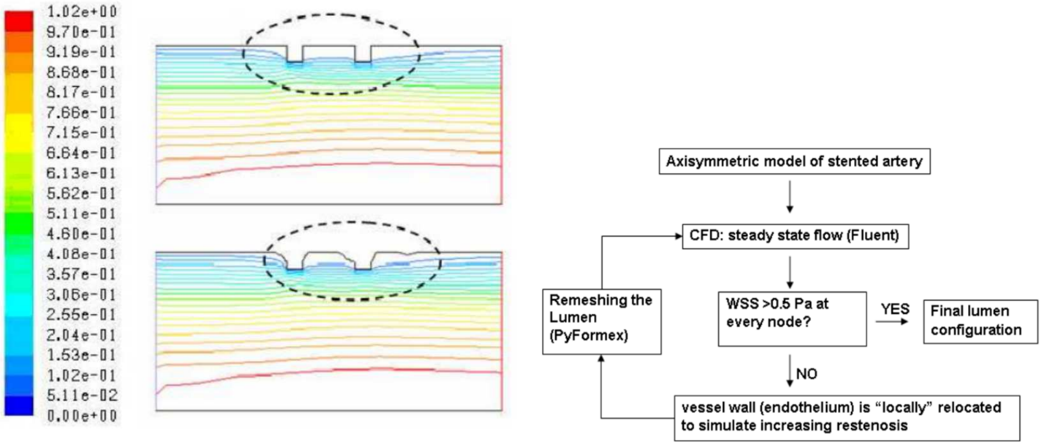

Figure 2.8: Contours of velocity magnitude (m/s) at first and 35th iteration (left), iterative process scheme (right) (De Santis 2008).

Caiazzo et al. (2010) proposed a first comprehensive approach to stent restenosis. Based the study on past $in-vitro$ and $in-vivo$ biological data, a two-dimensional multiscale model was assembled. The single-scale solvers were first independently developed, and later coupled together to form the complete modeling structure. The simulation included the following components:
-A Bulk flow solver modeling the blood flow as a Newtonian incompressible fluid and solving the Navier–Stokes equations, through the Lattice Boltzman method was implemented.
-An agent based model simulating the smooth muscle cell (SMC) dynamics, namely, the cell growth, the cell cycle and physical and biological cell–cell interaction.

-A Finite Difference scheme computing the drug diffusion within the cellular tissue, described using a generic anisotropic diffusion law, in order to simulate not only a bare metal stent but also a drug eluting stent.

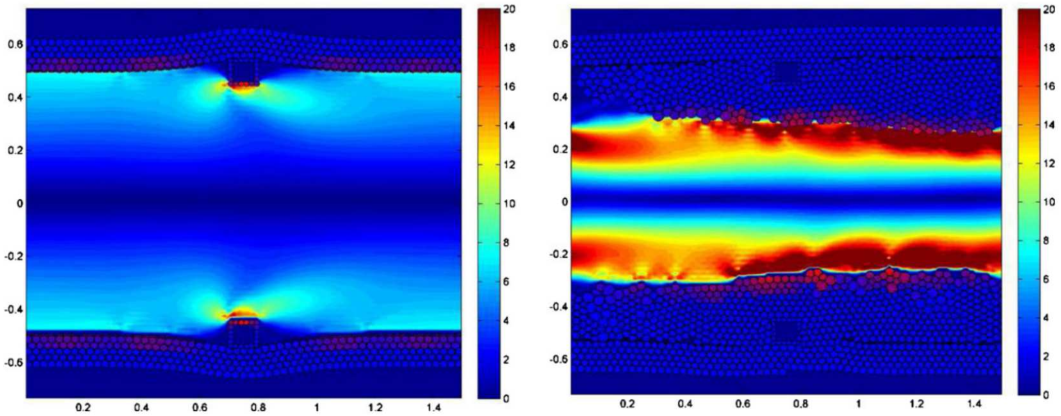

Figure 2.9: Initial condition for the multiscale model (left). The same domain at 28 days post-stent deployment (Right). Colour bars refer to the wall shear stress within the lumen in Pascals (Caiazzo 2011).

The benchmark geometry for the 2D simulations consisted of a vessel with a length of 1.5 mm, an internal width of 1 mm, and an external width of 1.24 mm. Two square struts with a side length of 90 µm were deployed. Within the biological solver, a wall shear stress (WSS) threshold was set for simulating smooth muscle cell (SMC) proliferation. The real physiological threshold value of 0.4 Pa, taken from the literature, corresponded to a value of 2.76 Pa in the considered 2D geometry. The simulation was carried out under steady flow conditions and lasted for an equivalent of 72 days, with values extracted each hour, resulting in a total of 1700 extracted instants. The results were promising when compared to real data. Neointimal growth ceased around the 28-day mark, resulting in a final thickness of 0.2 mm, corresponding to approximately a 40% occlusion. The peak proliferation appeared to occur around the 20-day mark. The data computed immediately after the stent deployment as compared to those observed 28 days later (Fig.2.9), indicate that the developing neointima causes a reduction in lumen diameter and an increase in wall shear stress. Due to the SMC ruleset, according to which the SMC agent proliferation is inhibited by high shear stress, an equilibrium is reached once the neointimal growth causes shear stress to exceed a certain threshold, and further proliferation ceases (Fig. 2.10).

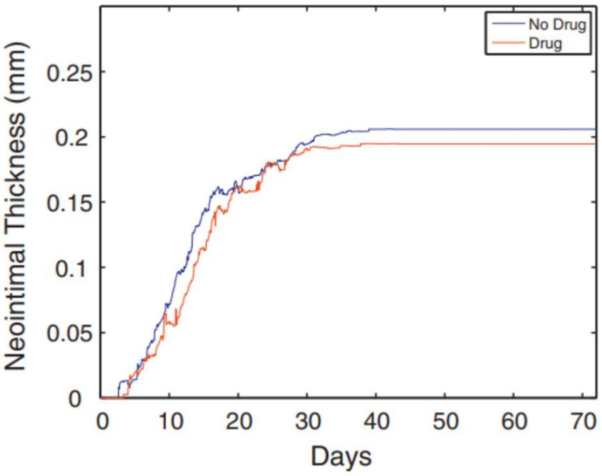

Figure 2.10: Neointimal thickness from 0 to 72 days, from bare metal and drug eluting stents (Caiazzo 2011).

In the last years, numerous studies utilized the Caiazzo model to conduct more detailed investigations. These studies explored various aspects, including different stent strut sizes, geometries, and deployment depths, as well as a more in-depth analysis of smooth muscle cell proliferation and re-endothelialization speed.

Tahir et al. (2011), carried out CFD simulations using two different rectangular strut of 180 µm and 90 µm thickness, respectively, and a 180 µm circular strut. The stents were embedded in the vessel walls at various depths ranging from 70 to 130 µm. For the sake of comparison, an $in-vivo$ dataset was compiled, consisting of more than 500 histological sections of stented porcine coronary arteries. This dataset included data on neointimal growth and the magnitude of vessel wall damage assessed through the Gunn injury score (Gunn 2002). This particular database can be usefully used as a benchmark for in-stent restenosis simulations (Fig. 2.14 left).
The models consistently reached a wall shear stress threshold value, resulting in a nearly constant final neointimal thickness, regardless of strut size or deployment depth, with an almost symmetrical neointimal growth curve, in contrast to experimental evidence. In the case of the circular cross-section strut, there was a decrease in the growth rate (Fig. 2.11), accompanied by delayed neointimal growth. This behaviour is likely due to the presence of fewer recirculation zones in the vessel. However, neglecting the poor final endpoint results, the computations predicted a early peak proliferation in case of deep injury/stretch and exhibited qualitative patterns in accordance with the $in-vivo$ data.

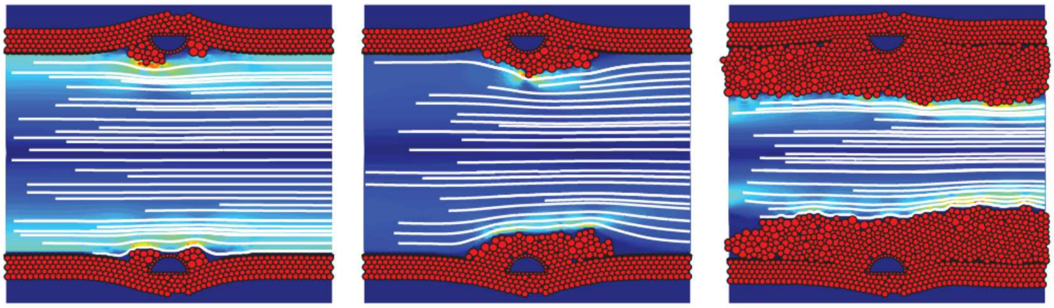

Figure 2.11: Simulation results of a rounded strut (180 μm) deployed at 90 μm, neointimal growth after 7, 14 and 28 days after stent deployment (Tahir 2011).

Tahir et al. (2014) carried out additional simulations, using the $in-silico$ Caiazzo multiscale model, to investigate the impact of different re-endothelialization speed on neointimal growth. These simulations have been based on a new set of proliferation rules in the agent-based model for smooth muscle cell, along with interpolated data from Nakazawa et al. (2010), to approximate the time distribution of a functional endothelium recovery. Notably, neointimal growth was observed to be not directly governed by the average wall shear stress but rather by its effect on nitrate production (Guo and Kassab 2009). Three re-endothelialization cases were modelled in order to investigate the effect of functional endothelium recovery rate on the restenotic lesion development.

The lesion growth rates, evaluated through the steepness of the curves in figure 2.12b, were directly proportional to the injury score caused by the stent implantation; moreover, the influence of a functional endothelium led to different end points for all the simulations. These results agree qualitatively with the $in-vivo$ data. Regardless of the fact that porcine arteries response to injury shows similarities with the human arteries, caution must be paid when transfering the knowledge gathered from a healthy porcine vessel to the behaviour of diseased human arteries.

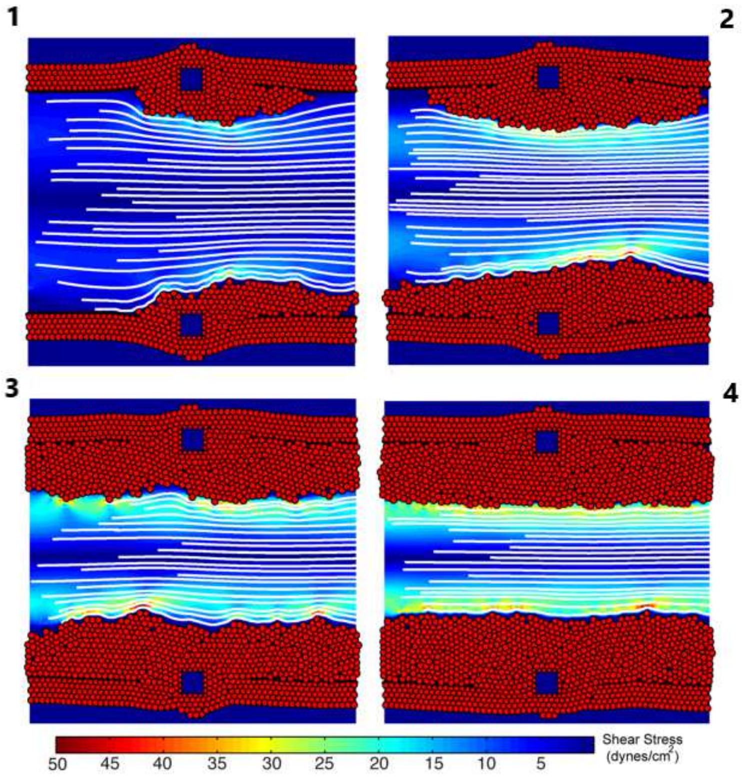

(a) Neointimal growth after 50 days post stenting, showing SMC growth and flow streamlines, struts were deployed at a depth of 110 mm (Tahir 2014)

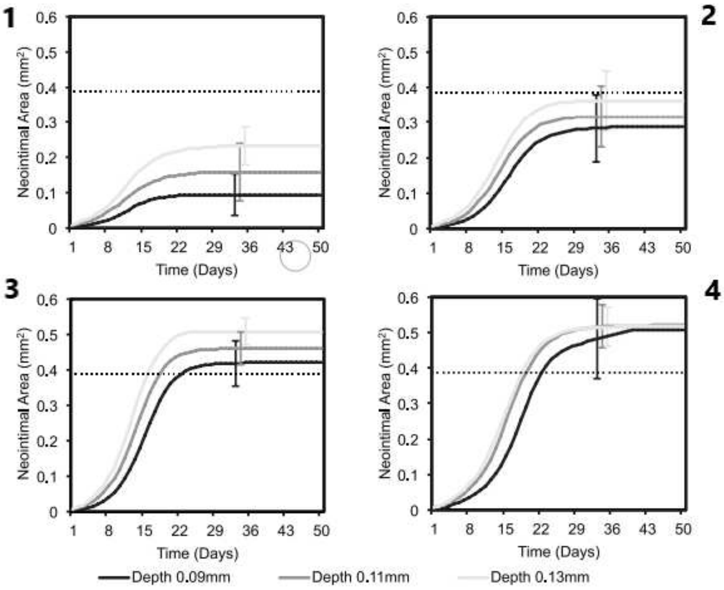

(b) Neointimal area as a function of time, black dotted line represents the 50% lumen occlusion point according to the domain dimensions (Tahir 2014).

Figure 2.12: (1) 59% functional endothelium at the third day, 100% after 15 days post stenting. (2) 59% functional endothelium at the third day, 100% after 23 days post stenting. (3) 0% functional endothelium right after stenting, 100% after 23 days post stenting. (4) Previous result, Tahir(2011).

Zun et al. (2017) conducted the most complete simulation currently available in the literature. The base model remained that proposed by Caiazzo (2010), complemented with the advanced smooth muscle cell proliferation rules introduced by Tahir (2014). However, the geometry consisted of a 3D vessel with internal and external elastic lamina specifically modeled to simulate more correctly injury score effects and endothelial interactions.

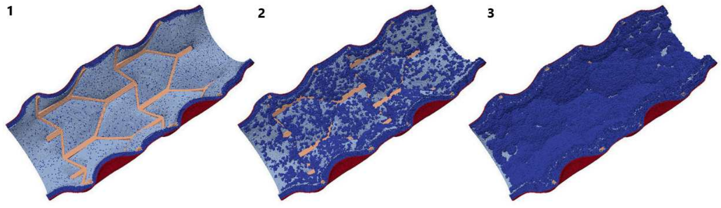

(a) Neointima proliferation for IS 3; (1) vessel right after stenting; (2) 1 week after stenting; (3) 2 weeks after stenting (Caiazzo 2011).

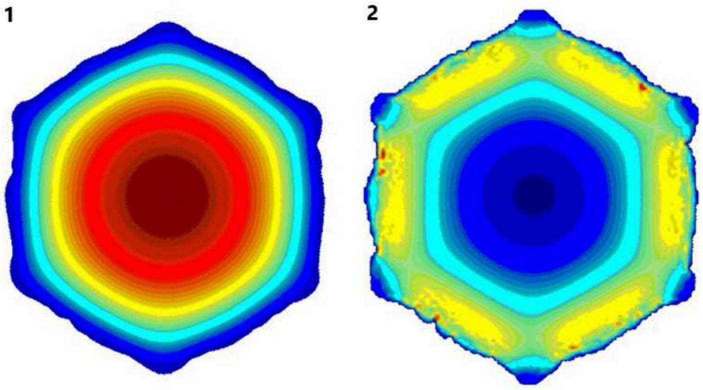

(b) Sample slices of the blood flow solution; (1) velocity; (2) shear stress (Caiazzo 2011).

Figure 2.13: (a) Sample of 3D geometry and cell proliferation, (b) example of vessel section Zun 2019.

All the simulations of the study were conducted in a 2.8 mm diameter vessel with an open cell 8 mm stent segment. The default setup involved a 0.2 mm strut width, a 15-day re-endothelialization speed, and an injury score of 2 on the Gunn scale. To better assess the significance of each parameter, numerous simulations were conducted, with only one parameter varied at a time. The results are summarized as follows:

Injury Score effect. The results agreed qualitatively with the experimental data from Tahir (2011) (Fig. 2.14 left). However, the neointimal thickness was lower than in real arteries, a common outcome of many simulations, possibly due to the exclusion of the extracellular matrix, a significant component of real in-stent restenosis. After a re-endothelialization period of 15 days, the growth at the vessel wall interface practically ceased, although some growth continued within the bulk of the neointima (Fig. 2.14 right).

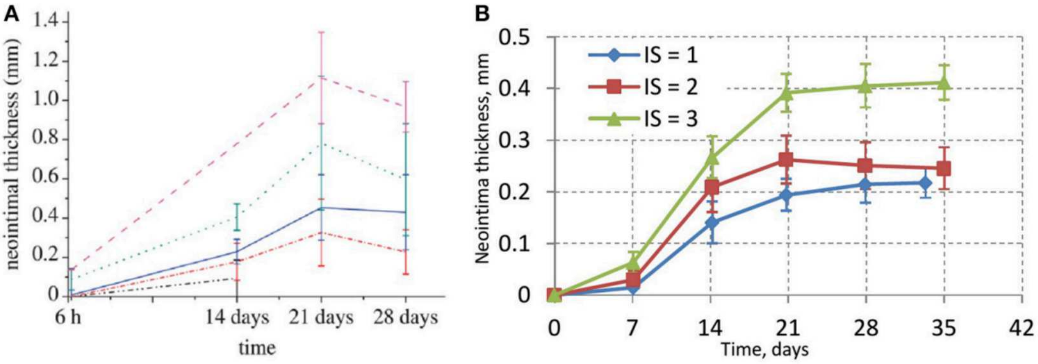

Figure 2.14: $In - vivo$ experimental data for neointimal growth-reproduced from Tahir Tahir 2011(left), simulated values of neointimal thickness (right)(Zun 2019), various injury scores are depicted.

Re-Endhtelialization speed effect. Three different re-endothelialization speeds were evaluated: fast (10 days), normal (15 days), and slow (20 days). In all cases, a linear endothelial cell growth model was considered, starting at 59% after three days and reaching 100% after the chosen duration. The model proved to be highly sensitive to this parameter. It not only influenced the peak thickness but also the time required to reach it. The average neointimal thickness over the struts was 0.10 mm, 0.24 mm, and 0.69 mm for the 10-day, 15-day, and 20-day scenarios, respectively. The third case, with more than 50% occlusion, could be classified as actual an restenosis and should require additional treatment.

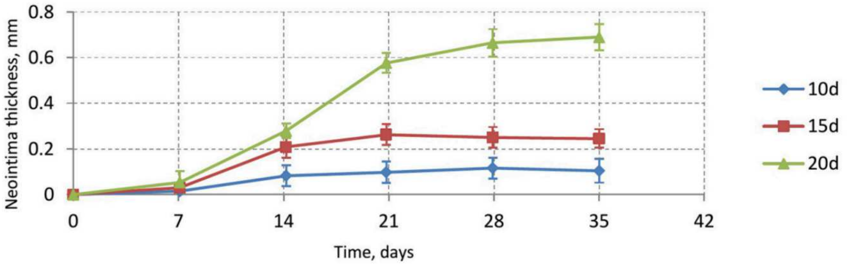

Figure 2.15: Neointimal thickness dynamics for IS2 and 0.2 mm struts for different re-endothelization speeds (Zun 2019).

Strut width effect. It is known that the amount of exposed struts should be minimized and larger struts can lead to more significant vessel wall injury. Nevertheless the neointimal growth showed just a slight positive correlation with strut width in the three cases. As mentioned previously, this could be attributed to the absence of the extracellular matrix and an underestimated thrombogenicity effect.

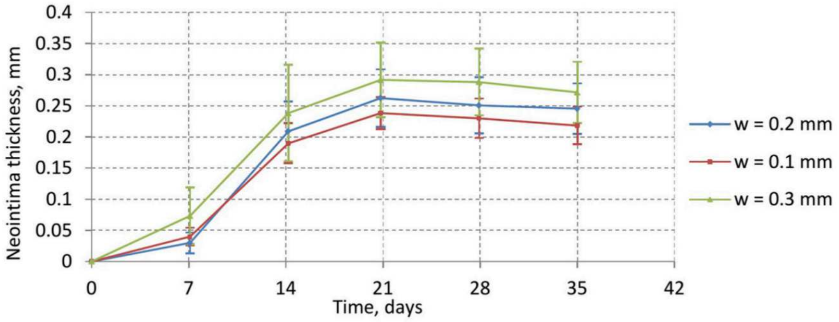

Figure 2.16: Average neointima thickness over struts for normal (w = 0.2 mm), wide (w = 0.3 mm), and narrow (w = 0.1 mm) struts (Zun 2019).

The numerical simulations reviewed in this chapter referred to the injury score scale introduced by Gunn in 2002 (Gunn 2002), which took into account both the potential rupture in various endothelial layers and the degree of angular deformation caused by the stent struts on the vessel wall. The score was determined as follows: 0, no deformation upon media; 1, deformation of the internal elastic lamina by <45°; 2, deformation of the internal elastic lamina by >45°; 3, rupture of the internal elastic lamina; 4, rupture of the external elastic lamina.

The neointimal thickness was evaluated following the same procedure used in in-vivo studies, selecting several points on different stent struts and averaging the results (Gunn, 2002; Zun, 2019). Finally, the advanced proliferation rules introduced were based on a study by Guo and Kassab (Guo and Kassab, 2009), who established a link between the presence of platelet endothelial cell adhesion molecules (PECAM-1), released by functional endothelial cells after stenting, and the relationship between wall shear stress and nitrate (NO) concentration.

Chapter 3

Materials and methods

As discussed in chapter 2, modelling neointimal growth correctly is an intricate problem. The more detailed simulations are computationally expensive, and their multiscale characterization require multidisciplinary knowledge. In this chapter, various modeling choices are discussed. The main idea is to design a conceptualized simulation based on the correlations found in the $in-vivo$ studies and compare the results with more sophisticated blood flow simulations.

3.1 Design of the numerical test

This section focuses on the simulation setup, including geometry, mesh properties, and boundary conditions. The model is designed to achieve the correct balance between the simplicity of the simulation and the fulfilment of realistic results. For this purpose, we consider the key anatomical properties of flow within a vessel and evaluate the effects of the hemodynamic parameters introduce in chapter 1 and 2.

3.1.1 Geometry and mesh

The present simulations were mostly conducted on a straight cylindrical vessel with a 4 mm diameter and four diameter length (table 3.1), simulating an idealized region of coronary arteries (CA). Additionally, we utilized a 6 mm diameter geometry, mimicking a left femoral artery (LFA), to evaluate the effects of different velocity profiles and the significance of OSI and RRT indexes, defined by equation (1.2) and (1.3). The axial symmetry of the flow within a cylinder is exploited to reduce the computational domain by three-quarters.

The investigated stent was one of the most commonly used and commercially available, consisting of an open-cell modular structure formed by intertwined cylindrical wires, half the vessel's length in size and placed halfway through the vessel's length. The circular cross-section strut thickness has been fixed at 90 μm, and was embedded in the vessel wall for half the diameter. As previously mentioned, most of the CFD simulations available in literature considered a thicker strut (180 μm), but nowadays stent wires are becoming thinner. The importance of strut geometry and width has already been discussed in Jiménez and Davies (2009).

Type	Diameter (mm)	Length (mm)	Stent Length (mm)
Coronary Artery	4	16	8
Left Femoral Artery	6	24	12

Table 3.1: Summary of the different geometries

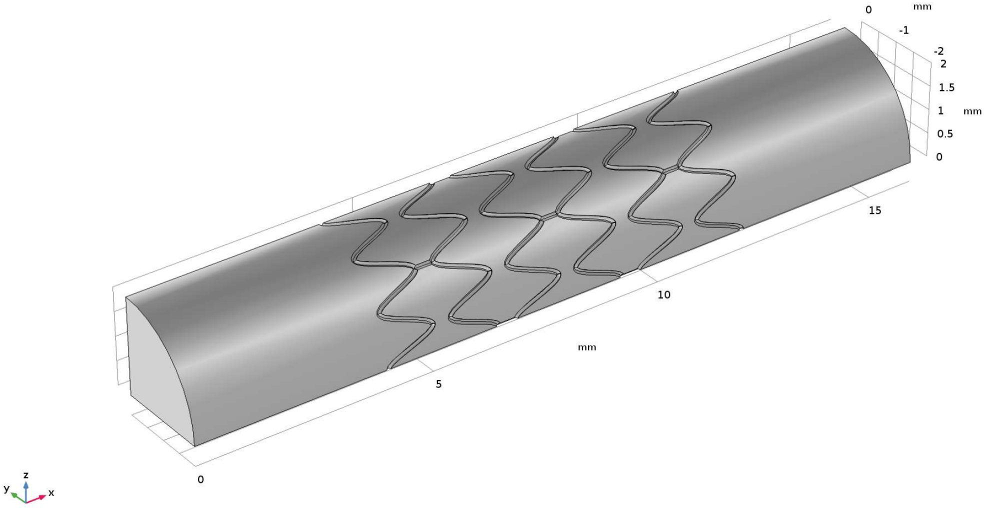

Figure 3.1: Vessel geometry with an open-cell stent, of 4 mm diameter.

The simulation setup (Fig. 3.1) and the meshing have been conducted using COMSOL Multiphysics® software. A free tetrahedral mesh has been applied to the entire geometry, with mesh size refinement implemented in both the vessel wall and stent strut boundaries (Fig. 3.2). Additionally, boundary layers have been added to obtain more detailed results in the near-wall section. The mesh refinement has been chosen to ensure mesh independence of the results while limiting the computational time and the amount of data to be extracted for each computation. The most refined mesh was used for the stationary simulations, while time-dependent simulations were conducted using coarser meshes, one for each diameter size. A remeshing test carried out for the time-dependent simulation of the coronary artery confirmed the mesh independence of the coarser meshes eventually adopted for the simulations. The properties of these meshes are reported in Table 3.2.

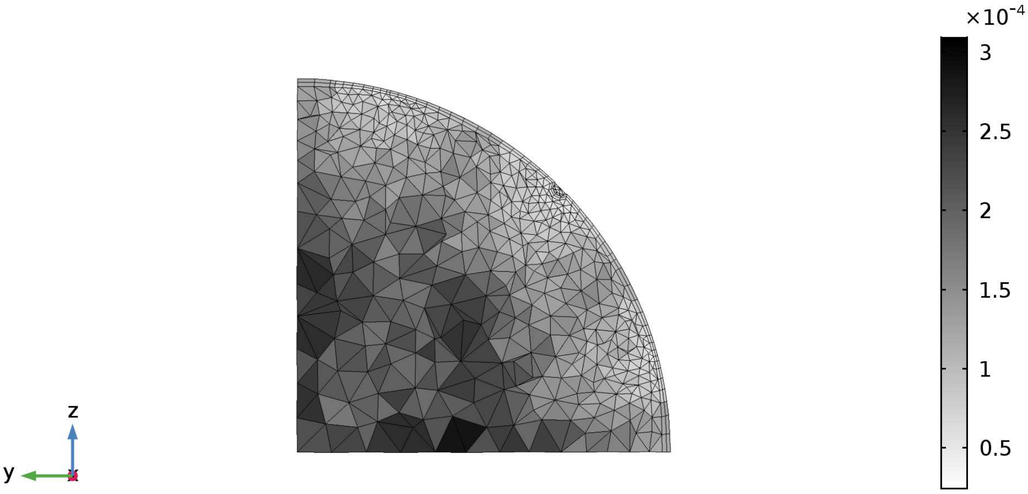

(a) y-z view, cut at x=8mm.

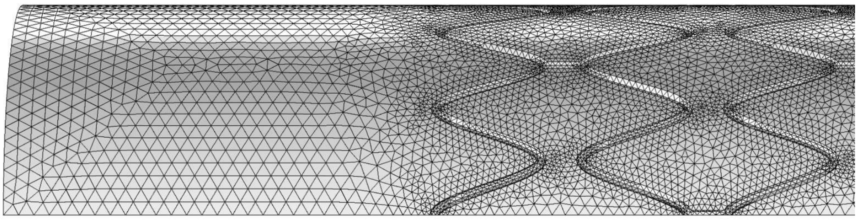

(b) x-z view.

.

(c) Element Quality Histogram, 0 to 1, left to right.

.

Figure 3.2: Mesh features for the stationary simulations carried out in a 4 mm vessel. a) cross-section transect; b) view in the longitudinal x-z plane; c) element quality histogram.

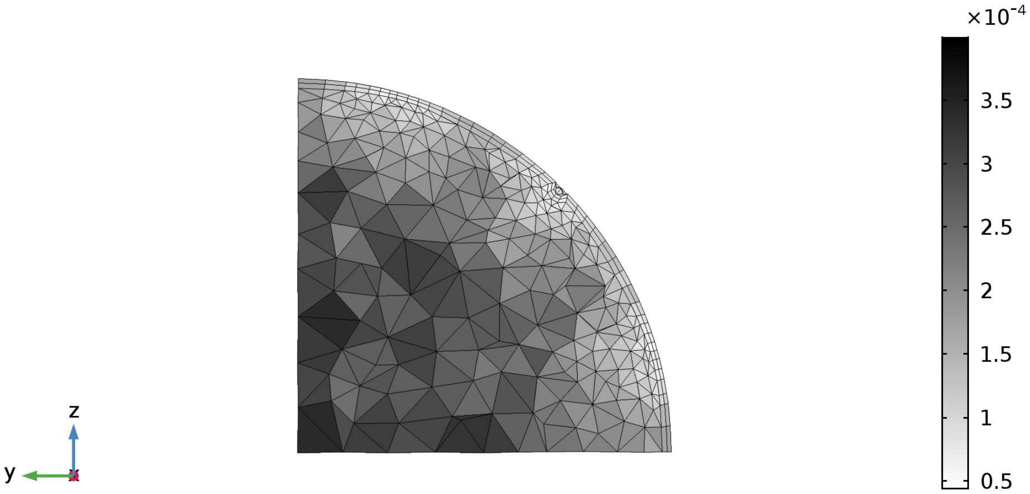

(a) y-z view, cut at x=8 mm.

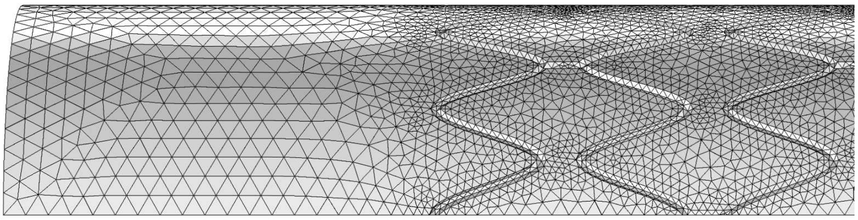

(b) x-z view.

.

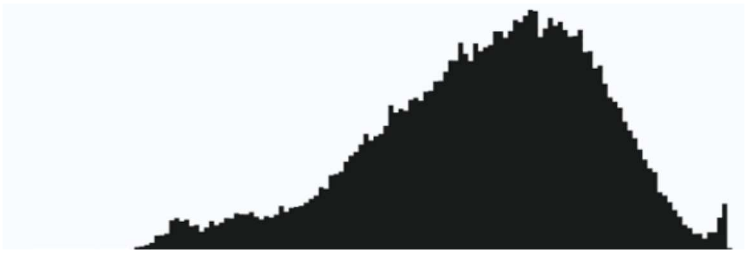

(c) Element Quality Histogram, 0 to 1, left to right.

.

Figure 3.3: Mesh features for the time dependent simulations carried out in a 4 mm vessel. a) cross-section transect; b) view in the longitudinal x-z plane; c) element quality histogram.

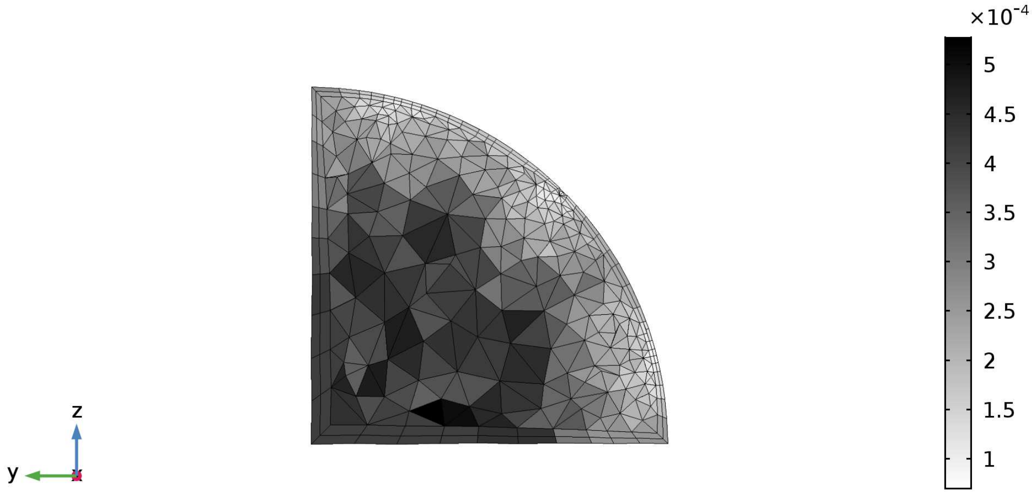

(a) y-z view, cut at x=12 mm.

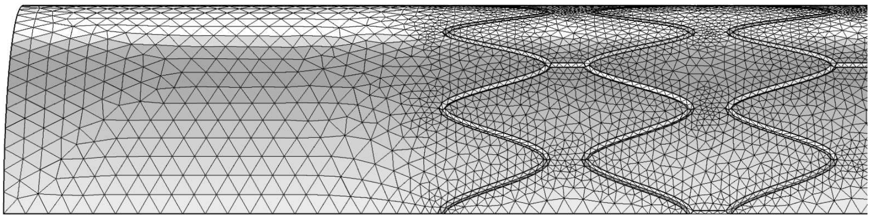

(b) x-z view.

.

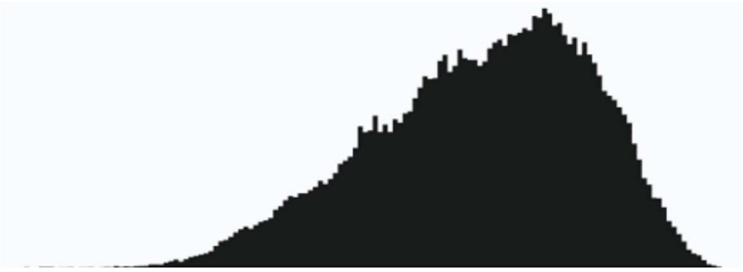

(c) Element Quality Histogram, 0 to 1, left to right.

.

Figure 3.4: Mesh features for the time dependent simulations carried out in a 6 mm vessel. a) cross-section transect; b) view in the longitudinal x-z plane; c) element quality histogram.

Mesh Information			
	Stationary (4mm)	Time Dependent (4mm)	Time Dependent (6mm)
Number of elements	323043	124870	137502
Tetrahedral elements	281533	105554	111686
Edge elements	2921	2040	1885
Average element quality	0.6625	0.6475	0.6443

Table 3.2: Summary of different mesh properties

3.1.2 Time Regime and boundary condition

A no-slip and no-flux boundary condition was imposed on the vessel wall, which includes the blood-endothelium and blood-stent interfaces. Taking advantage of the axial symmetry of the flow, we applied a symmetry condition to the internal boundaries to maintain the correct velocity profile. The vessel wall was treated as rigid (Jiang 2015). This approach implies a quite simplified treatment of the vessel interactions with both the fluid and the metal stent structure. However, it is worthwhile to note that medium-sized arteries typically have thicker, stiffer walls which are less susceptible to deformation due to blood motion. At the outlet of the vessel model, a zero pressure condition was imposed to achieve a steady outlet flow. Any backflow was absent or negligible during the simulations.

Inlet Conditions

The effect and interplay of inlet conditions and rheological models have been extensively studied by Jiang et al. (2015). In the present thesis four different inlet velocity conditions have been employed, depending on the time regime (either stationary or pulsatile) and the vessel geometry. A parabolic velocity profile was applied normally to the inlet surface to simulate the Poiseuille flow characteristic of flows within a pipe and to better mimic fully developed flow conditions. For the coronary arteries, inlet conditions have been extracted from Jung et al. (2005). The average and maximum values of the stationary velocity profile were 0.22 m/s and 0.37 m/s, respectively.

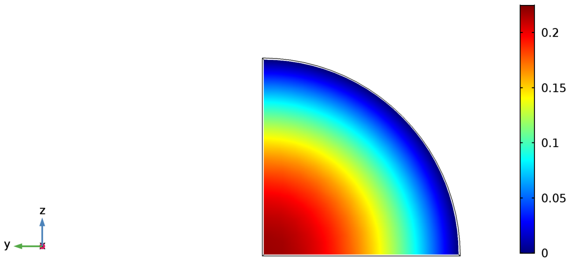

Figure 3.5: Parabolic velocity profile imposed at the inlet for the average stationary velocity of 0.22 m/s. The colorbar expresses the velocity in m/s.

The pulsatile flow condition for the 4 mm vessel was obtained through simple interpolation of a typical signal of the cardiac cycle, as depicted in Fig. 3.7. The left femoral artery velocity profile was derived from Masuda et al. (2013). This specific study case was chosen because of the characteristic negative velocity present near the end of the cycle, which can have a significant effect on the oscillatory shear index. The time dependent simulations were carried out by imposing a periodic flow with a period T=0.735 s (Jung 2006). The simulations always lasted three cycles, with the first two having damped peaks to facilitate the final convergence. The results were evaluated exclusively for the third cycle. The time step imposed for the 6 mm vessel was is one-hundredth of the period length, and was doubled for the 4 mm vessel.

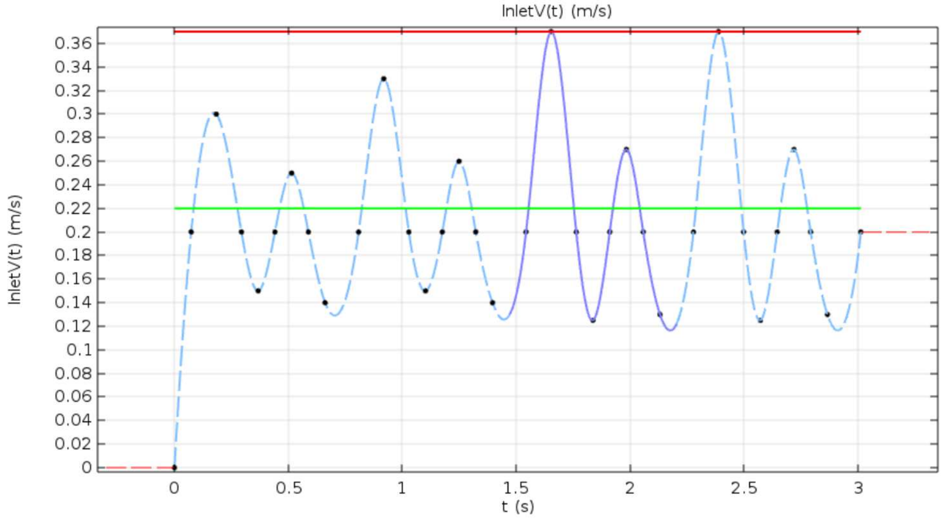

Figure 3.6: Pusatile Inlet condition imposed for the 4 mm vessel simulations. The green line denotes the average velocity; the red line corresponds to the maximum velocity.

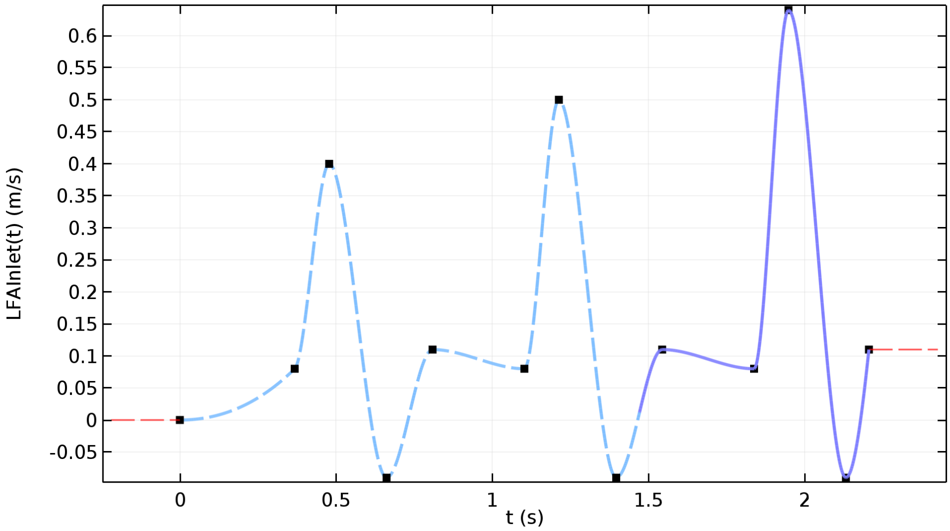

Figure 3.7: Pusatile Inlet condition imposed for the 6 mm vessel simulations.

3.1.3 Rheological Model

The majority of studies dealing with blood simulations modeled blood as a Newtonian fluid, as discussed in chapter 2. This is a reasonable approximation for the speeds and scales typical of stenosed vessel (Zun 2019). However, various studies (Jiang 2015, Conforto 2022) have shown a clear difference in distribution and size of low wall shear stress zone when implementing a non-Newtonian model, as the Carreau-Yasuda model with tweaked parameters.

In the Newtonian case, blood is modeled as incompressible, and homogeneous, with a density and viscosity equal to $\rho = 1060 kg/m^3$ and $\mu = 3.5 * 10^{-3} Pa \cdot s$, respectively. Generally, blood behaves as a non Newtonian fluid at low shear rates (less than 100 s^{-1}), while the instantaneous shear rate throughout a cardiac cycle varies from zero to approximately 1000 s^{-1} in several large arterial vessels. As showed in Figure 3.8 the blood flow shear rate range is relatively limited.

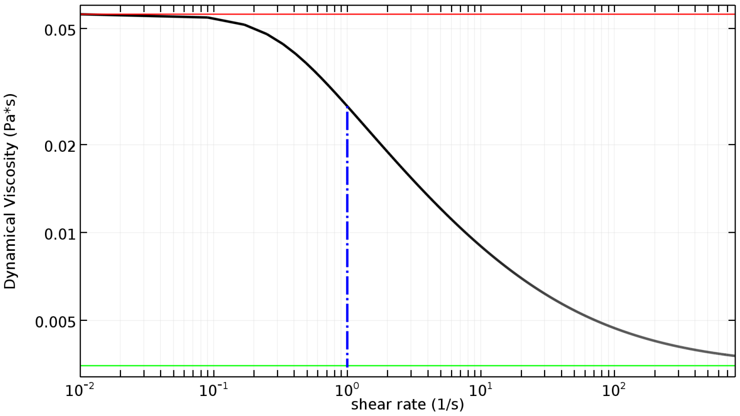

Figure 3.8: Carreau-Yasuda model, with the shear rate limit viscosities represented in green and red. The dashed blue line represent the minimum instantaneous shear rate reached in a cardiac cycle.

The Carreau-Yasude model introduces and additional term, relating the dynamic viscosity of the blood to the shear rate through the following power law expression

$$\mu = \mu_\infty + (\mu_0 - \mu_\infty) \left[1 + (\lambda \cdot \dot{\gamma})^2\right]^{\frac{n-1}{2}} \tag{3.1}$$

where μ_∞ and μ_0 are the infinite and zero shear rate limit viscosities, respectively, $\dot{\gamma}$ is the shear rate, λ is the relaxation time constant, and, finally, n is a power law index. The specific parameters chosen in the present work are reported in Table 3.3.

Parameter	Value (mm)
$\mu_0(Pa \cdot s)$	0.056
$\mu_\infty(Pa \cdot s)$	0.00345
$\lambda(s)$	3.313
n	0.3568

Table 3.3: Carreau-Yasuda model parameter (Conforto 2022)

3.2 Simulation Method

3.2.1 Fluid Flow Solver

The velocities profiles used in the various simulations, had a peak instantaneous velocities of 0.37 m/s for the coronary and 0.65 m/s for the left femoral artery. The corresponding values of the Reynolds number

$$Re = \frac{\rho \cdot U \cdot L}{\mu} \tag{3.2}$$

are around 500 and 1200, respectively, corresponding in both case to laminar flow conditions (Re<2000). Note in the case of the Carreau-Yasuda model, the value of μ_∞ is used to compute the Reynolds number.

Laminar flow solver

The default COMSOL laminar flow solver was used to resolve the governing equations. It is based on a fully coupled approach, allowing to compute all the unknowns, i.e., the velocity and pressure fields, in a single iteration. The solved equations are the continuity equation derived from the mass conservation principle and the Navier-Stokes equations. In the case of an incompressible and homogeneous fluid ($\rho = constant$), these equations read:

$$\nabla \cdot \vec{u} = 0 \tag{3.3}$$

$$\rho \frac{d\vec{u}}{dt} + \rho g \nabla h + \nabla p = \mu \nabla^2 \vec{u} \tag{3.4}$$

The default suggestion for solving large 2D and 3D models is the iterative generalized minimal residual method solver (GMRES). The memory requirement for an iterative solver, as opposed to direct solvers, scales linearly with the number of degrees of freedom of the system. The governing equations are solved implementing the default P1-P1 elements which are the simplest available. They perform interpolation of unknowns using piecewise linear polynomials. The choice of the solver has been guided by the same reasoning used for the mesh refinement; the computational cost and memory needed to utilize more complex elements and the corresponding interpolation functions is computationally time-consuming, and even less sustainable considering the numerous simulations needed in the analysis, given the aim to develop a robust but also efficient tool for helping the clinicians.

3.2.2 Endothelial Growth Model

The main objective of the thesis is to simulate reasonably the endothelial growth associated with stent implantation through a conceptualized approach. As we have seen in the chapter 2, the majority of $in - vivo$ studies have found a strong correlation between low wall shear stress regions and neointimal hyperplasia. More specifically, the critical regions are characterized by shear stresses smaller than 0.5 Pa. The idea thus consists of conceptualizing endothelial growth, and consequent lumen narrowing, simulating it iteratively by changing the local dynamical viscosity according to the values of the shear stress. The implemented iterative process consisted of the following steps: evaluate the blood flow field in the vessel; extract the spatial distribution of wall shear stress; individuate the near-wall nodes with a shear stress value below the threshold limit of 0.5 Pa; assign a significantly higher dynamical viscosity value to those specific nodes; repeat again the process restarting from the first step. The advantage of this procedure is that it does not need any remeshing of the computational domain, since the boundary changes are accounted for virtually by using an increased value of the local fluid viscosity wich lead to vanishing velocity values.

For the stationary simulations, this process-based model can be implemented directly through the COMSOL user interface. For any node near to the wall, where the computed shear stress is smaller than the threshold limit, the new viscosity is assigned according to the relation

$$\mu^* = \mu + \frac{0.5[Pa] - WSS}{0.5[Pa]} * 1000[Pa \cdot s] \qquad if \quad WSS < 0.5[Pa], \tag{3.5}$$

having assumed, as a first approximation, that the virtual increment of viscosity is proportional to the relative distance of the WSS from the critical threshold. clearly, this approach allow us to determine the final wall configuration whereby WSS is everywhere smaller than the critical values, but does not provide any information about the transitory which produces this configuration.

For the time dependent simulations, two possibilities have been explored to adjust iteratively the local viscosity, considering either the average or the maximum value of the local shear stress throughout the last periodic cycle of simulations, when stable flow field conditions are attained. In the first case, the average values is computed as:

$$TaWSS = \frac{1}{T}\int_0^T |WSS| dt = \frac{1}{T}\sum_i WSS_i \cdot \Delta t \tag{3.6}$$

where the time integral has been approximated numerical thorugh Matlab with a left Riemann sum, and the corresponding viscosity values for each node have been set equal to

$$\begin{cases} \mu = 0.00345[Pa \cdot s] & if \quad TaWSS > 0.5[Pa] \\ \mu = \frac{0.5[Pa] - TaWSS}{0.5[Pa]} \cdot 1000[Pa \cdot s] & if \quad TaWSS < 0.5[Pa] \end{cases} \tag{3.7}$$

The OSI and RRT parameters are also evaluated through Matlab, extracting the needed data provided by the last simulated temporal cycle. Finally, the neointimal thickness after each iteration is evaluated by averaging the radial coordinates of the "new" critical points found during each cycle.

3.3 Simulations Summary

The list of stationary and time dependent simulations is reported in Tale 3.4. The stationary simulation have been carried out exclusively for the 4 mm vessel and represent the benchmark for all the other computations. The time dependent simulation were carried out with different geometries (coronary artery and left femoral artery), rheological model (Newtonian and Carreau-Yasuda), and velocity inlet profiles (average and maximum velocity values of the coronary artery velocity profile, coronary artery and left femoral artery pulsatile velocity profiles).

Stationary Simulations

Diameter (mm)	Rheological model	Inlet Velocity (m/s)	Maximum Reynolds Number	N° of Cycles
4	Newtonian	0.22	267	30
4	Newtonian	0.37	448	10

Time Dependent Simulations

Diameter (mm)	Rheological model	Inlet Velocity (m/s)	Time Step	N° of Cycles
4	Newtonian	Pulsatile velocity (CA)	$0.02 \cdot T$	18
4	Carreau-Yasuda	Pulsatile velocity (CA)	$0.02 \cdot T$	20
6	Newtonian	Pulsatile velocity (LFA)	$0.01 \cdot T$	18

Table 3.4: Brief overview of the simulations discussed in the thesis

Chapter 4

Stationary Results

This chapter illustrates the results concerning the stationary simulations, considering the two steady velocity inlet conditions discussed in chapter 3. In particular, we will:
report on the simulated neointimal growth; compare the main flow properties obtained by imposing either average or high velocity inlet conditions; describe the evolution of the various parameters and their response to lumen narrowing.

4.1 Wall Shear stress and Neointimal thickness

The stent presence produces zones of higher and lower wall shear stress compared with the normal physiological values. We first describe the progression of endothelial growth and then discuss the shear stress distributions that led to it.

4.1.1 Neointimal thickness

The imposed inlet condition significantly influences the various parameters, in particular the growth progression and the final lumen geometry.
As shown in Figure 4.1, the endothelial tissue begins to accumulate near the stent struts and slowly progresses towards the center of the cells. The viscosity distribution nearby the external vessel walls, simulating neointimal hyperplasia, qualitatively evolves in the same manner for both velocities. In both cases, the endothelial layer fully covers the stented region after the same number iterations. However, a deeper analysis on transversal slices reveals key differences between the two simulations.
As discussed in numerous studies, stent implantation induces a lower wall shear stress region at the stent outlet as compared to the inlet. Moreover, the size of this region is proportional to the mean fluid flow velocity. This difference becomes more pronounced after each cycle, as showed in the average velocity simulations (Fig.

4.1d,4.2b)

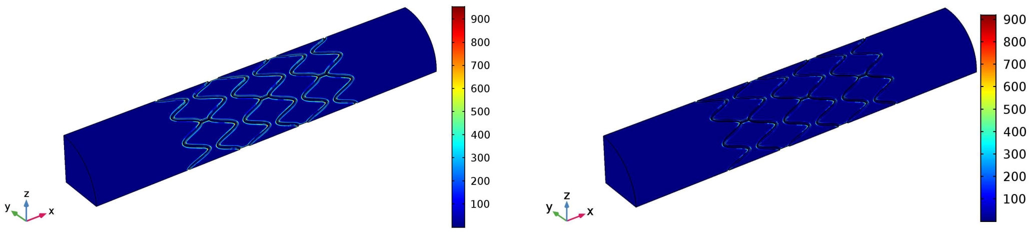

(a)

First Endothelial profile

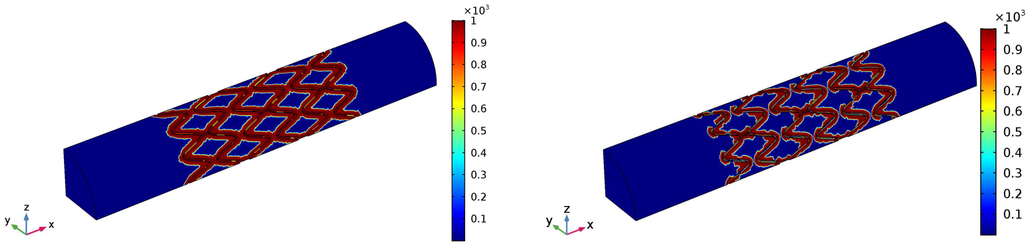

(b) Third Endothelial profile

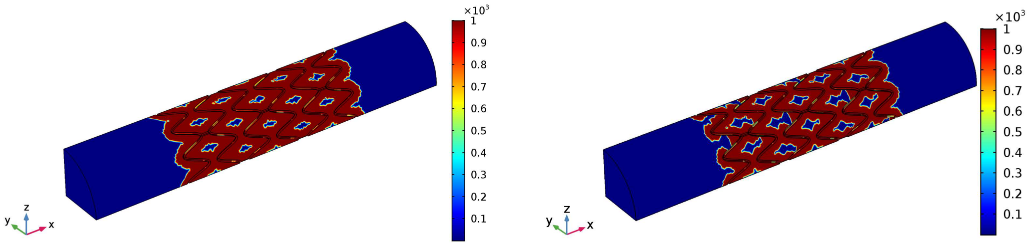

(c) Fifth Endothelial profile

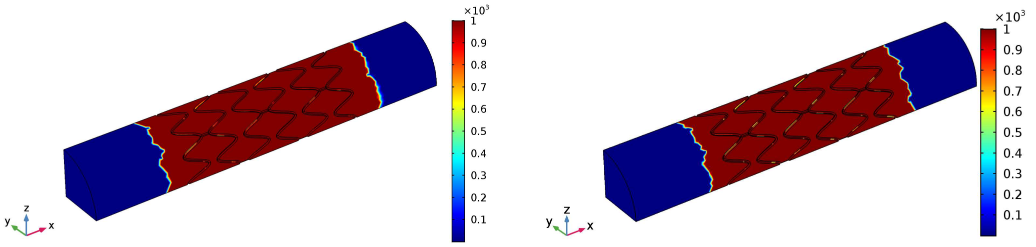

(d) Tenth Endothelial profile

Figure 4.1: Dynamical viscosity profiles (Pa·s), representing neointimal hyperplasia on the vessel wall, obtained using equation (3.4). Left panels: average velocity simulations. Right panels: high velocity simulations.

The progression of the lumen narrowing is very different when considering average and high inlet velocities. As expected, lower velocity is linked to lower wall shear stress and consequent quicker restenosis process.
We selected a single cross-section slice to highlight the differences in neointimal thickness evolution for the two different velocity input conditions (Fig. 4.2)

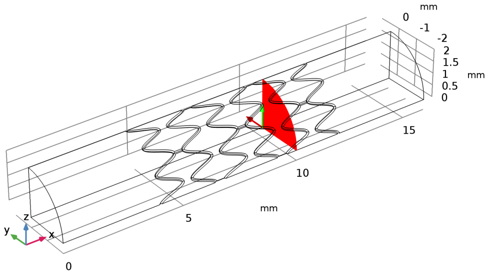

(a) Selected vessel slice, x=10 mm

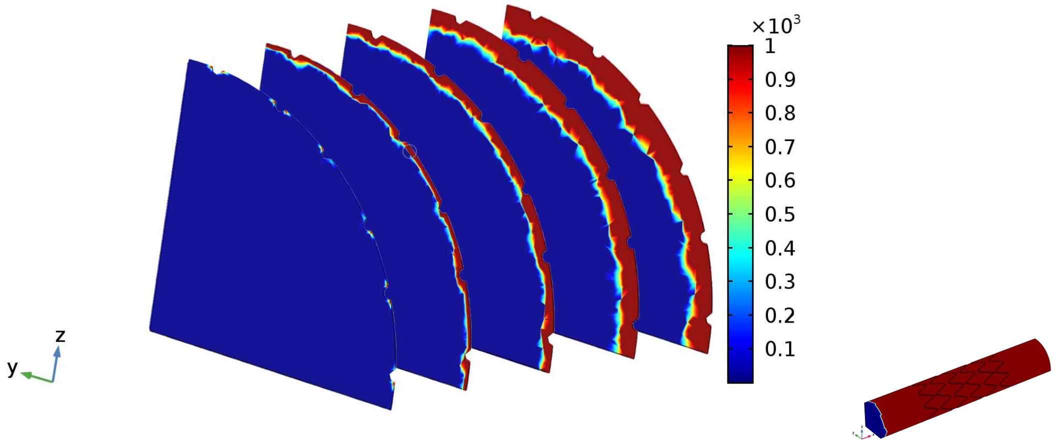

(b) Average velocity results, from left to right we represented cycle 1,5,10,20,30.

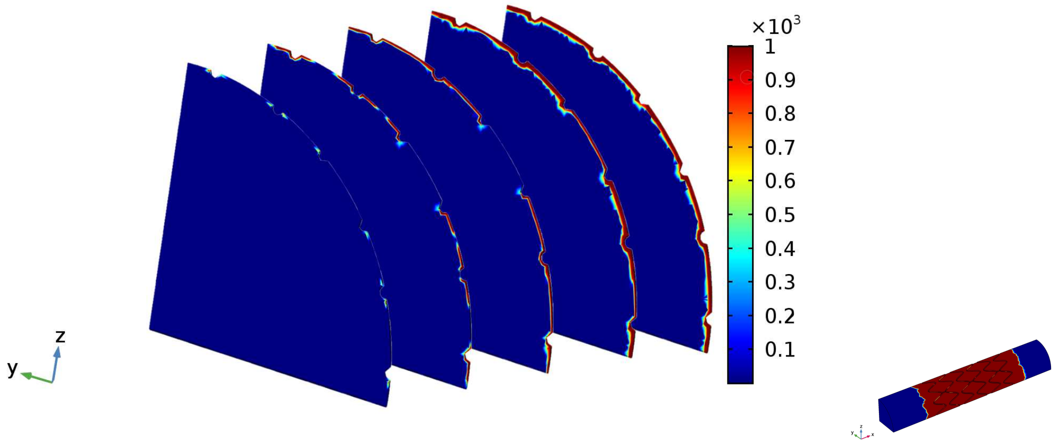

(c) High velocity results, from left to right we represented cycle 1,3,5,7,10.

Figure 4.2: Neointimal thickness progression, observed in a selected slice, displayed through the dynamical viscosity distributions (Pa · s)

The simulations conducted with a reference velocity of 0.37 m/s revealed very little endothelial growth. The progression seems to reach a plateau after the tenth cycle, with a neointimal thickness that stabilizes around 0.027 mm. The results for the average flow velocity input display a prolonged neointimal growth, which continues even after thirty cycles. As shown in Figure 4.3 the slope of the neointimal thickness growth curve gradually decreases with each iteration, reaching equilibrium plateau of about 0.15 mm. The simulated tissue growth is distributed homogeneously along the vessel wall. Excluding the initial cycles, no protrusion corresponding to the stent strut presence is observed in the transversal section.

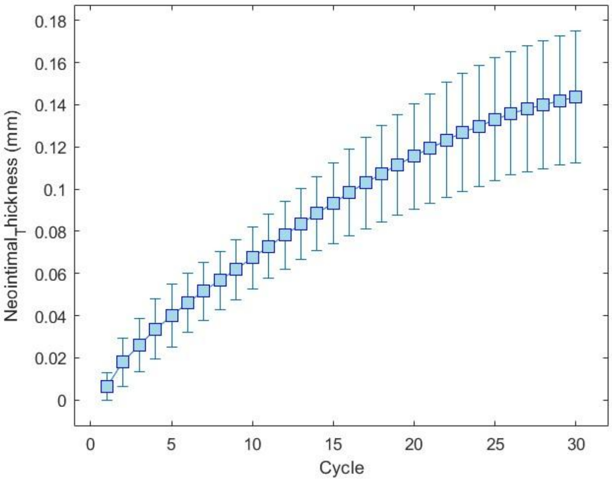

(a) Average velocity case.

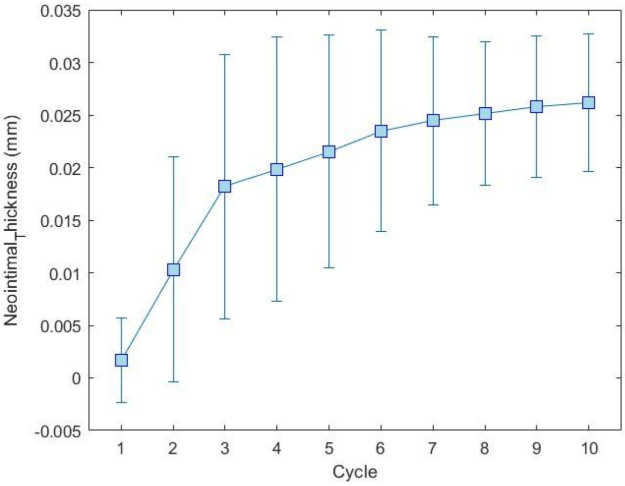

(b) High velocity case.

Figure 4.3: Neointimal thickness (mm) progression during each cycle.

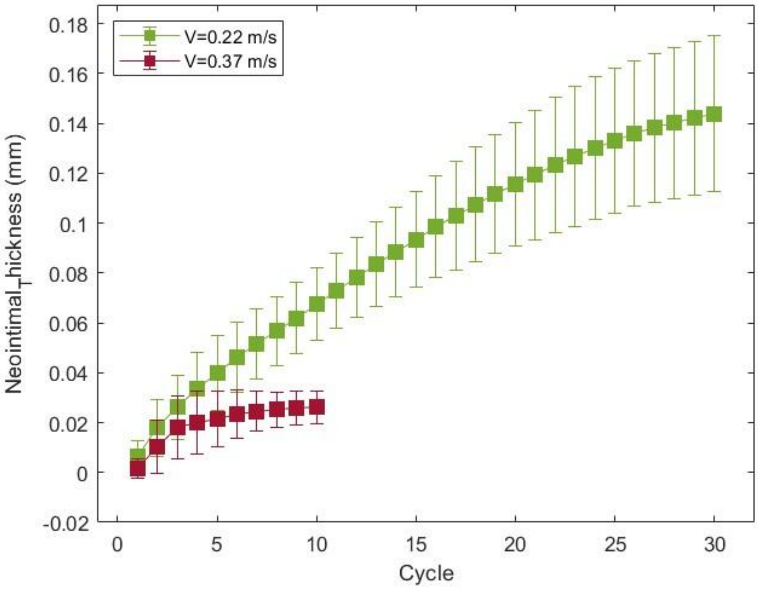

Figure 4.4: Neointimal thickness (mm) progression confront for both inlet velocities.

4.1.2 Wall shear stress

In chapter 2 we already discussed the importance of wall shear stress. Indeed numerous studies found a strong correlation between low stresses and endothelial growth. Figure 4.5, shows the initial WSS distribution on the vessel walls. We can appreciate the difference in magnitude in the smooth wall sections, with values around 0.7 Pa for the average velocity and almost doubled for the high velocity. However, in both cases a zone with values of the shear stress below the threshold of 0.5 Pa forms around the stent struts. These critical zones correspond to the regions where we observed the onset of the neointimal growth in Figure 4.1.

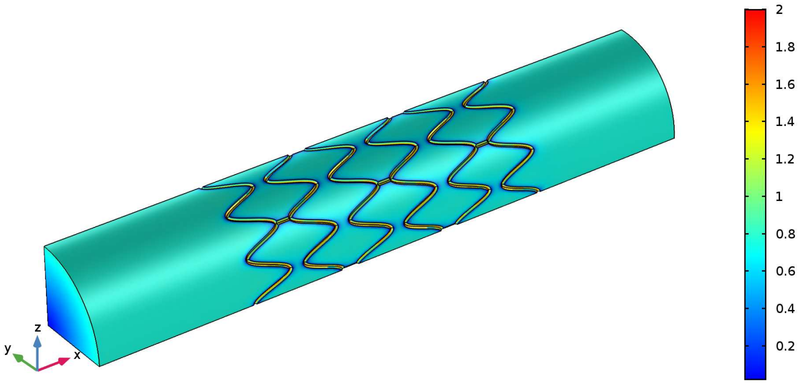

(a) Average Velocity

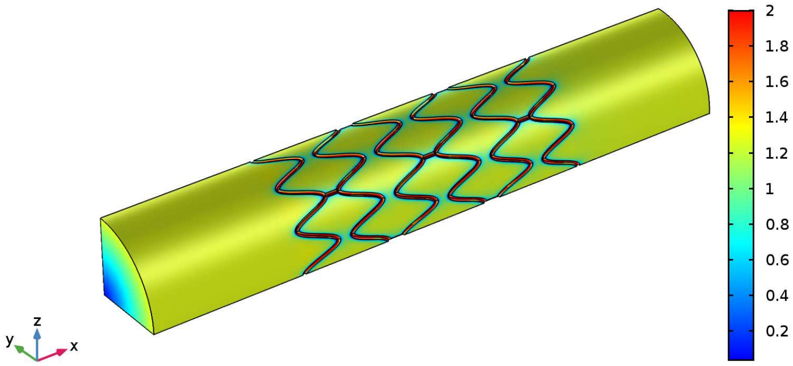

(b) High Velocity

Figure 4.5: Wall shear stress (Pa) first distribution, for both inlet velocities.

The inlet condition influence not only the wall shear stress magnitude, but also the overall volume of the critical zones produced in the simulations. The neointimal thickness registered after the first iteration in the simulations with the average velocity is almost fourfold that obtained in the high velocity case (Fig. 4.6).

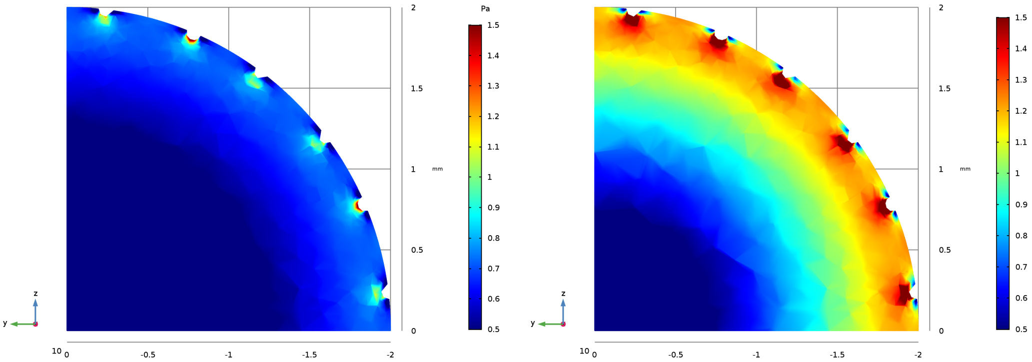

(a) First shear stress distribution

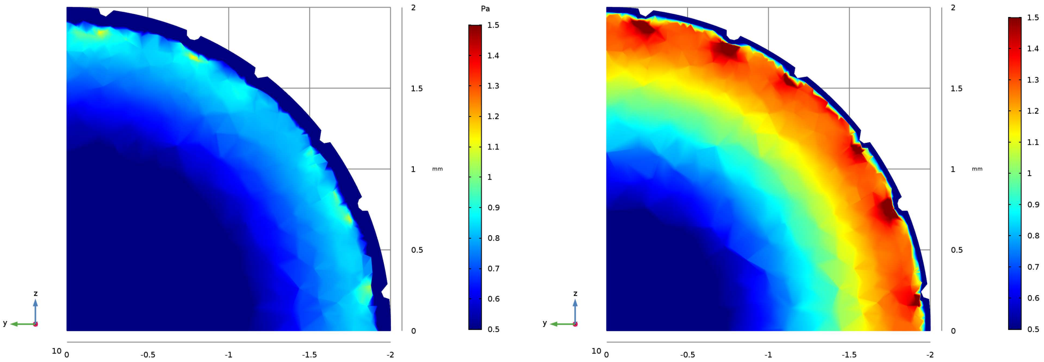

(b) Tenth shear stress distribution

Figure 4.6: Shear stress distribution in a transversal slice, for the simulation carried out with the average velocity inlet condition on the left, and the high velocity inlet condition on the right. The selected slice is the same as Fig. 4.2

The "equilibrium" configuration attained by the shear stress distribution for average and high velocity inlet simulations are shown in Figure 4.6b and 4.7. We can observe, especially in the average velocity simulation , how the shear stress near the neointimal tissue increases proportionally to the neointimal thickness increments. In the final configurations a circular area of high wall shear stress forms, which stops the neointimal growth progression.

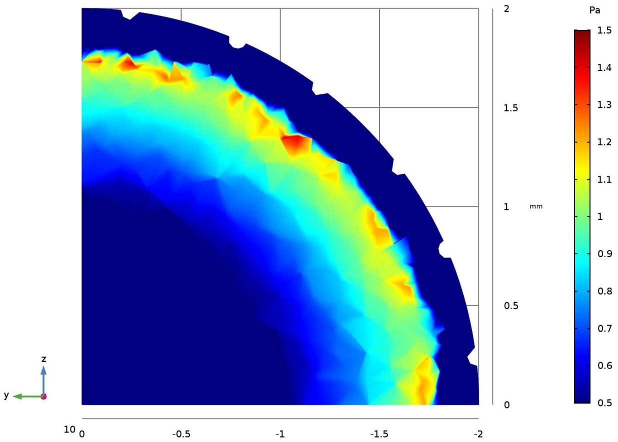

Figure 4.7: Shear stress distribution in a transversal slice, observed after the thirtieth cycle, for the simulation carried out with the average velocity inlet condition. The selected slice is the same as Fig. 4.2

4.2 Velocity and Streamlines

The stent presence alone affects parameters like velocity profiles and flow streamlines in the near wall zones. The simulated growth of the neointimal hyperplasia produces stronger changes in the various parameters.

4.2.1 Velocity

We are interested in how the initial (undisturbed) parabolic velocity profiles modify owing to the lumen narrowing. The difference between final and initial velocity magnitudes for both inlet velocity conditions are shown in Fig. 4.8. It clearly appears that the presence of the endothelial tissue significantly alters the flow in the near wall zone, while in the central region of the vessel only a slight increase in overall velocity occurs. As expected, more pronounced alterations are observed in this region as the restenosis progresses.

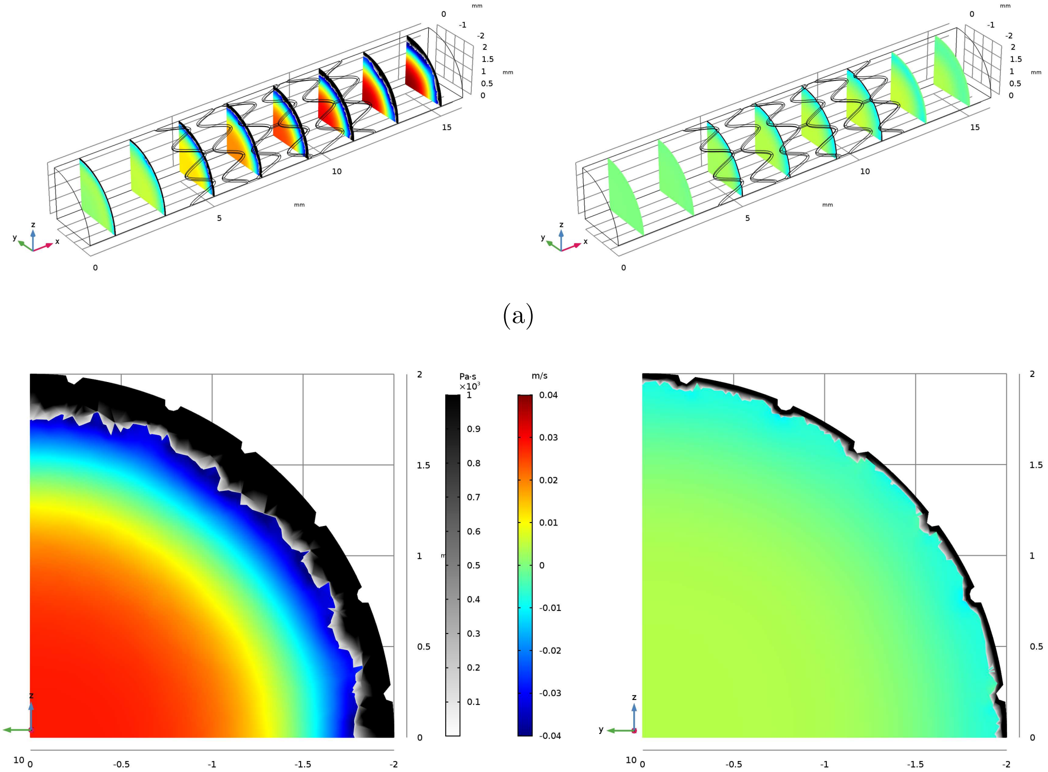

(a)

(b)

Figure 4.8: Difference in velocity magnitude (m/s) between the final and initial simulations. (a) Difference in eight slices. (b) Focus on the slice at x=10 mm. Endothelial growth represented through the dynamical viscosity.

4.2.2 Streamlines

To gain a better understanding of the formation of recirculation zones and the fluid elements movements, we analyze the spatial distribution of velocity streamlines. The streamlines are a family of curves that are always tangent to the instantaneous velocity vector field, $\vec{u}$.

As already reported in past studies, the presence of the stent not only deviates the streamlines, but also causes the formation of recirculation zones around the stent strut. The size of the vortices is proportional to the inlet velocity, but the qualitative behavior of the streamlines and their evolution strongly correlates with the registered neointimal thickness. Figure 4.9 shows the streamlines progression for the average velocity simulation, while the plots corresponding to the high velocity simulations can be found in Appendix A. Figure 4.9 indicates that the disturbances in the streamlines diminish with the endothelial growth.

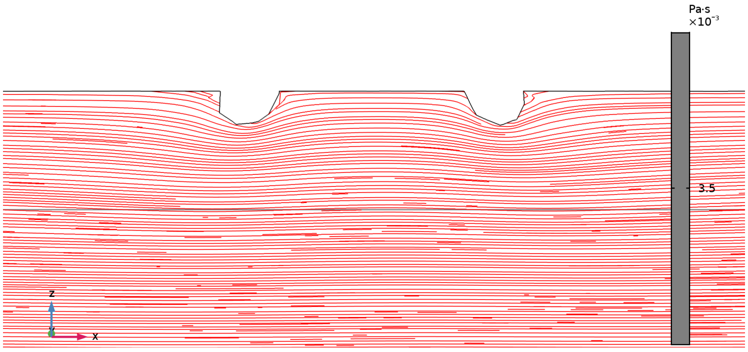

(a) First Cycle

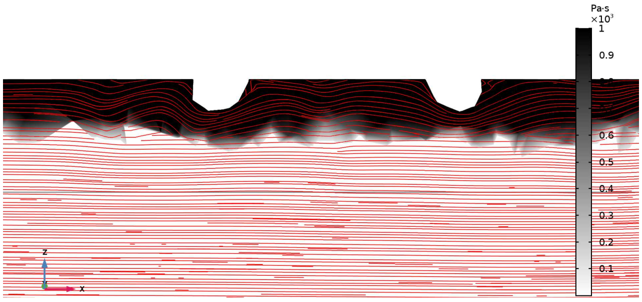

(b) Tenth Cycle

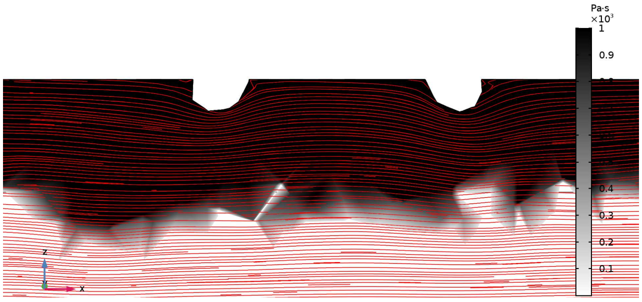

(c) Thirtieth Cycle

Figure 4.9: Longitudinal streamlines plot, average velocity simulations. Endothelial growth represented through the dynamical viscosity.

Transversal sections

The streamlines plots on transversal sections provide valuable information into the secondary currents forming near the vessel walls. The evolution of the streamlines reported in Figure 4.10 highlights the presence of concentric patterns around the stent struts, which, as observed for the longitudinal streamlines shown in Figure 4.9, diminish with the progression of restenosis. The streamline distribution reflects on the vorticity, as discussed in the next section.

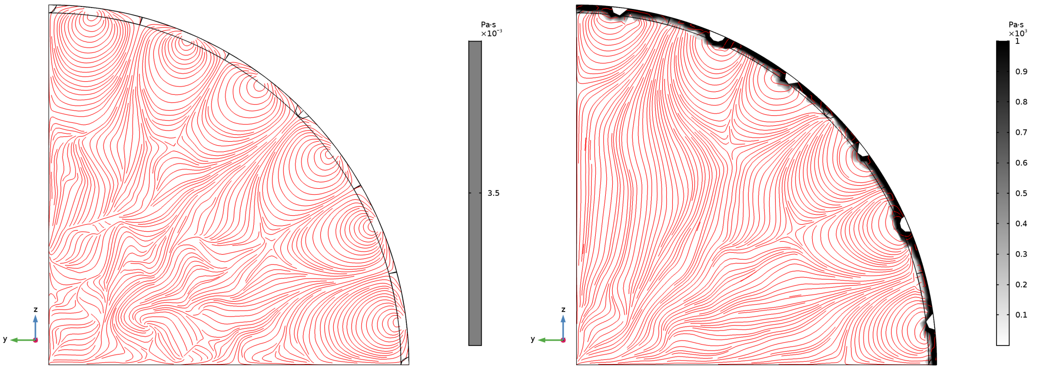

(a) First Cycle (b) Fifth Cycle

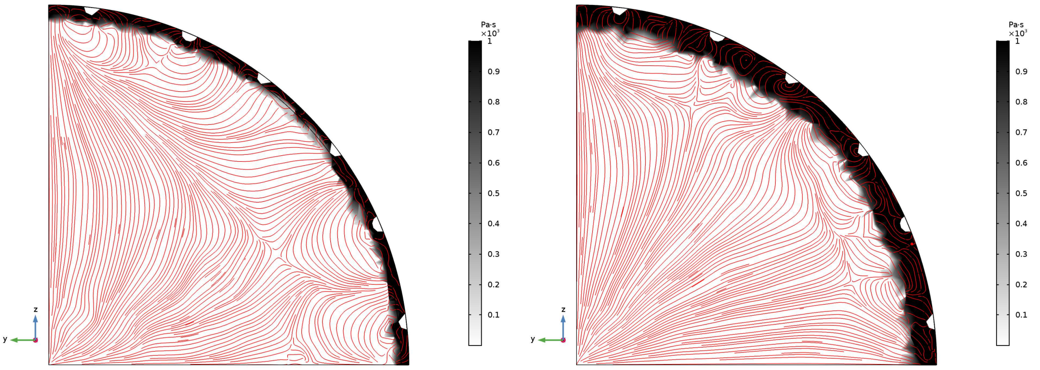

(c) Tenth Cycle (d) Twentieth Cycle

(e) Thirtieth Cycle

Figure 4.10: Transversal streamline plots, average velocity simulations. Endothelial growth represented through the dynamical viscosity.

4.3 Vorticity

The vorticity is defined as the curl of the velocity vector, i.e. $\vec{\omega} = \nabla x \vec{u}$, and it is a key parameter to understand displacements of fluid elements. Figure 4.11 and Figure 4.12 show the normal component ω_x of the vorticity vector on transversal slices of the fluid domain. The plots reveal the presence of clockwise and anti-clockwise rotation zones near the stent struts. Their positioning corresponds to the concentric patterns found in Figure 4.10 , and their magnitudes attenuate in a similar way.

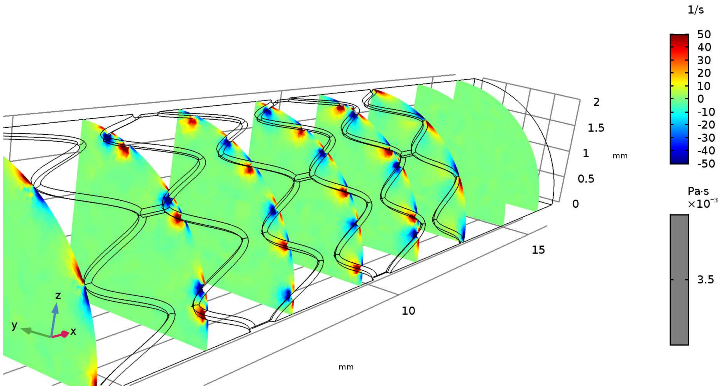

(a) First Cycle

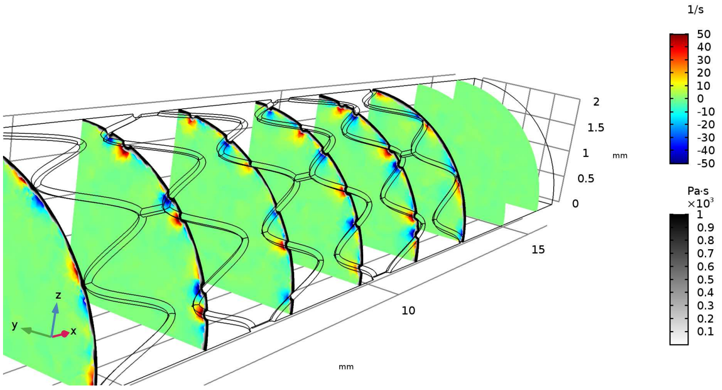

(b) Tenth Cycle

Figure 4.11: ω_x (1/s) vorticity component on transversal slices, high velocity simulations. Endothelial growth represented through the dynamical viscosity.

The vorticity attenuation as the simulation proceeds is even more appreciable in the results obtained by imposing the average velocity condition at the inlet. Figure 4.12c, highlights the presence of vorticity patterns in the distal part of the domain. These disturbances are related to the growth of the neointimal tissue..

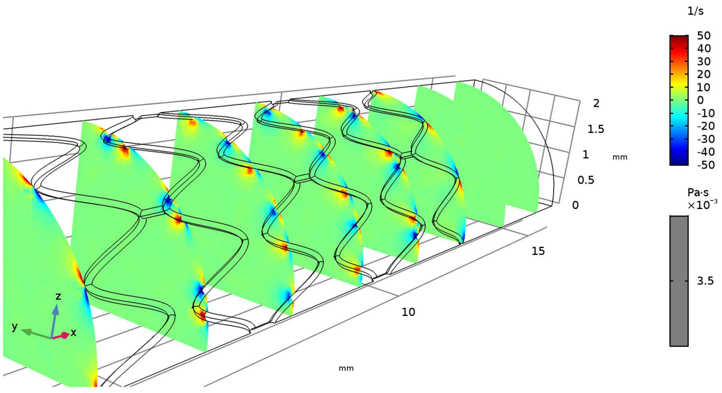

(a) First cycle

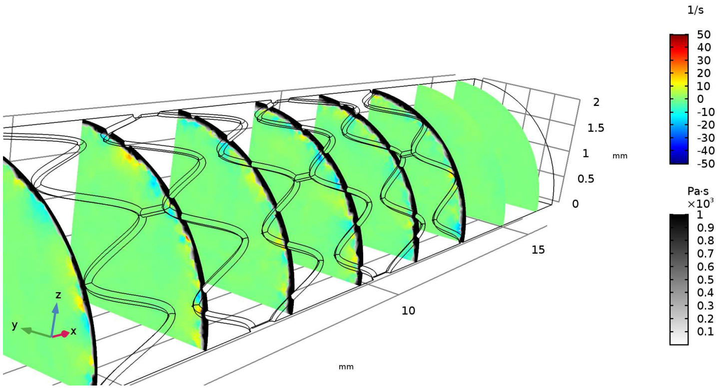

(b) Tenth cycle

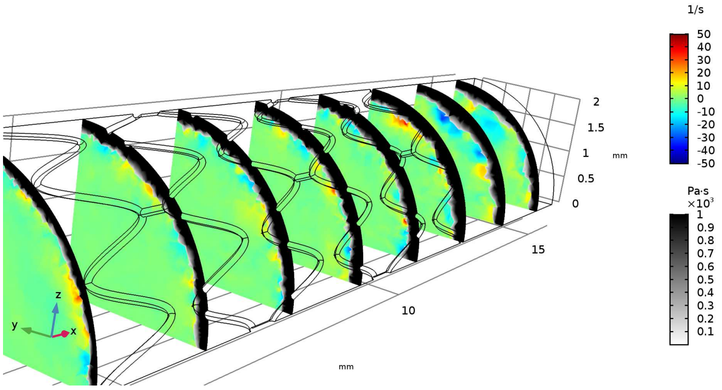

(c) Thirtieth cycle

Figure 4.12: ω_x (1/s) vorticity component on transversal slices, average velocity simulations. Endothelial growth represented through the dynamical viscosity.

4.4 Pressure

To conclude, Figure 4.13 shows the pressure distribution along the vessel length for both inlet conditions. The pressure, as expected, decrease linearly. In both cases, there is a remarkable increase in pressure due to the lumen narrowing while keeping the inlet velocity profile fixed. The differences between the initial pressure distributions attenuate in the final configuration. The endothelial growth causes disturbances and irregularities in the pressure distribution along the vessel boundaries.

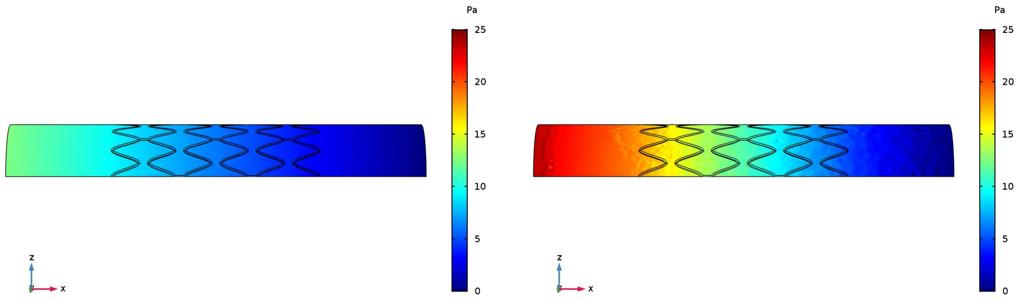

(a) Average velocity results.

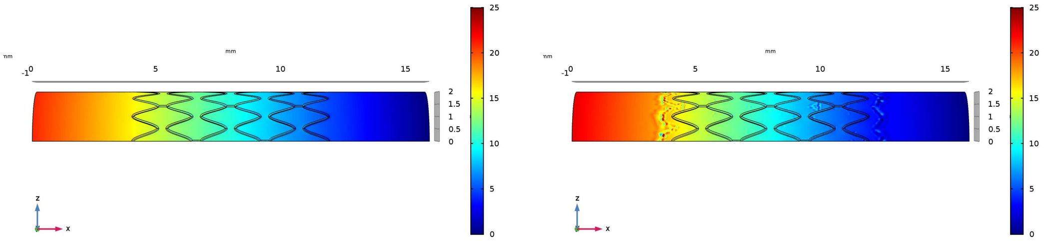

(b) High velocity results

Figure 4.13: Pressure along the external surface. On the left initial distribution, on the right final distribution.

Chapter 5

Time Dependent Results

The time dependent simulations are able to produce a more realistic evolution of in stent restenosis progression. In this chapter we present the CFD results obtained for a coronary artery and a left femoral artery.

5.1 Coronary Artery

Let us first consider the shear stresses computed at different cycles, and the correspondent neointimal thickness. In particular, we focus on five different time instants, corresponding to local minima and maxima of the cardiac cycle (Fig. 5.1). Then we display the respective time averaged wall shear stress and the endothelial growth progression.

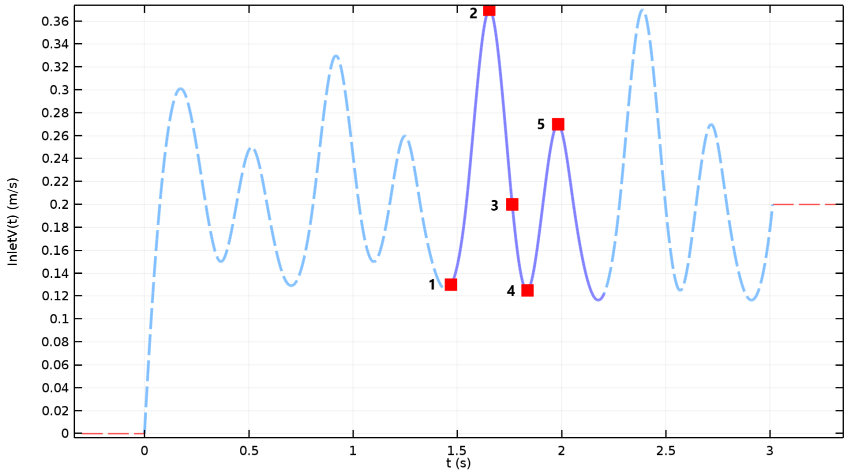

Figure 5.1: Coronary artery inlet velocity profile and selected instants used to evaluate pulsatile effects.

5.1.1 Wall shear stress

Figures 5.2-5.7 show the evolution of instantaneous shear stresses and the time averaged wall shear stress used to evaluate endothelial growth, for three different cycles, at the instants defined in Fig. 5.1.

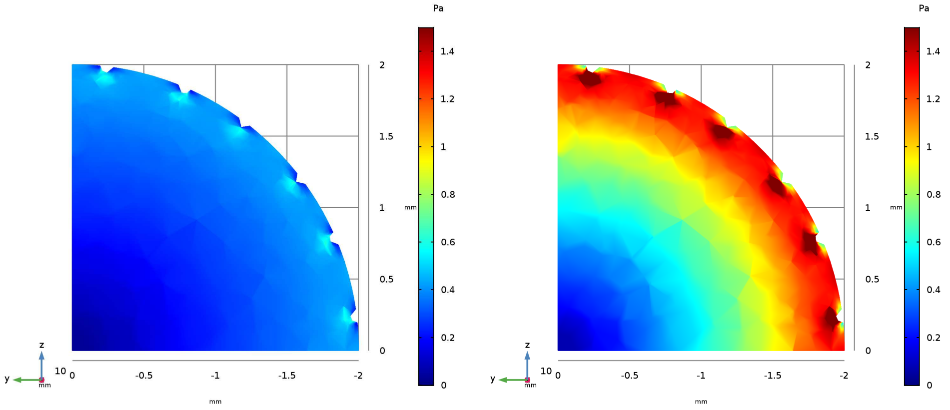

(a) Instant 1

(b) Instant 2

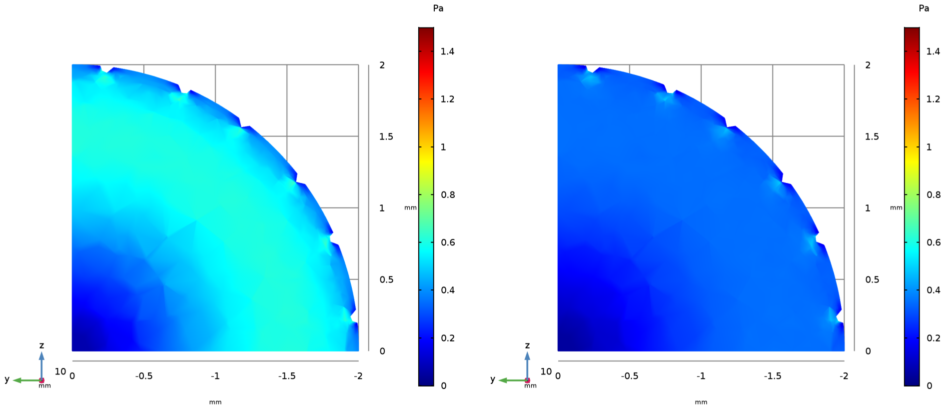

(c) Instant 3

(d) Instant 4

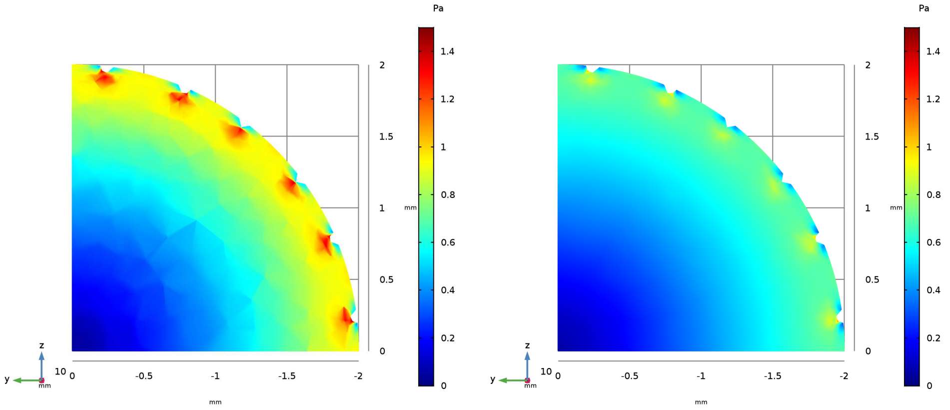

(e) Instant 5

(f) Time averaged shear stress

Figure 5.2: Shear stresses evolution in the five selected instants (a-e) and the time averaged shear stress (f), computed at the end of the first cycle.

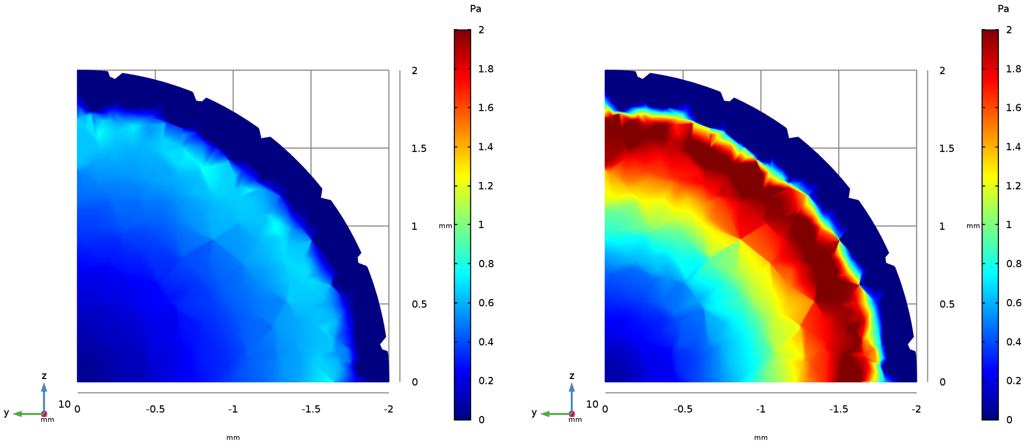

(a) Instant 1 (b) Instant 2

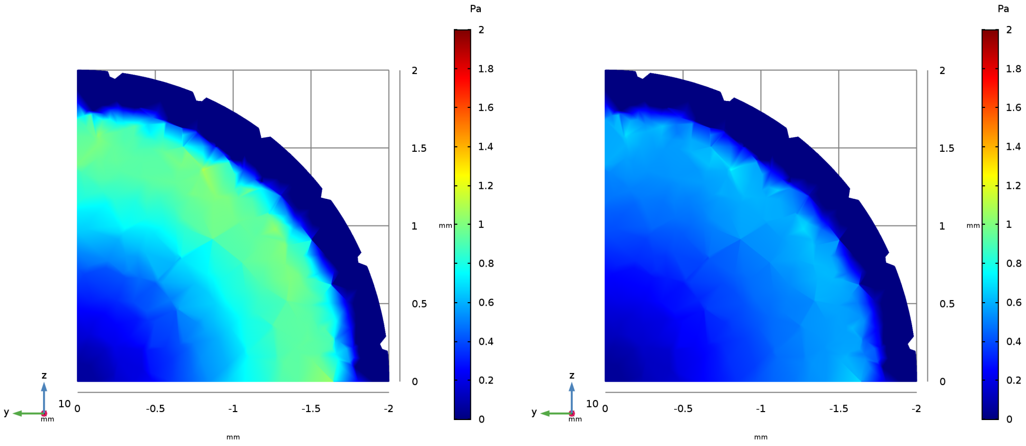

(c) Instant 3 (d) Instant 4

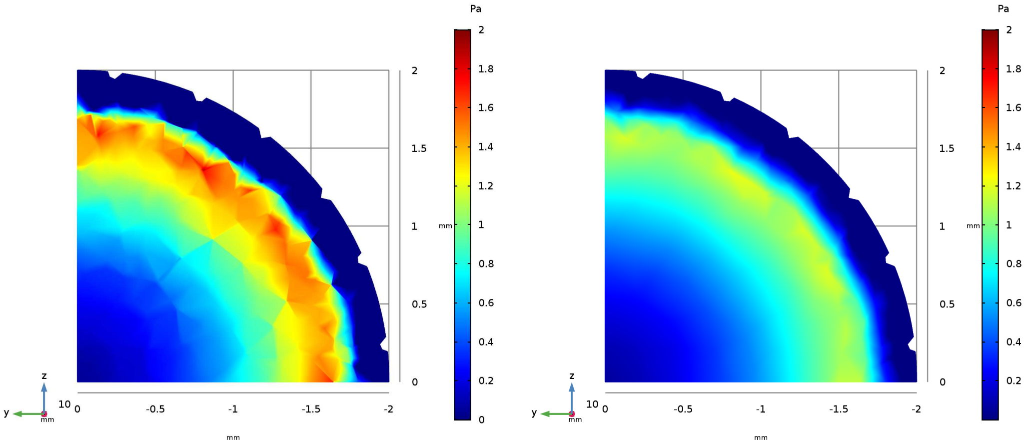

(e) Instant 5 (f) Time averaged shear stress

Figure 5.3: Shear stresses evolution in the five selected instants (a-e) and the time averaged shear stress (f), computed at the end of the fifth cycle.

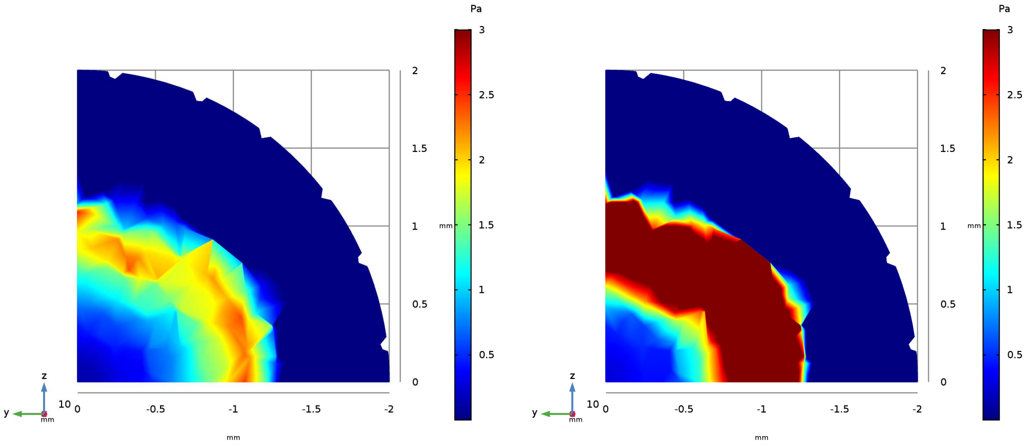

(a) Instant 1 (b) Instant 2

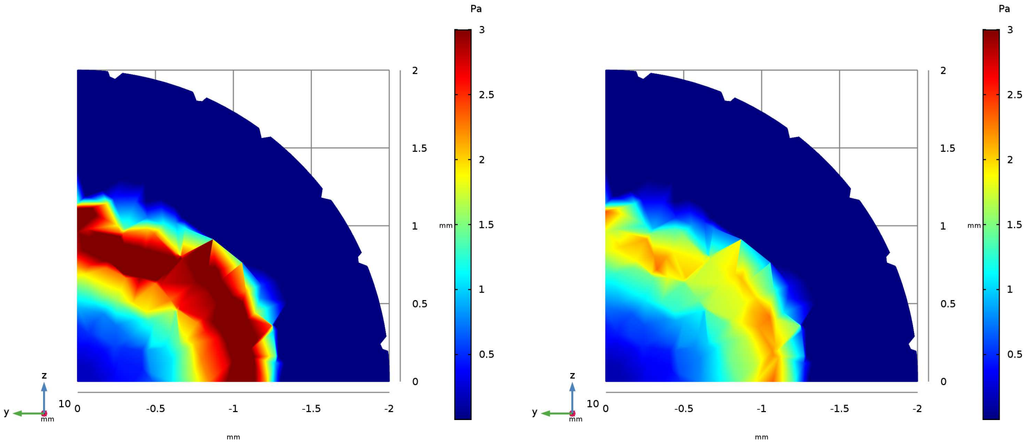

(c) Instant 3 (d) Instant 4

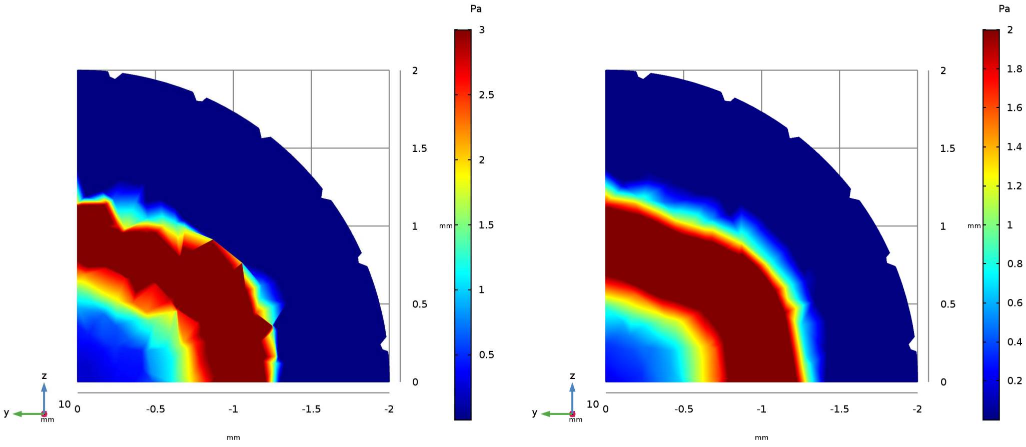

(e) Instant 5 (f) Time averaged shear stress

Figure 5.4: Shear Shear stresses evolution in the five selected instants (a-e) and the time averaged shear stress (f),computed at the end of the eighteenth, and last, cycle.

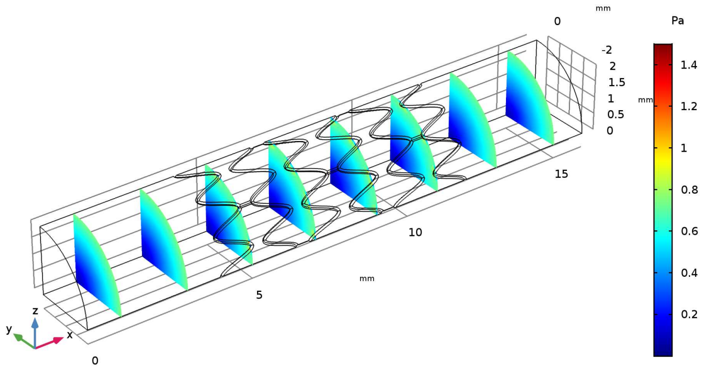

(a) First Cycle

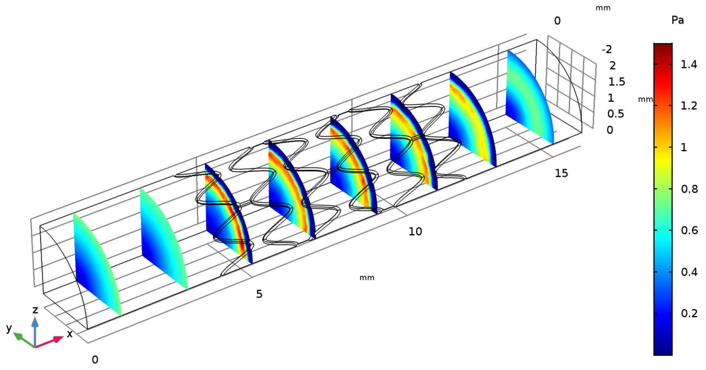

(b) Fifth Cycle

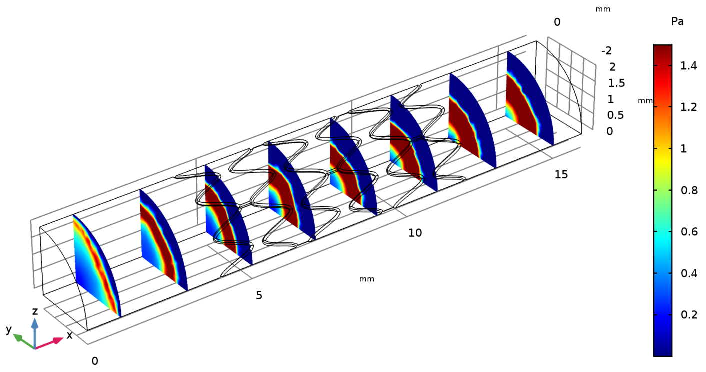

(c) Eighteenth Cycle

Figure 5.5: Time averaged wall shear stresses evaluated in eight transversal slices, computed at the end of three different cycles.

5.1.2 Neointimal thickness

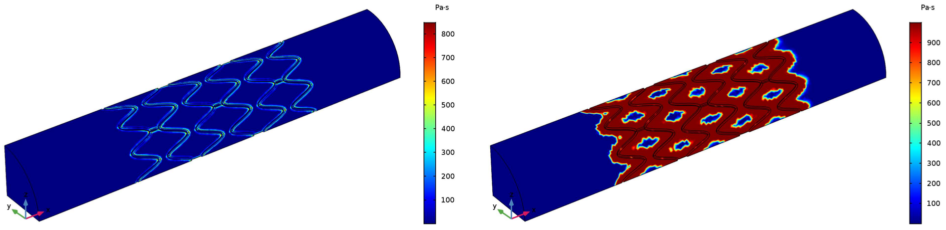

(a) First Cycle (b) Third Cycle

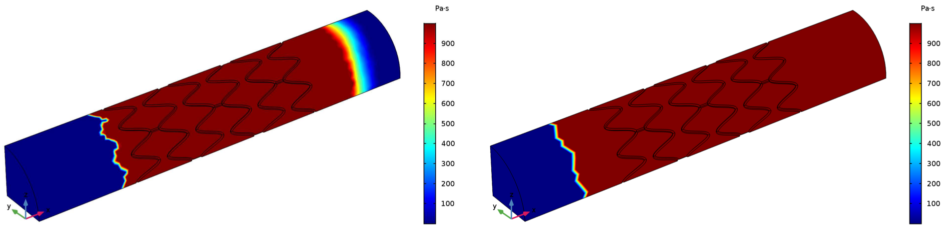

(c) Fifth Cycle (d) Tenth Cycle

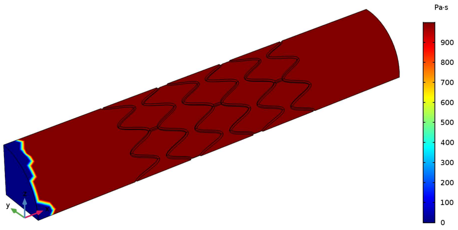

(e) Eighteenth Cycle

Figure 5.6: Dynamical viscosity profiles (Pa·s), mimicking neointimal hyperplasia growth on the vessel wall, obtained using equation (3.5).

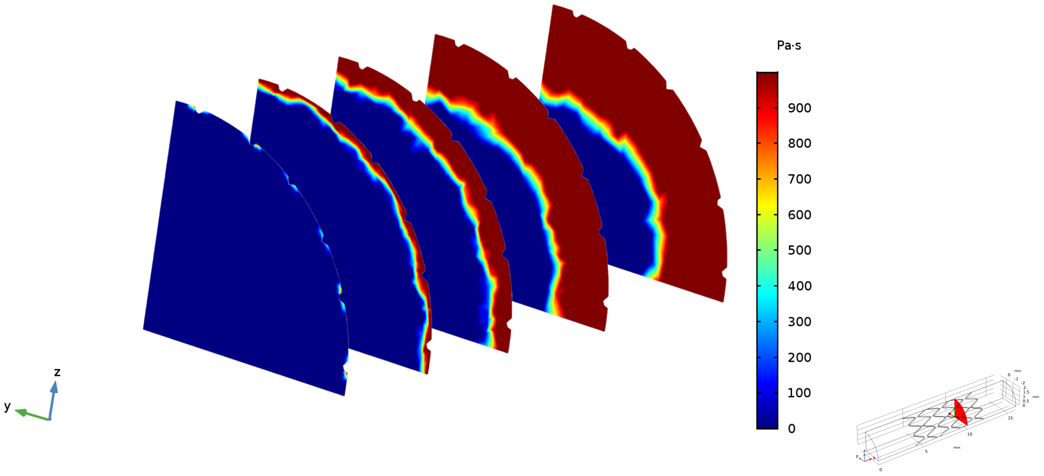

Figure 5.7: Neointimal thickness progression, in a singular slice, mimicked through the dynamical viscosity distributions, for the cycles 1,3,5,10,18 (from left to right).

Overall, the endothelial growth on the vessel walls is qualitatively similar to the stationary results presented in chapter 4. However, the downstream flow disturbances due to stent presence and endothelial growth are more evident, while the formation of a thin endothelial layer is observed even in the upstream region.
The neointimal thickness growth curve resembles, qualitatively, the multiscale simulations results discussed in chapter 2. The progression ceases after eighteen cycles, with an estimated neointimal thickness of 0.63 mm which corresponds to a vessel occlusion of approximately 50%.

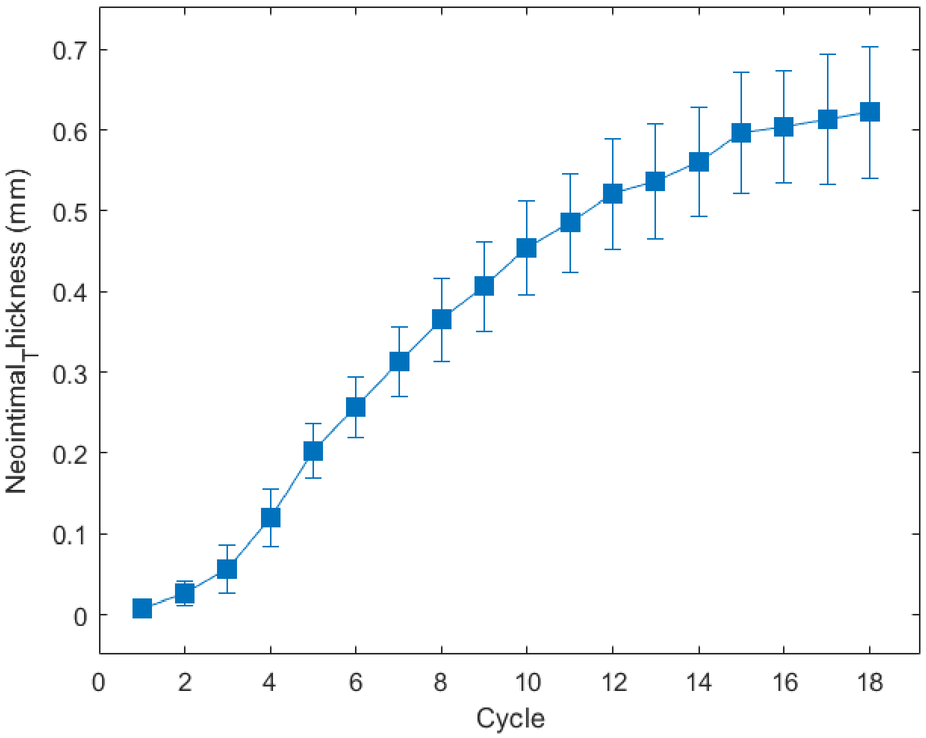

Figure 5.8: Evolution of the mean neointimal thickness (mm) for the coronary artery, resulting from the unsteady CFD simulations carried out assuming a Newtonian fluid model. The vertical lines correspond to the standard deviation.

To evaluate the mesh dependency of the numerical results, we performed a re-meshing after the eleventh cycle and computed the difference with respect to the previous results with the coarser mesh. The changes in the growth curves are relatively small and an identical neointimal thickness is eventually attained, as shown by the results reported in appendix A.

5.1.3 Carreau-Yasuda rheological model

The implementation of a non-Newtonian rheological model produced slightly different results. Adopting the Carreau-Yasuda fluid model led to a slower endothelial growth and a lower final neointimal thickness. Moreover, two extra iterations were needed to reach the equilibrium configuration. The final registered neoinitmal thickness is 0.6 mm.

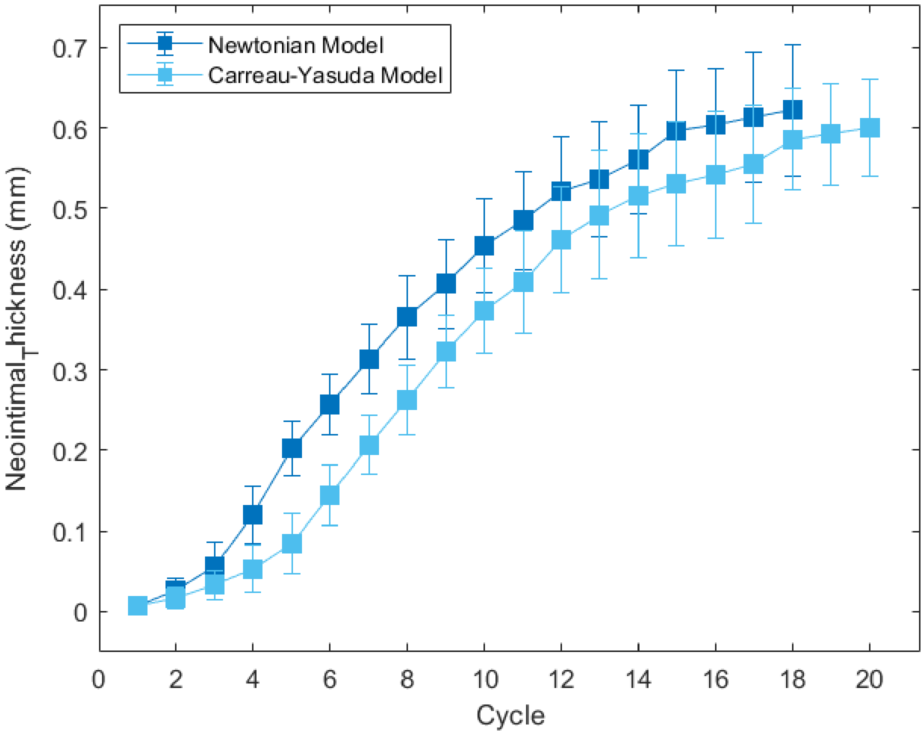

Figure 5.9: Evolution of the mean neointimal thickness (mm) for the coronary artery, resulting from the unsteady CFD simulations carried out assuming a Newtonian and non-Newtonian fluid model. The vertical lines correspond to the standard deviation.

5.2 Left Femoral Artery

Also for the left femoral artery simulations we monitored the flow characteristis and the endothelial growth for five local minima and maxima of the cardiac cycle.
In this particular case, the inlet velocity profile allow us to evaluate the oscillatory shear index and appreciate the difference in predicting critical region with respect to wall shear stress. We will conclude the analysis comparing the endothelial growth curves obtained for the coronary and femoral arteries.

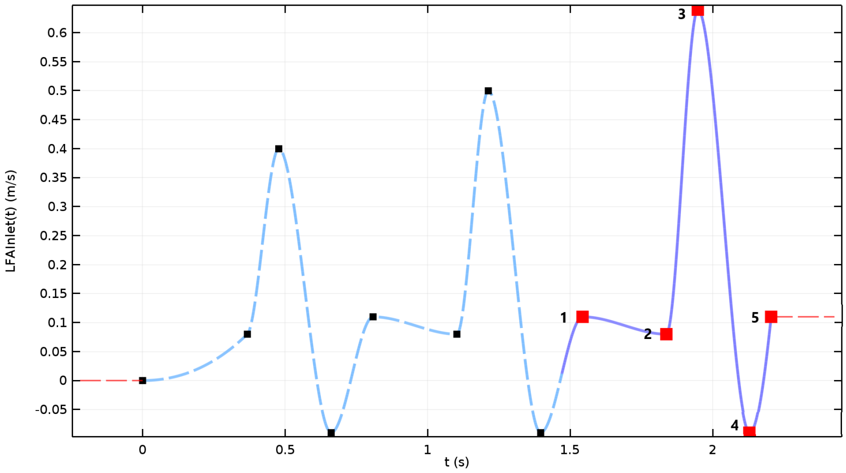

Figure 5.10: Left femoral artery inlet velocity profile and selected instants used to evaluate pulsatile effects.

5.2.1 Wall Shear Stress

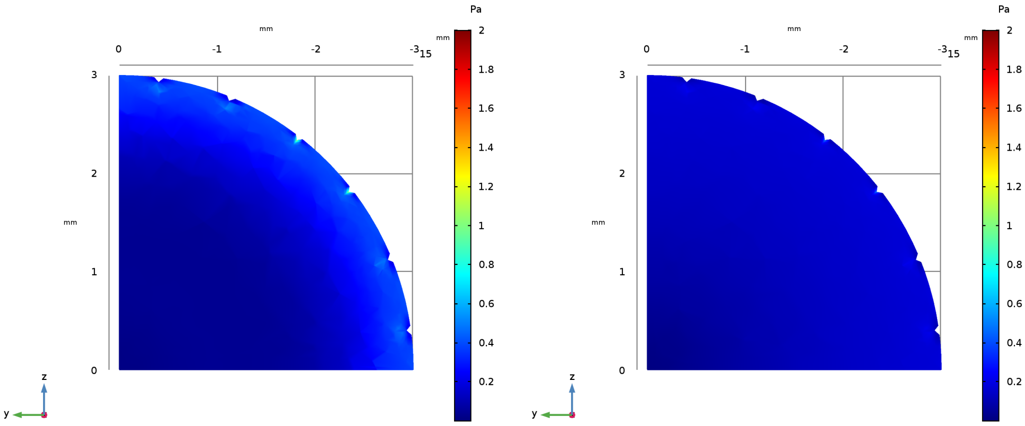

(a) Instant 1

(b) Instant 2

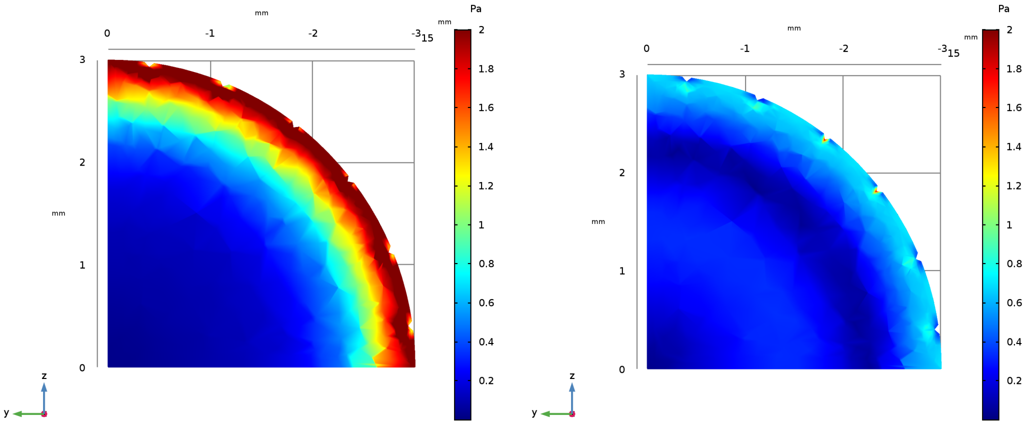

(c) Instant 3

(d) Instant 4

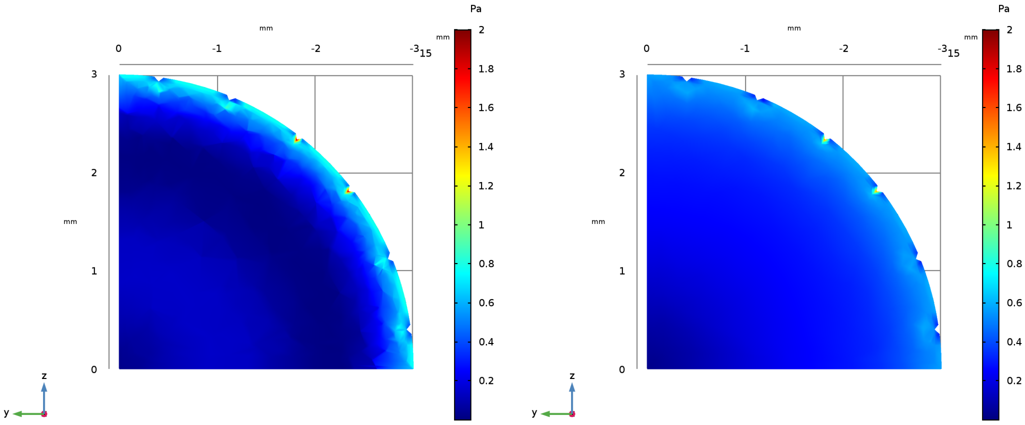

(e) Instant 5

(f) Time averaged shear stress

Figure 5.11: Shear stresses evolution in the five selected instants (a-e) and the time averaged shear stress (f), computed at the end of the first cycle.

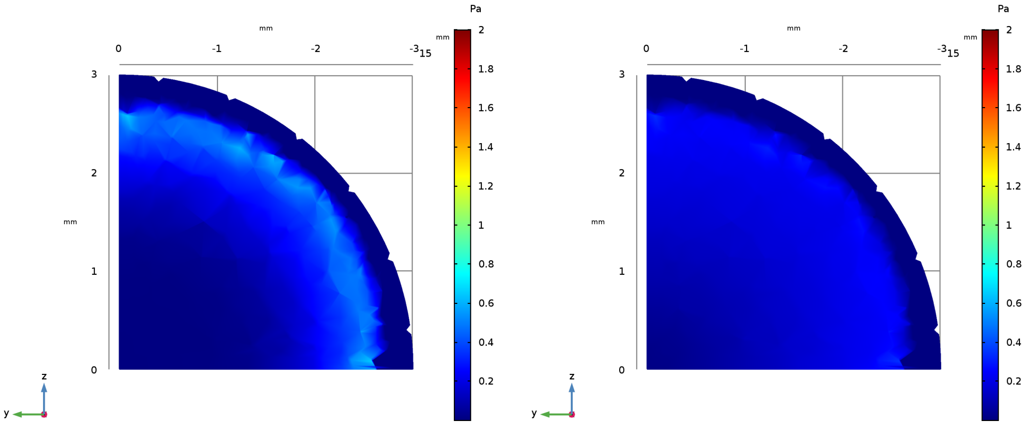

(a) Instant 1

(b) Instant 2

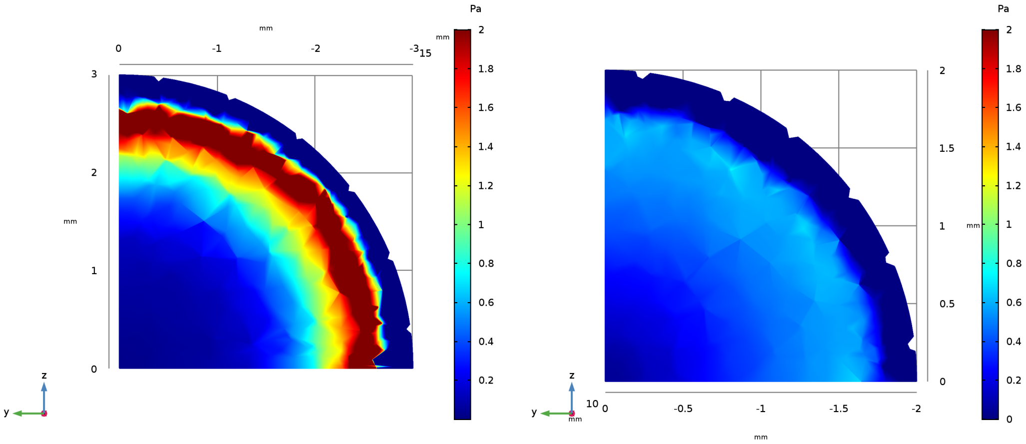

(c) Instant 3

(d) Instant 4

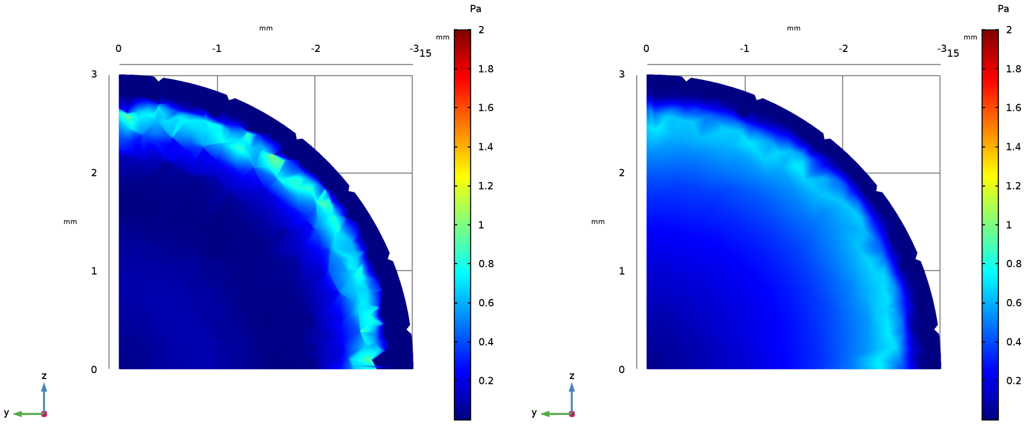

(e) Instant 5

(f) Time averaged shear stress

Figure 5.12: Shear stresses evolution in the five selected instants (a-e) and the time averaged shear stress (f), computed at the end of the fifth cycle.

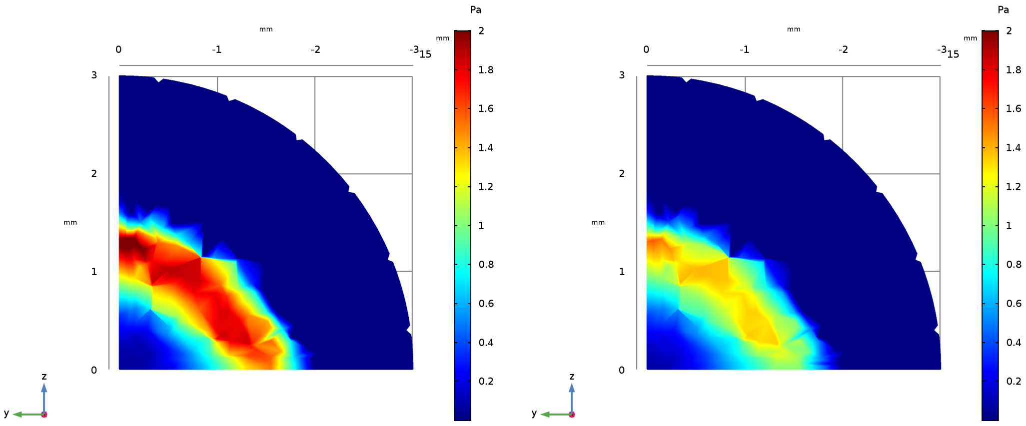

(a) Instant 1

(b) Instant 2

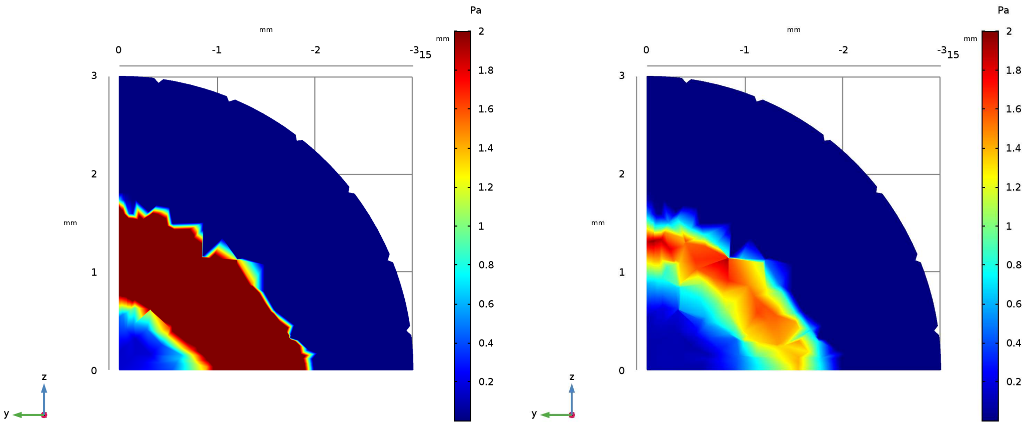

(c) Instant 3

(d) Instant 4

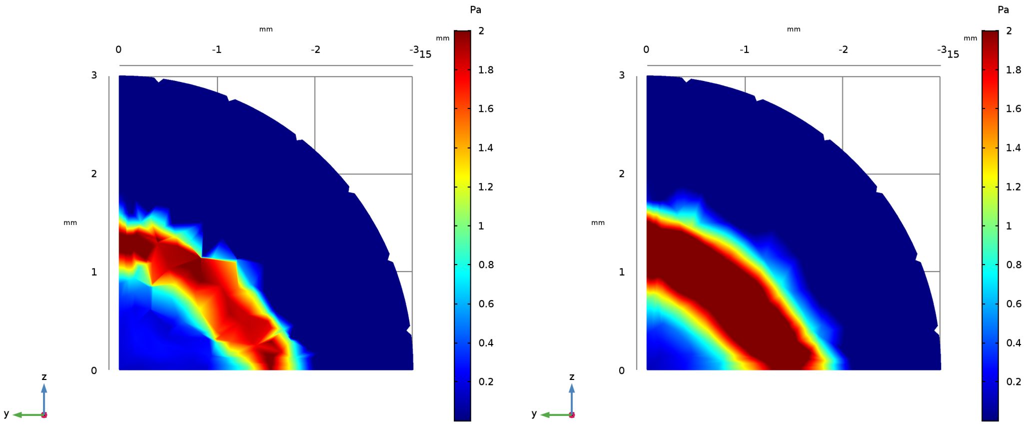

(e) Instant 5

(f) Time averaged shear stress

Figure 5.13: Shear stresses evolution in the five selected instants (a-e) and the time averaged shear stress (f), computed at the end of the eighteenth, and last, cycle.

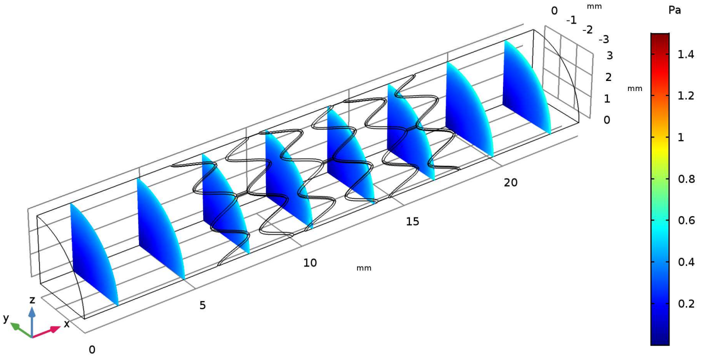

(a) First Cycle

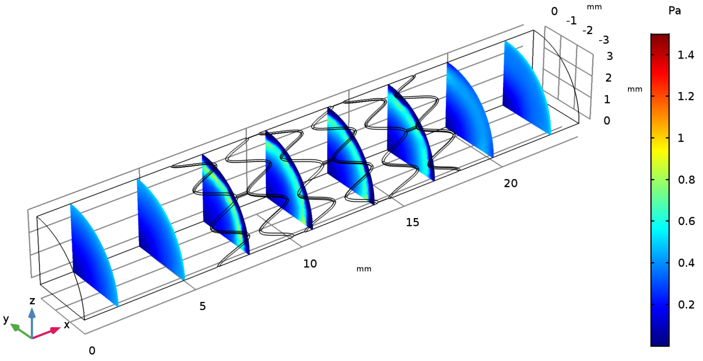

(b) Fifth Cycle

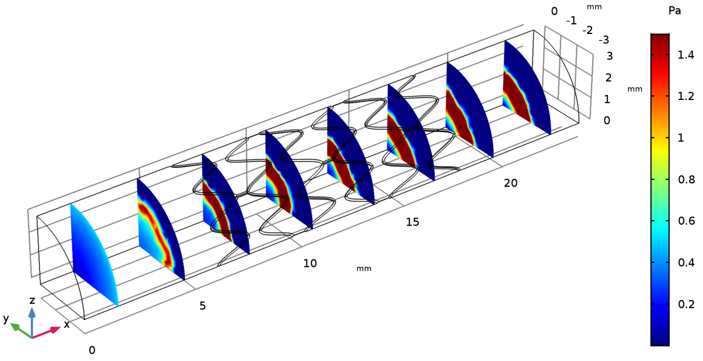

(c) Eighteenth Cycle Cycle

Figure 5.14: Time averaged wall shear stresses evaluated in eight transversal, computed at the end of three different cycles.

5.2.2 Neointimal thickness

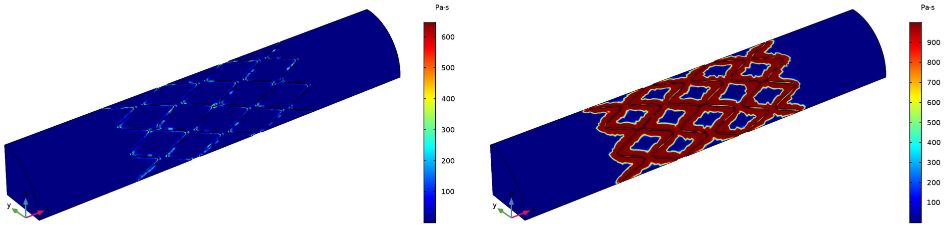

(a) First Cycle (b) Third Cycle

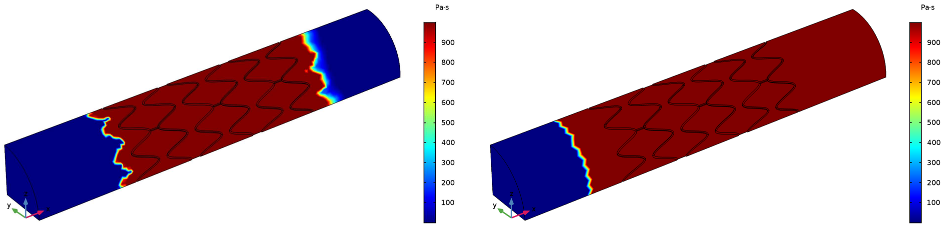

(c) Fifth Cycle (d) Tenth Cycle

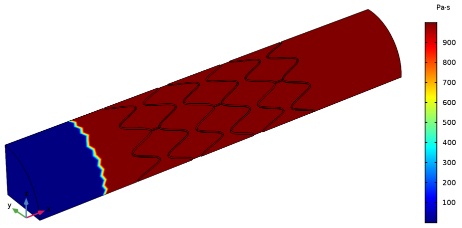

(e) Eighteent Cycle

Figure 5.15: Dynamical viscosity profiles (Pa·s), mimicking neointimal hyperplasia growth on the vessel wall, obtained using equation (3.5).

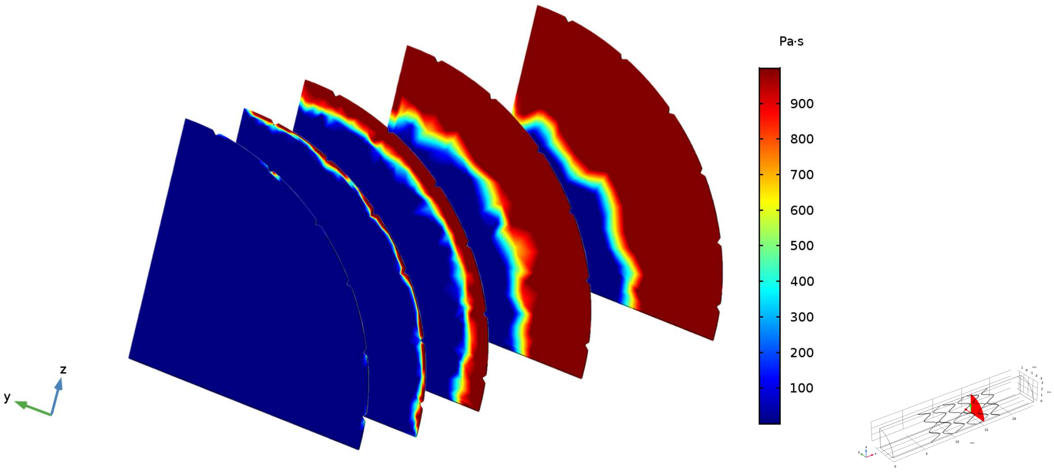

Figure 5.16: Neointimal thickness progression, in a singular slice, mimicked through the dynamical viscosity distributions,for the cycles 1,3,5,10,18 (from left to right).

Figure 5.11-5.16 show that the results of the left femoral artery simulations followed patterns similar to those computed for the coronary artery (Figures 5.2-5.7). The downstream stent region remains a critical zone, while the upstream region exhibits considerably less endothelial growth as compared to the coronary artery simulations (Fig. 5.15).
The growth curves for the two types of artery begin to diverge after five cycles. In the case of the left femoral artery, neointimal growth ceased when the neointimal thickness reached approximately 1.22 mm, corresponding to a vessel occlusion of 75%.

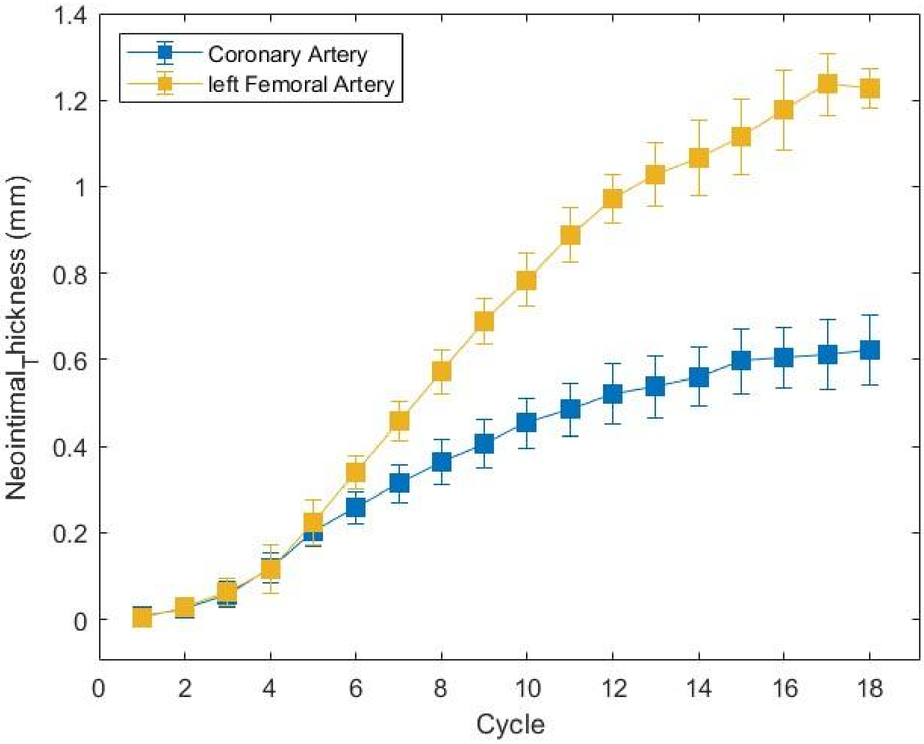

Figure 5.17: Evolution of the mean neointimal thickness (mm) for the coronary artery and left femoral artery, resulting from the unsteady CFD simulations carried out assuming a Newtonian fluid model. The vertical lines correspond to the standard deviation.

5.2.3 Oscillatory shear index

The oscillatory shear index (OSI) is a parameter used to express the ratio between backward and forward shear stresses. It can be employed to identify critical regions in the presence of partially reversed flow, as observed in the left femoral artery cardiac cycle, or in cases of disturbed flows within complex vessel geometries. As discussed in chapter 2.2, the critical threshold for the OSI index was set at 0.2 (Morlacchi 2011,Colombo 2021a). A region with values exceeding this threshold is characterized by highly oscillatory flow.

Figure 5.18 shows the spatial distribution of the OSI values at the end of the first and fifth cycles. It clearly emerges that the critical regions are primarily located in the distal part of the stent and on the stent struts.

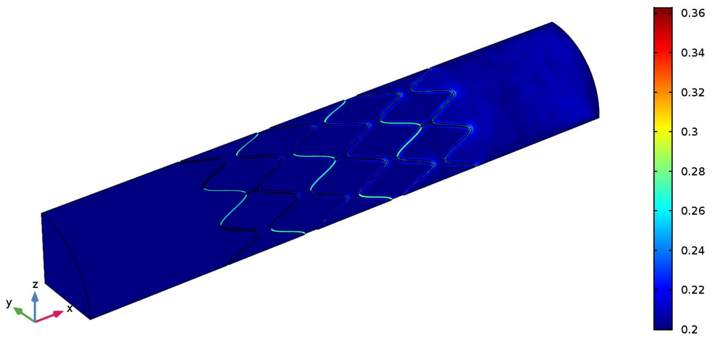

(a) First Cycle

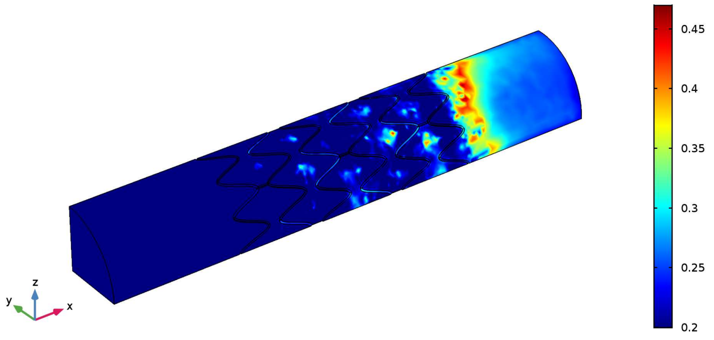

(b) Fifth Cycle

Figure 5.18: OSI index evaluated on the external surface of the left femoral artery vessel geometry.

The critical zones as identified by the OSI index are almost absent in the innermost zones of the left femoral artery after five cycles.

Finally, Figure 5.19 shows the difference between the near wall spatial distributions of the WSS and OSI indexes computed for left femoral artery. A positive or negative value of this difference individuates a critical region for either the WSS or the OSI index, while a zero values means the indexes provide the same information. Figure 5.19 indicates that the oscillatory shear index overestimates the critical region, not only in the downstream section of the artery but even in the inter-strut regions (Fig. 5.19a). However, as shown in Figure 5.15, the OSI values highlights the criticality of the downstream region. Finally, no critical OSI zone are observed in the whole narrowed region of the left femoral artery.

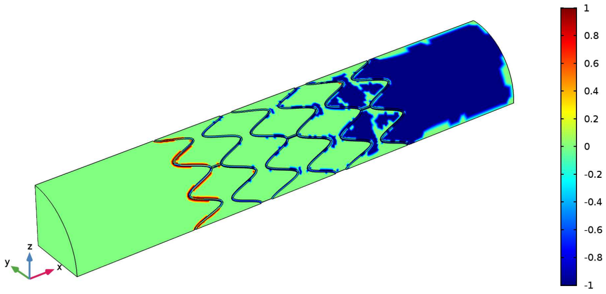

(a) Discrepancy between WSS and OSI index critical zone on the external surface of the left femoral artery.

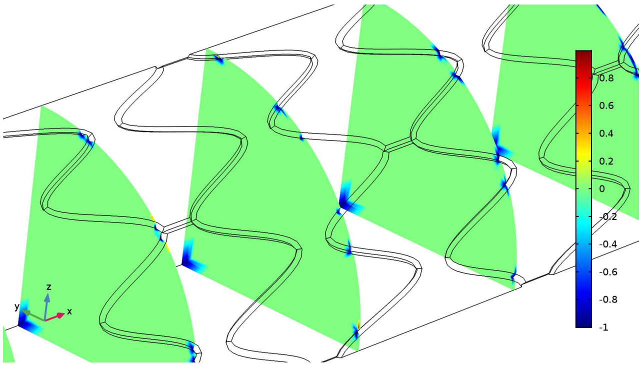

(b) Discrepancy between WSS and OSI index critical zone on transversal left femoral artery slices.

Figure 5.19: Predictors discrepancy, left femoral artery simulation, first cycle.

Additional OSI index plots and graphs can be found in Appendix A.

Chapter 6

Discussion

This chapter focuses on the comparison of the growth curves obtained through the present modelling approach, as well as more sophisticated models available in literature, trying to emphasize the presence of general trends. Moreover, the $in - vivo$ data described in chapter 2 will be also compared with present results.

Figure 6.1 shows the key differences between the stationary and time dependent simulations for the coronary artery. The evolution of the neointimal thickness computed in the various scenarios are remarkably different. In steady flow computations, prescribing at the artery inlet either the mean or the maximum velocity that characterize the blood flow leads not only to a different shape of the endothelialization curve, but also to different values of the equilibrium neointimal thickness. The adoption of a time dependent velocity input, reproducing that associated with a typical cardiac cycle leads to an even more different endothelialization curve and a definitely much higher equilibrium neointimal thickness.

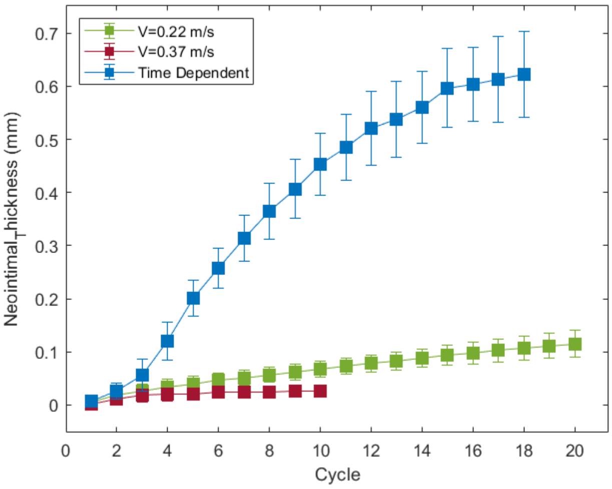

Figure 6.1: Evolution of the mean neointimal thickness (mm) for the coronary artery, resulting from both the steady and unsteady CFD simulations carried out assuming a Newtonian fluid model. The vertical lines correspond to the standard deviation.

Figure 6.2, on the other hand, indicates that in the presence of a time dependent velocity input, the artery diameter matters as well, giving rise to different shapes of the endothelialization curves and, consequently, different normalized neointimal thicknesses. The use of either a Newtonian or Carreau-Yasuda rheological fluid model also produces different endhotelialization curves, but with much less differences in shapes and, hence, in normalized neointimal thickness.

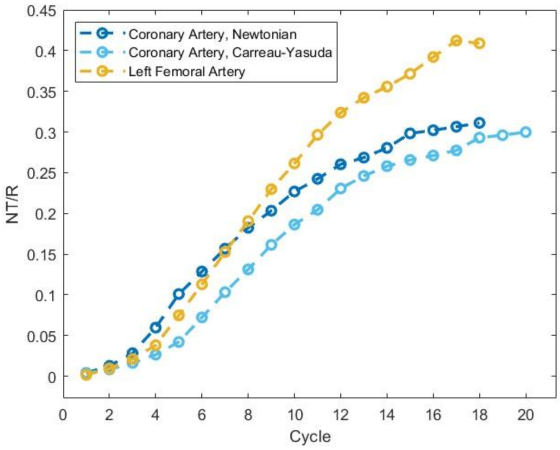

Figure 6.2: Evolution of the neointimal thickness normalized by the respective artery radius, for the coronary artery and left femoral artery, resulting from unsteady CFD simulations carried out assuming both a Newtonian and non-Newtonian fluid model.

Nevertheless, Figure 6.3 shows that when using a more complex scaling of the neointimal thickness, namely:

$$ScaledNT = \frac{NT}{R} \cdot \left(\frac{V_{avg}}{V_{max}}\right)^{0.5} \cdot Re \tag{6.1}$$

the scaled neointimal thickness progression curves obtained for the coronary and the left femoral artery tends to collapse.

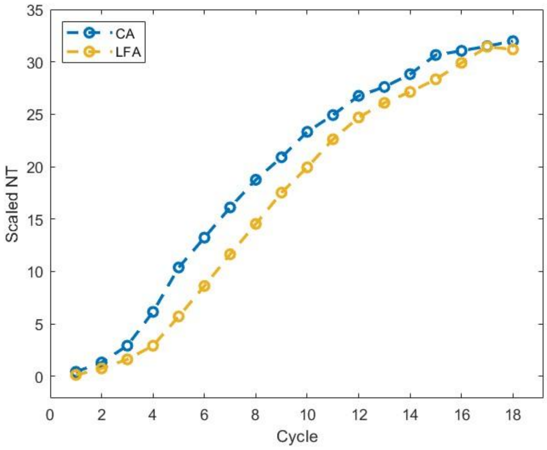

Figure 6.3: Evolution of the neointimal thickness scaled by equation (6.1), for the coronary artery and left femoral artery, resulting from unsteady CFD simulations carried out assuming both a Newtonian fluid model.

This result points out that not only the vessel diameter, but also the form of the input velocity signal (quantified by the ratio of the mean to the maximum velocities) influences the neointimal thickness progression.

Finally, Figure 6.4 reports the progression of the neointimal thickness, scaled by the vessel radius, computed with the present model for a coronary artery, as compared with those resulting from the multiscale numerical model of Zun (2017) and those extracted from the $in - vivo$ porcine data of Tahir (2011) considering a injury score 3 on the Gunn scale.
It clearly appears that the present coronary artery simulation are fully consistent with both the porcine coronary artery $in - vivo$ data and the more sophisticated results obtained in previous numerical studies. This finding suggest that the implementation of a pulsatile inlet velocity and the use of the corresponding time averaged shear stress are sufficient ingredients to obtain a reasonable reproduction of the actual endothelialization process, quantitatively similar to that computed with more complex multiscale numerical simulations, conducted under steady flow condition.

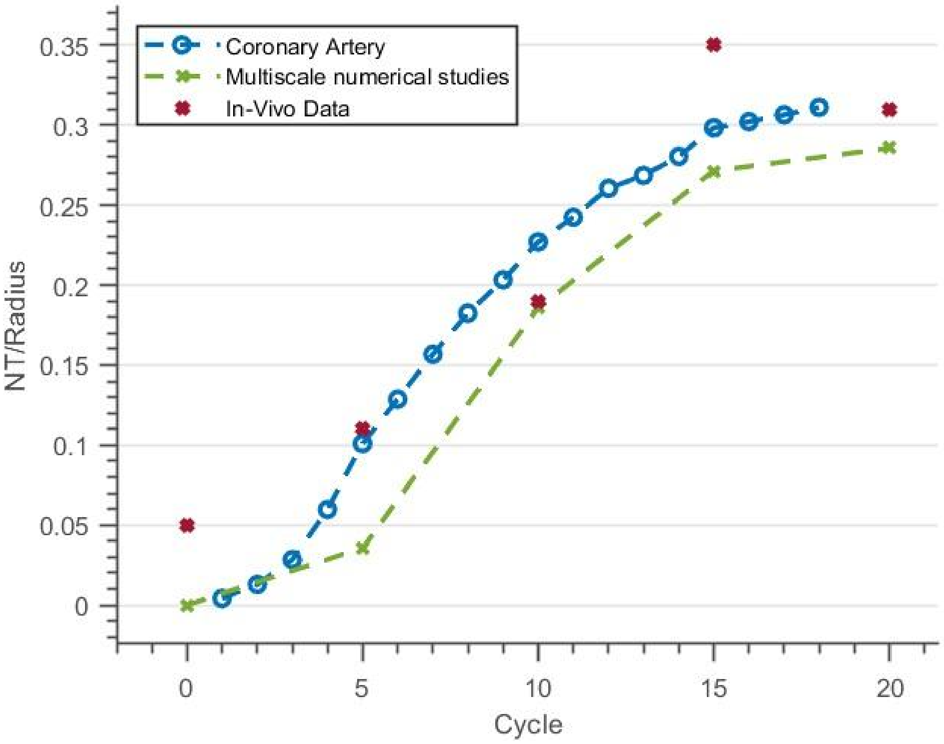

Figure 6.4: Evolution of the neointimal thickness scaled by the respective vessel radius, for the coronary artery unsteady CFD simulations carried out assuming both a Newtonian fluid model, for the multiscale numerical simulation of Zun (2017) and for the $in - vivo$ porcine data of Tahir(2011).

The endothelialization is a continuous process, whereas, the present conceptualized model, discretizes its progression. Additionally, the iterative process implemented to evaluate the wall shear stress, is based on a single cardiac cycle, while the time realistically needed to obtain a similar tissue growth is much higher. The ratio between the real time scale (T_i) and the simulated cycle time scale (T=0.735 s) should be specified by introducing a suitable correlation, between the model growth rate, imposed by the mesh dimension, and the real growth rate (R). The equation proposed, for this relation is

$$NT_{final} = R \cdot \bar{h} \cdot \int_{0}^{T_{final}} \frac{\tau_{cr} - \tau}{\tau_{cr}} dt \tag{6.2}$$

where NT_{final} is the final equilibrium neointimal thickness; R is the real (unknown) endothelial growth rate; $\bar{h}$ is the average element size; T_{final} is the time needed to reach the equilibrium configuration, equal to about 28 days, according to the literature; τ_{cr} is the shear stress threshold and τ is the computed wall stress value below the threshold. Equation (6.2) can be written for each iteration of the present model:

$$\Delta NT_i = R_i \cdot \bar{h}_i \cdot \frac{0.5[Pa] - \overline{TaWSS_i}}{0.5[Pa]} \cdot n \cdot T \tag{6.3}$$

where ΔNT_i is the endothelial growth gain for each iteration; R_i is the real growth rate for each iteration; $\bar{h}_i$ is the average element size considering only the critical regions; $\overline{TaWSS_i}$ is the time-averaged (over the pulsatile cycle of a single iteration) wall shear stress of the critical nodes; and finally, n_i is the ratio between the real time scale and the cardiac cycle period, i.e. $T_i = n \cdot T$ and consequently $\sum_{0}^{final} n \cdot T = 28 days$.

Conclusion

The results obtained, in particular the time dependent results, further corroborate the existence of a correlation between endothelial growth and wall shear stress discussed in chapter 2.

The simulations conducted in this study are based exclusively on fluid dynamic modelling, neither biological nor chemical processes have been included in the simulation setup. The present iterative process-based approach was motivated by the $in - vivo$ relationship found between neointimal thickness and wall shear stresses. Despite the conceptualized modelization of the neointimal thickness, the simulation results compare extremely well with the numerical studies introduced in section 2.3, which included a sophisticated characterization of biological and chemical factors, specific molecules concentration, cell migration and proliferation. Note also that, all these studies were conducted assuming a steady flow condition and Newtonian rheological model.

Through the present model, and the implementation of a time averaged wall shear stress based endothelial growth, we obtained results quantitatively similar to those proposed by the more advanced coupled CFD and biochemical models. In addition, present results highlight the importance of the pulsatile character of blood flow. Considering the evolution of the wall shear stress during the full cardiac cycle, the proposed scheme provided a very good approximation of more complex biological interactions.

Our model, in its simplicity, allows for an efficient exploration of the relevant parameter space. However, it is limited by independence from some key medical parameters. The stent thickness influences the endothelial growth progression exclusively in the initial cycles, and the growth cessation is exclusively function of the vessel diameter and blood velocity, as injury score and re-endothelialization rate are not included in the present model.

Further research is also needed to better understand the role of the vessel form, using real, imported vessels geometry, as well as the role played by the inlet condition. Applying different arterial inlet conditions to the same geometry could provide crucial information on the effect of the cardiac cycle, and help to individuate the type of stented vessels potentially more susceptible to endothelial growth.

Appendix A

Extra plots and figures

High velocity streamlines

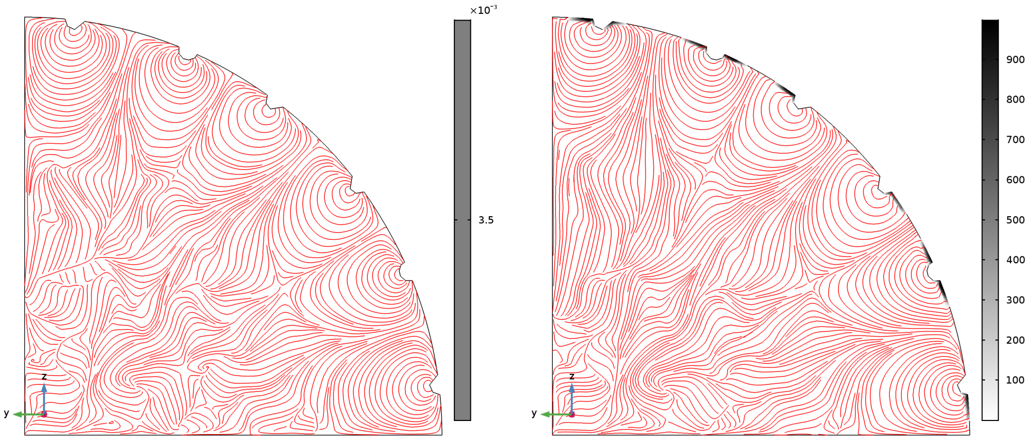

(a) First Cycle (b) Third Cycle

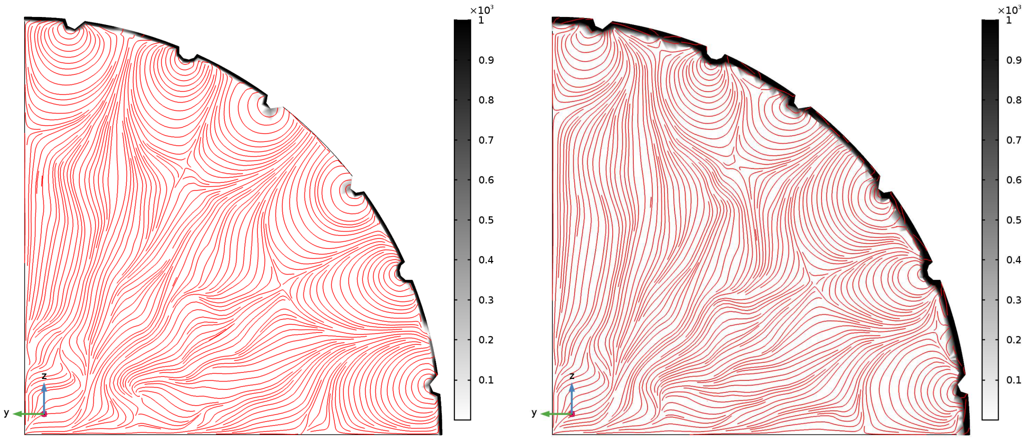

(c) Fifth Cycle (d) Tenth Cycle

Figure A.1: Transversal streamline plots, max velocity simulations. Endothelial growth represented through the dynamical viscosity.

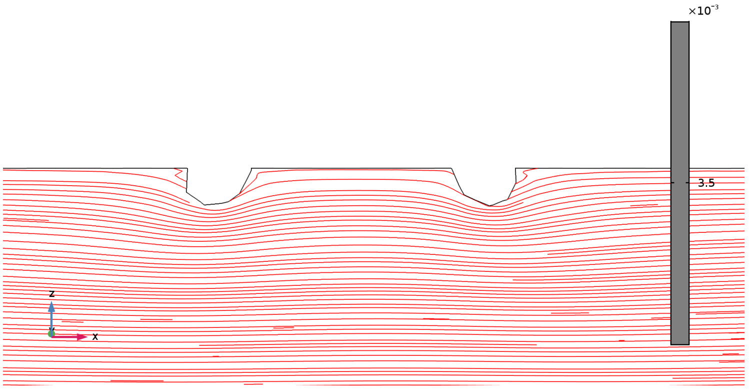

(a) First Cycle

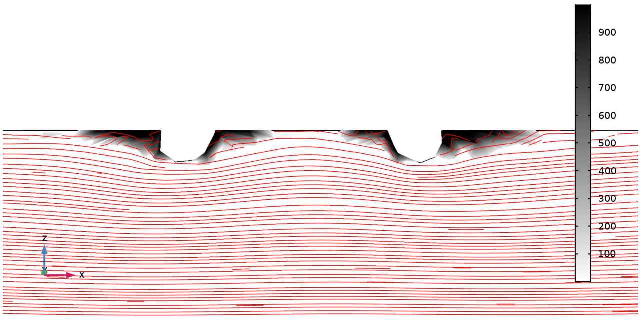

(b) Third Cycle

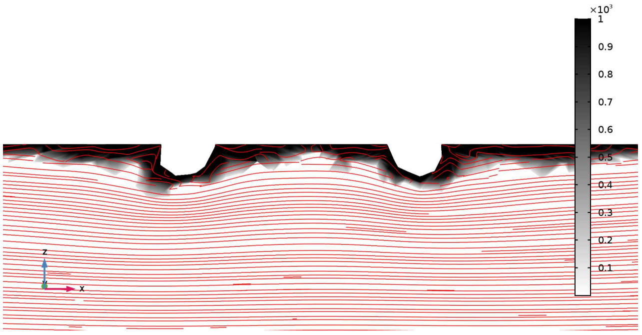

(c) Fifth Cycle

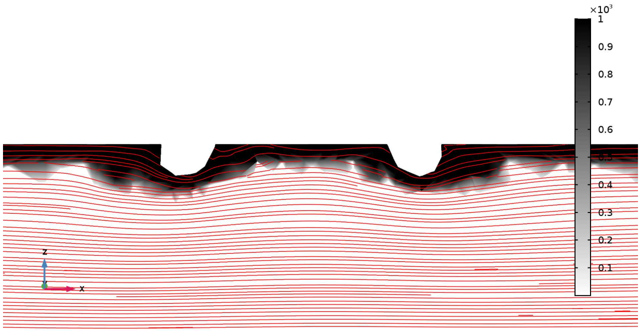

(d) Tenth Cycle

Figure A.2: Longitudinal streamlines plot, max velocity simulations. Endothelial growth represented through the dynamical viscosity.

Coronary artery TaWSS longitudinal distributions

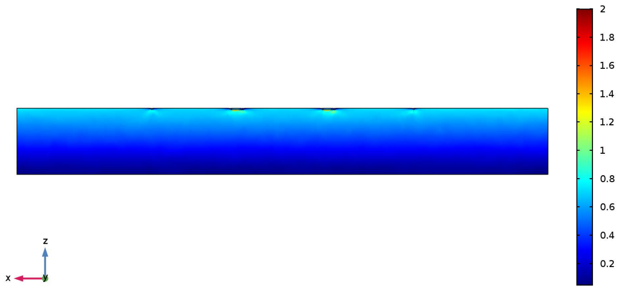

(a) First Cycle

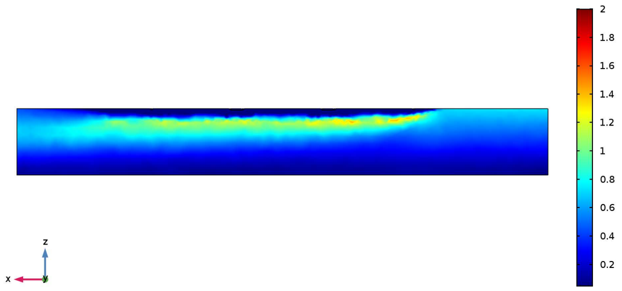

(b) Fifth Cycle

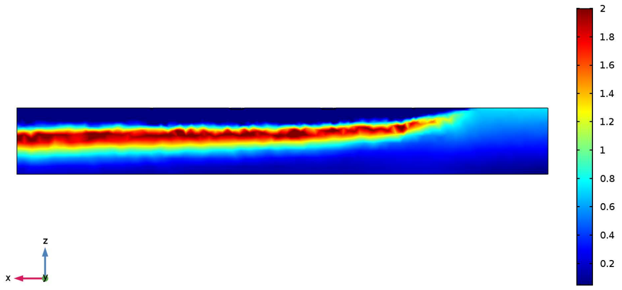

(c) Tenth Cycle

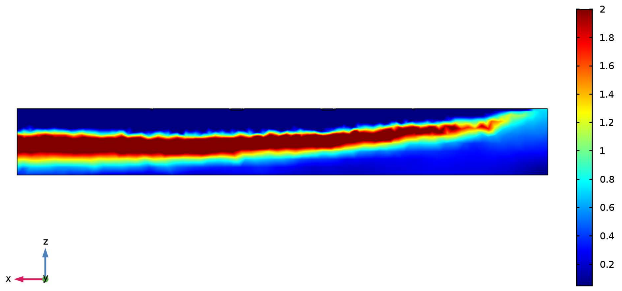

(d) Eighteenth Cycle

Figure A.3: Time averaged wall shear stresses evaluated along a longitudinal cut. Coronary artery simulations, Newtonian model.

Re-Meshing Summary

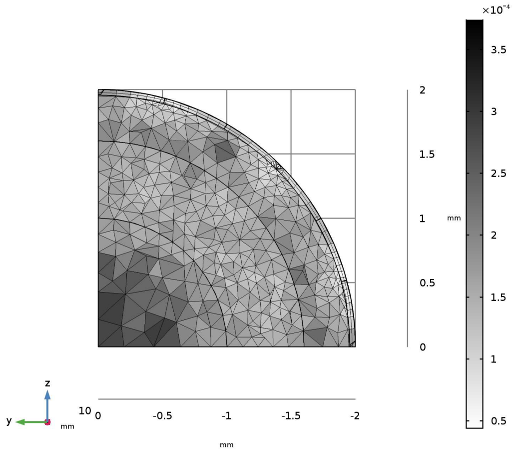

(a) Refined mesh in a circular crown with internal radius 1 mm and external radius 1.6 mm.

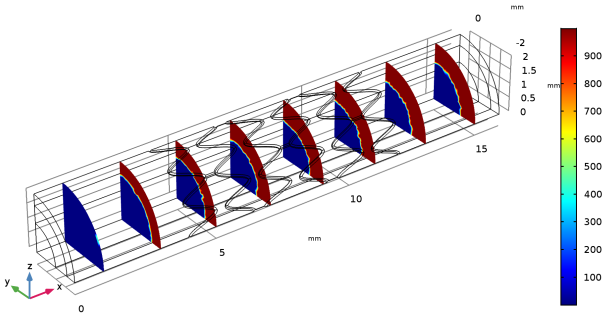

(b) Neointimal thickness profile, mimicked through the dynamical viscosity, obtained for the sixteenth cycle.

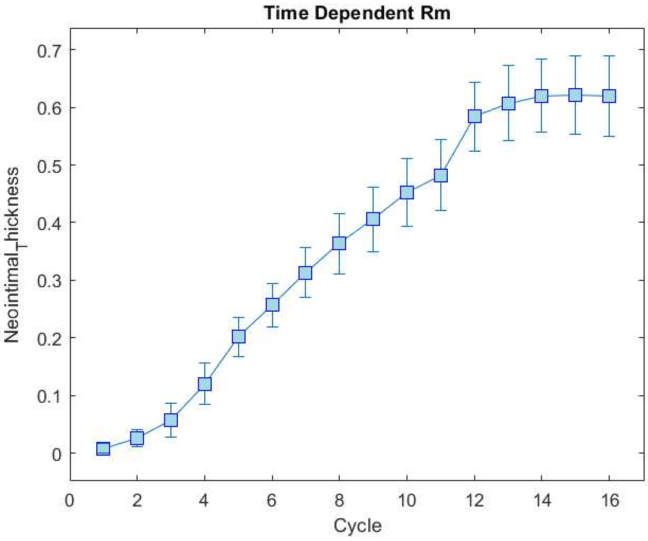

(c) Eighteenth Cycle

Figure A.4: Evolution of neointimal thickness (mm) growth curve for the coronary artery CFD re-meshed simulation carried out assuming a Newtonian fluid.

Additional oscillatory shear index plots

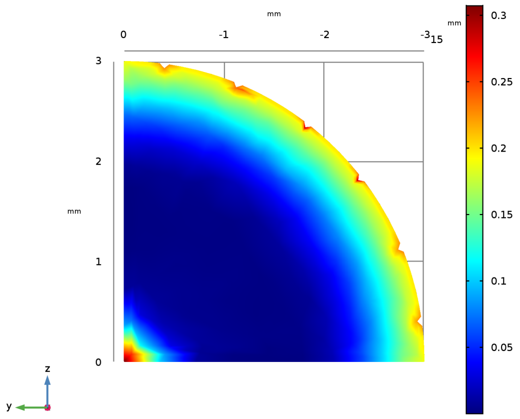

(a) OSI index distribution, obtained for the first Cycle

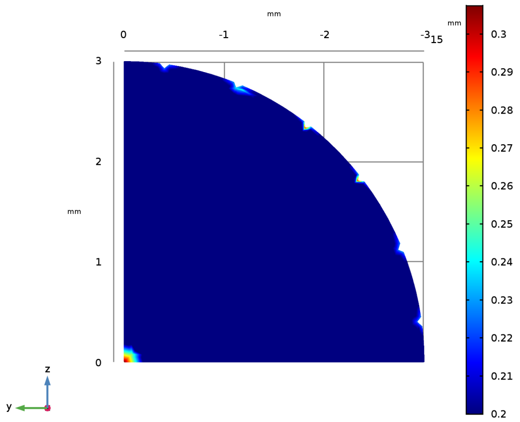

(b) OSI index distribution, obtained for the first Cycle, highlighted the critical regions.

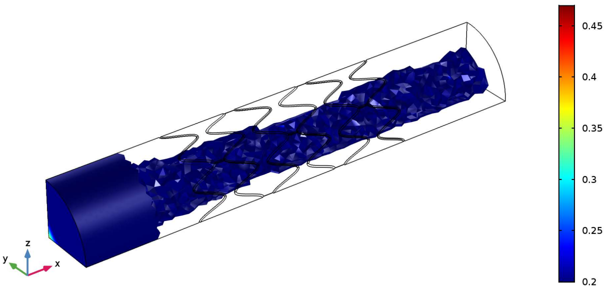

(c) OSI index values for the non-occluded vessel volume, obtained for the eighteenth, and last, cycle.

Figure A.5: OSI index values additional plots, left femoral artery simulations.

Bibliography

Barton, M. et al (2014). “Balloon angioplasty – the legacy of Andreas Grüntzig, M.D. (1939–1985)”. In: *Frontiers in Cardiovascular Medicine* 1.

Bedair, T. et al (2017). “Recent advances to accelerate re-endothelialization for vascular stents”. In: *Journal of Tissue Engineering* 8, pp. 1–14.

Brown, A. et al. (2016). “Role of biomechanical forces in the natural history of coronary atherosclerosis”. In: *Nature Reviews Cardiology* 13, pp. 210–220.

Byrne, R. et al (2015). “Stent thrombosis and restenosis: what have we learned and where are we going? The Andreas Gruntzig Lecture ESC 2014”. In: *European Heart Journal* 36, pp. 3320–3331.

Caiazzo, A. et al. (2011). “A Complex Automata approach for in-stent restenosis: Two dimensional multiscale modelling and simulations”. In: *Journal of Computational Science* 2, pp. 9–17.

CFD Module User’s Guide (2017). v. 5.3. COMSOL Multiphysics®. Stockholm,Sweden. URL: `https://doc.comsol.com/5.4/doc/com.comsol.help.cfd/CFDModuleUsersGuide.pdf`.

Colombo, M. et al. (2021a). “Baseline local hemodynamics as predictor of lumen remodeling at 1-year follow-up in stented superfcial femoral arteries”. In: *Scientific Reports* 11. 1613.

— (2021b). “In-Stent Restenosis Progression in Human Superficial Femoral Arteries: Dynamics of Lumen Remodeling and Impact of Local Hemodynamics”. In: *Annals of Biomedical Engineering* 49, pp. 2349–2364.

COMSOL Multiphysics Reference Manual (2019). v. 5.5. COMSOL Multiphysics®. Stockholm,Sweden. URL: `https://doc.comsol.com/5.5/doc/com.comsol.help.comsol/COMSOL_ReferenceManual.pdf`.

Conforto, C. (2022). “Numerical study of how stent geometry and fuid rheology infuence the restenosis risk in stented coronaries”. MA thesis. University of Padua.

De Santis, G. et al. (2008). “Simulation of wall shear stress-driven in-stent restenosis”. In: *IFMBE Proceedings* 22, pp. 1955–1958.

Duraiswamy, N. et al (2009). “Comparison of Near-Wall Hemodynamic Parameters in Stented Artery Models”. In: *Journal of Biomechanical Engineering* 131.

Erdogan, E. et al (2022). “Intravascular Imaging for Guiding In-Stent Restenosis and Stent Thrombosis Therapy”. In: *Journal of the American Heart Association* 11.

Gunn, J. et al (2002). “Coronary artery stretch versus deep injury in the development of in-stent neointima”. In: *Heart* 88, pp. 401–405.

Guo, X. and G. S. Kassab (2009). “Role of shear stress on nitrite and NOS protein content in different size conduit arteries of swine”. In: *Acta Physiol*, pp. 99–106.

Habara, M. et al (2011). “Difference of Tissue Characteristics Between Early and Very Late Restenosis Lesions After Bare-Metal Stent Implantation - An Optical Coherence Tomography Study”. In: *American Hearth Association Journal* 4.

Jana, Soumen (2019). “Endothelialization of cardiovascular devices”. In: *Acta Biomaterialia* 99, pp. 53–71.

Jeays, A.D. et al. (2007). “Characterisation of the haemodynamics of the superior mesenteric artery”. In: *Journal of Biomechanics* 40, pp. 1916–1926.

Jiang, Y. et al. (2015). “Effects of the inlet conditions and blood models on accurate prediction of hemodynamics in the stented coronary arteries”. In: *AIP Advances* 5. 057109, pp. 2064–2073.

Jiménez, J. M. and P. F. Davies (2009). “Hemodynamically Driven Stent Strut Design”. In: *Annals of Biomedical Engineering* 37, pp. 1483–1494.

Jung, J. et al. (2006). “Multiphase hemodynamic simulation of pulsatile flow in a coronary artery”. In: *Journal of Biomechanics* 39, pp. 2064–2073.

Koskinas, K. et al (2012). “Role of Endothelial Shear Stress in Stent Restenosis and Thrombosis”. In: *Journal of the American College of Cardiology* 59, pp. 1337–1349.

LaDisa, J. F. et al (2005). “Alterations in wall shear stress predict sites of neointimal hyperplasia after stent implantation in rabbit iliac arteries”. In: *American Journal of Physiology-Heart and Circulatory Physiology* 288.

— (2003). “Three-Dimensional Computational Fluid Dynamics Modeling of Alterations in Coronary Wall Shear Stress Produced by Stent Implantation”. In: *Annals of Biomedical Engineering* 31, pp. 972–980.

Livelink^{TM} for MATLAB® User's Guide (2018). v. 5.4. COMSOL Multiphysics®. Stockholm,Sweden. URL: `https://doc.comsol.com/5.4/doc/com.comsol.help.llmatlab/LiveLinkForMATLABUsersGuide.pdf`.

Mahmoudi, M. et al. (2021). “The Story of Wall Shear Stress in Coronary Artery Atherosclerosis: Biochemical Transport and Mechanotransduction”. In: *Journal of Biomechanical Engineering* 143.

Malek, A. M. et al (1999). “Hemodynamic Shear Stress and Its Role in Atherosclerosis”. In: *Journal of the american medical association* 282.

Mitra, A. K. and D. K. Agrawal (2006). “In stent restenosis: bane of the stent era”. In: *Journal of clinical pathology* 59, pp. 232–239.

Morlacchi, S. et al. (2011). “Hemodynamics and In-stent Restenosis: Micro-CT Images, Histology, and Computer Simulations”. In: *Annals of Biomedical Engineering* 39, pp. 2615–2626.

Murphy, J. M. et al (2010). “Predicting neointimal hyperplasia in stented arteries using time-dependant computational fluid dynamics: A review”. In: *Computers in Biology and Medicine* 40, pp. 408–418.

Peiffer, V. et al. (2013). “Computation in the rabbit aorta of a new metric – the transverse wall shear stress – to quantify the multidirectional character of disturbed blood flow”. In: *Journal of Biomechanics* 46, pp. 2651–2658.

Prati, F. et al (2010). “Expert review document on methodology, terminology, and clinical applications of optical coherence tomography: physical principles, methodology of image acquisition, and clinical application for assessment of coronary arteries and atherosclerosis”. In: *European Heart Journal* 31.

Quarteroni, A. et al (2017). “The Cardiovascular System: Mathematical Modeling, Numerical Algorithms, Clinical Applications”. In: *Acta Numerica* 26.

Schillinger, M. et al (2008). “Does Carotid Stent Cell Design Matter?” In: *American Hearth Association Journal* 9.

Schmidt, T. and J. D. Abbott (2018). “Coronary Stents: History, Design, and Construction”. In: *Journal of clinical medicine* 7, pp. 126–134.

Stone, P. H. et al (2003). “Effect of Endothelial Shear Stress on the Progression of Coronary Artery Disease, Vascular Remodeling, and In-Stent Restenosis in Humans”. In: *American Hearth Association Journal* 108, pp. 438–444.

Tahir, H. et al (2011). “Multi-scale simulations of the dynamics of in-stent restenosis: impact of stent deployment and design”. In: *Cardiovascular Research* 1, pp. 365–373.

— (2014). “Modelling the Effect of a Functional Endothelium on the Development of In-Stent Restenosis”. In: *Plos One Journal* 8.

— (2015). “An in silico study on the role of smooth muscle cell migration in neointimal formation after coronary stenting”. In: *Journal of the Royal Society Interface* 12.

Van der Heiden, K. et al (2013). “The effects of stenting on shear stress: relevance to endothelial injury and repair”. In: *Cardiovascular Research* 99, pp. 269–275.

Wentzel, J.J. et al (2000). “Coronary stent implantation changes 3-D vessel geometry and 3-D shear stress distribution”. In: *Journal of Biomechanics* 33, pp. 1287–1295.

White, Paul D. (1957). “The Evolution of Our Knowledge about the Heart and Its Diseases since 1628”. In: *Circulation* 15.

Zun, P. et al. (2019). “3D modelling of in-stent restenosis”. MA thesis. University of Amsterdam.